PAUL SCHERRER INSTITUT

PSI

Annual Report 2003

Electrochemistry Laboratory

http://ecl.web.psi.ch

Cover Photo
Carbons with a high graphitization degree are the first choice material as negative electrode in lithium-ion batteries, for reasons of high performance and low cost. One disadvantage of these materials is the exfoliation tendency in some electrolytes. The cover illustration shows an SEM image of an exfoliated graphite particle.

PAUL SCHERRER INSTITUT

Electrochemistry Laboratory

Annual Report 2003

With excerpts from the 2003 Annual Scientific Report of
the PSI Research Department General Energy (ENE)

Hardcopies of this report are available from:
Isabella Kalt (isabella.kalt@psi.ch)
Paul Scherrer Institut
5232 Villigen PSI
Switzerland

A full version of this report is also available on the web:
http://ecl.web.psi.ch

Paul Scherrer Institut
Electrochemistry Laboratory
5232 Villigen PSI
Switzerland

Secretary
Phone +41 (0)56 310 29 19
Fax +41 (0)56 310 44 15

TABLE OF CONTENTS

EDITORIAL

Günther G. Scherer

The Electrochemistry Laboratory is dedicated to research in various areas of advanced electrochemical energy storage and conversion processes. In addition, the Electrochemistry Laboratory provides expertise and innovative solutions in the fields of batteries, fuel cells, supercapacitors, electrolysis, electrocatalysis, electrochemical material science, and modern methods for electrochemical interface analysis. With this particular research effort Paul Scherrer Institut's Electrochemistry Laboratory, as the leading institution in this area in Switzerland, will contribute to the long-term development of zero emission converters and energy storage systems in the context of a sustainable development.

Currently, the laboratory is organized into the following five research groups: Fuel Cells, Fuel Cell Systems, Batteries, Capacitors, and Materials. Within this Annual Report each of the research groups is represented by several contributions, highlighting their research efforts and their results of the past year 2003.

According to the laboratory's philosophy we carry out research and development of electrochemical energy conversion and storage systems at the materials, cell, and systems level. This is the reason why many of our projects are materials development oriented. Surface, interface, and inter-phase aspects of materials play an important role, for the processes occurring in electrochemical conversion and storage systems. Materials aspects will influence cell and systems design, hence the development of more sophisticated and over all cheaper materials will allow working on more efficient but simpler cells and systems. Emphasis is also given to develop the necessary tools of thin film preparation, surface modification, and surface analysis. These tools are applied to a vast variety of materials, among others to polymers and inorganic materials for non-electrochemical applications.

The implementation of novel *in situ* diagnostic methods for electrochemical cells is another topic, which has been emphasized during the past year. The use of PSI's large facilities, like SINQ or SLS, for our research projects has become "standard" and will even be increased in the upcoming years.

Many of our projects carried out during the year 2003 have medium-term goals; results will be published in future years. This is particularly the case with projects performed in collaboration with industrial partners. All of our groups have been successful in the year 2003 to acquire new projects with industrial partners, either bilateral or within the context of national or international programs. Together with industrial partners several patents have been filed.

Continuous education of our students and co-workers is another primary goal of our laboratory. The visit of Prof. Dr. Dieter M. Kolb, University of Ulm, Germany, current President of the International Society of Electrochemistry, from July 7 to 10 was the highlight of this year. Prof. Kolb delivered to us eight stimulating lectures on the Fundamentals of Modern Electrochemistry and we had the chance to discuss many other topics during the week he spent with us. Participation of our co-workers at national or international conferences, including numerous lectures or poster presentations, served as a means to expose the Laboratory to the international scientific community. Further, several diploma and summer students spent time with us to carry out their thesis in one of our research groups.

Communication to our partners in research projects, within the Paul Scherrer Institut, and to the scientific community outside of PSI is of utmost importance to us. For this reason, the laboratory again organized successfully a One-Day-Symposium with international participation. The 18th One-Day-Symposium took place on the 28th of May, addressing the theme "Electrolytes for Electrochemical Cells". Lectures on various aspects of liquid, aqueous and non-aqueous, as well as solid electrolytes were given by M. Winter (Graz), K.D. Kreuer (Stuttgart), J. Vetter (Villigen), V. Hennige (Marl), M. Fooken (Stuttgart), H.P. Brack (Villigen), M. Roelofs (Wilmington, DE), Ö. Ünsal (Frankfurt/M.) and L. Gauckler (Zürich). We look forward to the 19th and 20th Symposium, which will take place on January 16th, respectively September 15th, 2004.

Further, our Electrochemistry Seminar (a Monday afternoon affair), was organized in several cycles to various topics by either our PhD-students, post-doctoral fellows, and the group leaders and took place 35 times, with 15 external speakers.

In summary, we can look back again to a successful year 2003. This gives us great confidence to further contribute to the field of Electrochemistry and transfer our know-how to industrial partners as well as to support education of students in these areas. We see our work in the wider context of a sustainable energy development, which also has been identified as a general future goal of the Domain of the Swiss Federal Institutes of Technology.

Prof. Dr. D.M. Kolb on the occasion of his visit of the Electrochemistry Laboratory of Paul Scherrer Institut (July 7 to July 10, 2004), during a lecture delivered to our PhD-students and colleagues.

THE ELECTROCHEMISTRY LABORATORY

STRUCTURE

Electrochemistry Laboratory

G.G. Scherer (head)
I. Kalt (secretary)

Fuel Cells

G.G. Scherer

Clean Energy Conversion with high efficiency
Optimized components and cells

Fuel Cell Systems

F. Büchi

Optimisation of system efficiency
Novel stack concepts

Batteries

P. Novak

High energy density
Compact 4V cells

Capacitors

R. Kötz

High power density complementary storage device
High capacitance and cycle life

Materials

Th. Lippert

Design of functional materials
Fundamental under-standing of interfacial processes

Interface Analysis

R. Kötz

In situ and *ex situ* characterization of the electrochemical interface.

LEC-PERSONNEL

Staff

Alkan Gürsel Selmiye, Dr. (since February, 2003)**,** **A**ndreaus Bernhard, Dr. (until November, 2003), **A**rcaro Manual, **B**ärtsch Martin, Dr. (until December, 2003), **B**arbieri Olivier, Dr. (since January, 2003), **B**ärtschi Martin (until June, 2003), **B**rack Hans-Peter, Dr. (until Septenber, 2003), **B**üchi Felix, Dr., **B**uqa Hilmi, Dr., **D**eiss Erich, Dr., **G**eiger Friederike, **G**ubler Lorenz, Dr., **H**ahn Matthias, Dr., **H**olzapfel Michael, Dr. (since May, 2003), **K**aiser Hermann, **K**alt Isabella, **K**ötz Rüdiger, Dr., **L**ippert Thomas, Dr., **M**army Christian, **N**ovák Petr, Dr., **P**aganelli Gino, Dr. (since February, 2003), **P**anozzo Roberto (until July, 2003), **P**eter Sandra, **R**aimondi Fabio, Dr. (since March, 2003), **R**ichner Roy, Dr. (until March, 2003), **S**auter Jean-Claude, **S**cheifele Werner, **S**cherer Günther G., Dr., **S**chneider Ingo, Dr. (since December, 2003), **S**chnyder Bernhard, Dr., **S**teiger Beat, Dr., **S**tössel-Sittig Caroline, Dr., **T**obler Martina (since August, 2003), **T**sukada Akinori, **U**fheil Joachim, Dr. (since February, 2003), **V**etter Jens, Dr., **W**ambach Jörg, Dr..

PhD Students

Campana Flavio, **D**umont Thomas, **G**oers Dietrich (until December, 2003), **F**reunberger Stefan (since January, 2003), **H**ajbolouri Faegheh, **H**ardwick Laurence (since September, 2003), **H**auer Marc, **K**opitkovas Giedrius, **K**ramer Denis, **K**uhn Holger, **K**uhnke Markus, **L**empola Nina, **M**ontenegro Macarena, **P**iotto Piotto Andrea, **R**einer Andreas (since June, 2003), **S**antis Marco, **S**laski Michal, **U**rech Lukas (since October, 2003), **W**immer Jean, **W**ürsig Andreas.

AWARDS

T. Dumont
Marie Curie Research Fellowship
at the Université de Bordeaux1, France, January - April 2003.

M. Montenegro
Marie Curie Research Fellowship
at the Foundation for Research & Technology - Hellas, Crete, Greece,
September - December 2003.

D. Schmid[1], M. Santis, M. Ruge[1], F.N. Büchi
PowerPac Project
Swiss Technology Award, 2003.
[1] ETH Zürich

THIS PhD STUDENT FROM ECL GRADUATED IN 2003

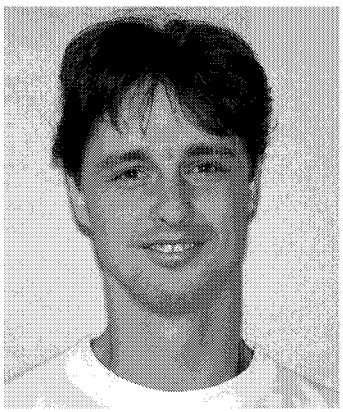

Dr. Dietrich Goers

Title of thesis:

In situ Raman-Spektroskopie und Videomikroskopie an Lithium-Ionen-Batterien
PhD. Thesis, No. 15344

Advisor at university:	Prof. R. Nesper, ETH Zürich
Advisor at PSI:	Prof. A. Wokaun PD Dr. P. Novak
Date of oral examen:	November 26, 2003

EXCHANGE STUDENTS, DIPLOMA THESES, SUMMER STUDENTS

T. Kondo, PhD-Candidate
Laser ablation of polymers with different pulse lengths
Tokushima University, Japan, September 2002 – March 2003

T. Weber
Beiträge zur Zyklovoltammetrie an der polykristallinen Platinelektrode in wässrigen Elektrolytlösungen
ETH Zürich, October 2002 – February 2003

B. Köllmann
Entwicklung einer Regelung der Methanolkonzentration in wässriger Lösung und Integration in Teststände zur Charakterisierung von Direkt-Methanol-Brennstoffzellen
Technische Universität, Clausthal, Germany, October 2002 – March 2003

K. Meissner
Comparison of laser ablation plasma spectroscopy with laser ablation inductively coupled-plasma mass spectrometry
Fachhochschule Wiesbaden, Germany/ETH Zürich, November 2002 – April 2003

R. Lachmann
Charakterisierung eines neuen Aktivmaterials für die Lithium-Ionenbatterie
ETH Zürich, February 2003

J. Lobpreis
Time- and space resolved emission spectroscopy during pulse laser deposition
Fachhochschule Wiesbaden, Germany, March – August 2003

S. Loher
Introduction and validation of a dynamic hydrogen reference electrode in a direct methanol fuel cell
ETH Zürich, April – June 2003

H. Yoshikawa, PhD-Candidate
Microstructuring of polymers and glass for microfluidic devices
Osaka University, Japan, April – July 2003

L. Caldwell
Electrochemical impedance spectroscopy porous PEFC electrodes
Imperial College, London, Great Britain, July – September 2003

O. Sanz, PhD-Candidate
Experiments with pulsed reactive crossed beam laser ablation
Instituto de Optica, Madrid, Spain, August – September 2003

S. Canulescu
Experiments with pulsed reactive crossed beam ablation
INFLPR, Bucharest, Romania, October – December 2003

S. Deubelbeiss
Inbetriebnahme eines neuen 100 cm^2 Brennstoffzellen-Designs
ETH Zürich, October – November 2003

SEMINAR, INVITED SPEAKERS

Prof. Dr. K. Krischer
Technische Universität, München, Germany
Selbstorganisierte Reaktivitätsmuster bei der Oxidation von CO sowie H_2 in Gegenwart von Katalysatorgiften an Pt-Elektroden
January 20, 2003.

Prof. Dr. N. Djilali
University of Victoria, Canada
Computational modelling of multiphase transport phenomena in PEM fuel cells
May 21, 2003

Prof. Dr. S. Virtanen
ETH Zürich
Modern methods in the study of corrosion mechanisms: towards an in-depth understanding of passivation and localized breakdown of metallic materials.
May 26, 2003.

P. Sudan
Universität Freiburg
Carbon nanotubes: fundamental and electrochemical applications
June 16, 2003.

Dr. P. Rüetschi
ehem. Leclanché SA, Yverdon-les-Bains
Alterungsprozesse in Bleisäure-Akkumulatoren
June 23, 2003

Dr. M. Jakob
Center for Energy Policy and Economics, ETH Zürich
Beiträge zur Erreichung des CO_2-Zieles
June 30, 2003.

Dr. P. Häring
Oerlikon Stationäre Batterien AG, Aesch
Bleiakkumulatoren in stationären Energieversorgungen
September 15, 2003.

Dr. U. Paulus
Fritz Haber-Institut der Max-Planck Gesellschaft, Berlin, Germany
Adsorption und Oxidation von CO auf $RuO_2(110)$ – eine UHV Studie
September 22, 2003.

Dr. J. Schumacher, Ch. Ziegler, A. Hakenjos
Fraunhofer Institut, Freiburg, Germany
Charakterisierung portabler Brennstoffzellen, Simulation und Messtechnik
September 29, 2003.

Dr. Thomas Vad
Forschungszentrum Jülich, Germany
Characterization of co-sputtered Pt/C layers by anomalous small-angle X-ray scattering
November 18, 2003.

Prof. Dr. Bhuvanesh Gupta
Indian Institute of Technology, New Delhi, India
Radiation induced graft modification of polymers
December 18, 2003.

CONFERENCES – WORKSHOPS

Electrolytes for Electrochemical Cells
18th One-Day-Symposium
May 28, 2003
Organizers: G.G. Scherer, P. Novák, R. Kötz

With contributions from:

Prof. Dr. M. Winter, Technische Universität Graz, Austria
Dr. K.D. Kreuer, Max Planck Institut, Stuttgart, Germany
Dr. J. Vetter, Paul Scherrer Institut, Villigen
Dr. V. Hennige, Degussa, Creavis Technologie & Innovation, Marl, Germany
Dr. M. Fooken, Honeywell Specialty Chemicals Seelze GmbH, Seelze, Germany
Dr. H.P. Brack, Paul Scherrer Institut, Villigen
Dr. M.G. Roelofs, DuPont Company, Wilmington, USA
Dr. Ö. Ünsal, Celanese Venture GmbH, Frankfurt am Main, Germany
Prof. Dr. L.J. Gauckler, Eidgenössische Technische Hochschule, Zürich

Einführung in moderne Aspekte der Elektrochemie
Seminarreihe mit Prof. Dr. Dieter M. Kolb, Universität Ulm, Deutschland
July 7 – 10, 2003
Organizer: G.G. Scherer

Workshop "1st Infrared Users Meeting"
4th SLS Users Meeting, PSI, SLS, Villigen,
October 31, 2003.
Organizer and Chairman: J. Wambach

REVIEW ACTIVITIES OF THE LABORATORY FOR FOLLOWING JOURNALS

American Chemical Society Books, **A**pplied Physics A, **A**pplied Physics Letters, **C**hemical Communications, **C**hemical Society Reviews, **E**lectrochemical and Solid State Letters, **E**urophysics Letters, **F**uel Cells – From Fundamentals to Systems, **I**EEE Transactions of Plasma Science, **I**onics, **J**ournal of Applied Chemistry, **J**ournal of Electroanalytical Chemistry, **J**ournal of Electrochemical Society, **J**ournal of Materials Chemistry, **J**ournal of Microlithography – Microfabrication and Microsystems, **J**ournal of Photochemistry Photobiology A: Chemistry, **J**ournal of Physical Chemistry, **J**ournal of Power Sources, **L**angmuir, **N**ature Materials, **O**ptical Materials, **S**olid State Ionics, **T**hin Solid Films.

REVIEW ACTIVITIES OF THE LABORATORY FOR THE FOLLOWING ORGANISATIONS

Christian Doppler Forschungsgesellschaft, Österreich; **M**ISTRA, Schweden; **A**ustrian Research Centers, Kompetenzzentren-Programm; **P**SI, Forschungskommission.

CO-REFEREE'S REPORT FOR DISSERTATIONS

Dietrich **G**oers, PSI/ETH Zürich; Jari **I**honen, KTH, Stockholm, Sweden; Daniel **S**chmid, ETH, Zürich.

PROJECTS, TEACHING ACTIVITIES, SCIENTIFIC CONTRIBUTIONS TO JOURNALS AND CONFERENCES, PATENT APPLICATIONS AND MEMBERSHIPS

PROJECT COLLABORATIONS WITH EXTERNAL PARTNERS

BBW

Projektleiter: P. Novák
CAMELiA (Calendar life mastering of Li-ion accumulator)
EU-Projekt

Projektleiter: P. Novák
LiBERAL (Lithium battery evaluation and research – accelerated life test direction)
EU-Projekt

Projektleiter: P. Novák
SLiON (Solvent-free lithium polymer starter battery)
EU-Projekt

Projektleiter: G.G. Scherer
FCTESTNET
EU-Projekt

BFE

Projektleiter: F.N. Büchi
Numerische Modellierung von PE Brennstoffzellen mit der FE-Methode
BFE and ZHW Winterthur

Projektleiter: F.N. Büchi
Untersuchung des Temperaturverhaltens von PE Brennstoffzellen im Bereich 0 bis -10 °C

Projektleiter: G.G. Scherer
Polymer Elektrolyt Brennstoffzellen mit H_2 und Methanol als Brennstoff

EOARD

Projektleiter: T. Lippert
Polymers used as fuel in laser plasma thrusters in small satellites

EU AND INDUSTRY (CRAFT)

Projektleiter: P. Novák
High performance active smart card with contactless charging
EU-Projekt

INDUSTRY

Projektleiter: L. Gubler
Membranen für die Direkt Methanol Brennstoffzelle
Chemische Industrie

Projektleiter: P. Novák
Entwicklung eines Batterieseparators auf Basis der keramischen Membranfolie der CREAVIS
CREAVIS Gesellschaft für Technologie und Innovation mbH, Marl, Germany

Projektleiter: P. Novák
Behandlung der Graphite für die negative Elektrode der Lithiumionen-Batterie
TIMCAL AG, Bodio

Projektleiter: P. Novák
Elektrochemische Charakterisierung von Oxiden für Lithiumionen-Batterien
Ferro GmbH, Frankfurt/Main, Germany

Projektleiter: P. Novák
Elektrode für Lithiumionen-Batterie
Circuit Foil Luxembourg, Luxembourg

Projektleiter: G.G. Scherer
Membranentwicklung für Brennstoffzellen
Chemische Industrie

Projektleiter: G.G. Scherer
CO-Toleranz von Polymerelektrolyt Brennstoffzellen
R. Bosch AG

Projektleiter: G.G. Scherer
Diagnostics of Polymer Electrolyte Fuel Cells
Automotive Industry

KTI

Projektleiter: R. Kötz
Optimized Electrochemical Capacitors
Maxwell Technologies SA, Rossens

Projektleiter: R. Kötz
Synthesis of supported nanostructured high porosity carbon as electrode material
Maxwell Technologies SA, Rossens
EMPA Dübendorf
TIMCAL, Bodio

Projektleiter: T. Lippert
Laser-Dünnglasbeschriftung: Methoden und Systeme
Frewit Printing SA, Fribourg

Projektleiter: B. Schnyder
Corrosion aspects of the EDM process
Agie SA

NATIONALFONDS

Projektleiter: R. Kötz
Scanning probe microscopy of the solid electrolyte interface

Projektleiter: P. Novák
Synthesis and characterization of advanced electroactive materials for electrodes of rechargeable lithium-ion batterie

Projektleiter: A. Wokaun, T. Lippert
Comparison of the mechanism of laser ablation and laser-induced material transfer

TEACHING ACTIVITIES

University Level Teaching

PD Dr. T. Lippert
Wahlfach Chemische Aspekte der Energie, Teil II, Mikrostrukturen, Laseranwendungen und neue Materialien
ETH Zürich, SS 2003.

PD Dr. P. Novák, Prof. Dr. A. Wokaun
Technische Elektrochemie
ETH Zürich, WS 2003/2004

Prof. Dr. A. Wokaun, Dr. J. Gass, Dr. G.G. Scherer
Technik erneuerbarer Energien, Teil 2
ETH Zürich, WS 2003/2004.

Lecture Courses at Other Schools

Contributions to Courses at Universities, FHL, and Other Institutes

Dr. M. Hahn
Brennstoffzellen und Supercaps
Beitrag zur PSI-Herbstschule, PSI, Villigen, October 6-10, 2003.

D. Kramer, Dr. B.H. Andreaus
Brennstoffzellen und Supercaps
Beitrag zur PSI-Herbstschule, PSI, Villigen, October 6-10, 2003.

PUBLICATIONS

Books and Reviewed Book Chapters

F.N. Büchi
Small size PEFC systems for special applications
Handbook of Fuel Cells - Fundamentals, Technology and Applications, (ISBN Nr. 0471-49926-9), John Wiley & Sons, Ltd, Chichester, **4**, Part 2, 1152–1161 (2003).

P. Dietrich, F.N. Büchi, A. Tsukada, M. Bärtschi, R. Kötz, G.G. Scherer, P. Rodatz[1], O. Garcia[1], M. Ruge[1], M. Wollenberg[2], P. Lück[2], A. Wiartalla[3], C. Schönfelder[3], A. Schneuwly[4], P. Barrade[5]
Hy.Power – A technology platform combining a fuel cell system and a supercapacitor
Handbook of Fuel Cells - Fundamentals, Technology and Applications, (ISBN Nr. 0471-49926-9), John Wiley & Sons, Ltd, Chichester, **4**, Part 2, 1184–1198 (2003).
[1] ETH Zürich
[2] Volkswagen AG, Wolfsburg, Germany
[3] FEV Motorentechnik, Aachen, Germany
[4] Montena Components SA, Rossens
[5] EPF Lausanne

O. Haas, F. Holzer, K. Müller, S. Müller
Metal/air batteries: The zinc/air case
Handbook of Fuel Cells - Fundamentals, Technology and Applications, (ISBN Nr. 0471-49926-9), John Wiley & Sons, Ltd, Chichester, **1**, Part 4, 382-408 (2003).

G.A. Nazzri[1], E. Takeuchi[2], R. Kötz, B. Scrosati[3]
Batteries and Supercapacitors
Proc. **2001-21**, The Electrochemical Society, Inc., 65 South Main Street, Pennington, New Jersey 08534-2839, USA, 2003
[1] General Motors, Warren, Michigan, USA
[2] Wilson Greatbatch, Ltd., Clarence, New York, USA
[3] Universita di Roma, Italy

Peer Reviewed Papers

A. Alessandrini[1], M. Gerunda[1], P. Facci[1], B. Schnyder, R. Kötz
Tuning molecular orientation in protein films
Surface Science **542** 64-71(2003).
[1] University of Modena and Reggio Emilia, Modena, Italy

H.-P. Brack, M. Wyler, G. Peter, G.G. Scherer
A contact angle investigation of the surface properties of selected proton-conducting radiation-grafted membranes
J. Membr. Sci. **5429**, 1-19 (2003).

H.-P. Brack, D. Fischer[1], G. Peter[1], M. Slaski, G.G. Scherer
Infrared and raman spectroscopic investigation of crosslinked polystyrenes and radiation-grafted films
Journal of Polymer Science Part A: Polymer Chemistry **42**, 59-75 (2003).
[1] Zürcher Hochschule, Winterthur

A. Braun, M.Bärtsch, O.Merlo[1], B. Schnyder, B. Schaffner, R. Kötz, O. Haas, A. Wokaun
Exponential growth of electrochemical double layer capacitance in glassy carbon during thermal oxidation
Carbon **41,** 759-765 (2003).
[1] University of Fribourg

H. Buqa, D. Goers, M.E. Spahr[1], P. Novák
The influence of graphite surface modification on the exfoliation during electrochemical lithium insertion
J. Solid State Electrochem. **8**, 79-80 (2003).
[1] TIMCAL SA, Bodio

H. Buqa, D. Goers, M.E. Spahr[1], P. Novák
Recent improvements in electrochemical performance of graphite negative electrodes for lithium-ion batteries
ITE Letters on Batteries, New Technologies & Medicine **4**, 38-43 (2003).
[1] TIMCAL SA, Bodio

F. Gassmann, R. Kötz, A. Wokaun
Supercapacitors boost the fuel cell car
Europhysics News **34**, 176-180 (2003).

D. Goers, H. Buqa, L. Hardwick, A. Würsig, P. Novák
Raman spectroscopic and structural studies of heat-treated graphites for lithium-ion batteries
Ionics **9**, 258-265 (2003).

M. Hauer, D.J. Funk[1], T. Lippert, A. Wokaun
Laser induced decomposition of a designed and a commercial polymer studied by ns-interferometry and shadowgraphy
Appl. Phys. A **77**, 297-301 (2003).
[1] Los Alamos National Laboratory, USA

M. Hauer, D.J. Funk[1], T. Lippert, A. Wokaun
Laser ablation of polymers studied by ns-interferometry and ns-shadowgraphy measurements
Appl. Surf. Sci. **208-209**, 107-112 (2003).
[1] Los Alamos National Laboratory, USA

G. Kopitkovas, T. Lippert, C. David, A. Wokaun, J. Gobrecht
Fabrication of micro-optical elements in quartz by laser induced backside wet etching
Microel. Eng. **67-68**, 438-444 (2003).

M. Lanz, C. Kormann[1], P. Novák
A procedure for specific charge and cycling performance measurements on $LiMn_2O_4$ spinels for lithium-ion batteries
J. Solid State Electrochem. **7**, 658-664 (2003).
[1] BASF AG, Ludwigshafen, Germany

T. Lippert, M. Hauer, C. Phipps[1], A. Wokaun
Fundamentals and applications of polymers designed for laser ablation
Appl. Phys. A **77**, 259-264 (2003).
[1] Photonic Associates, Santa Fe, NM, USA

T. Lippert, J.T. Dickinson[1]
Chemical and spectroscopic aspects of polymer ablation- special features and novel directions
Chem. Rev. **103**, 453-485 (2003).
[1] Washington State University, USA

M.J. Montenegro, C. Clerc[1], T. Lippert, S. Müller[2], A. Weidenkaff[3], P.R. Willmott[4], A. Wokaun
Analysis of the plasma produced by pulsed reactive crossed-beam laser ablation of $La_{0.6}Ca_{0.4}CoO_3$, Appl. Surf. Sci. **208-209**, 45-51 (2003).
[1] University of Zürich
[2] Euresearch, Bern
[3] University of Augsburg, Germany
[4] University of Zürich and PSI

C. Padeste, B. Steiger, A. Grubelnik, L. Tiefenauer
Redox labelled avidin for enzyme sensor architectures
Biosens. Bioelectron. **19**, 239-247 (2003).

U. Paulus[1], Z. Veziridis[2], B. Schnyder, M. Kuhnke, G.G. Scherer, A. Wokaun
Fundamental investigation of catalyst utilization at the electrode/solid polymer electrolyte interface – Part I: Development of a model system
J. Electroanal. Chem. **541**, 77-91 (2003).
[1] Fritz Haber-Institut, Berlin, Germany
[2] Volkswagen AG, Wolfsburg, Germany

C.R. Phipps[1], J.R. Luke[2], G.G. McDuff[2], T. Lippert
Laser-driven micro-rocket
Appl. Phys. A **77**, 193-201 (2003).
[1] Photonic Associates, Santa Fe, NM, USA
[2] NMT Albuquerque, USA

T. Rager
Pre-Irradiation grafting of styrene/divinylbenzene onto poly(tetrafluoroethylene-cohexafluoropylene) from non-solvens
Helv. Chim. Acta **86,** 1966-1981 (2003).

F. Raimondi, J. Wambach, A. Wokaun
Structural properties of Cu/ZnO/Si methanol reforming catalysts: Influence of the composition of the reactant mixture and of the Cu island size
Phys. Chem. Chem. Phys. **5**, 4015–4024 (2003).

F. Raimondi, B. Schnyder, R. Kötz, R. Schelldorfer, T. Jung, J. Wambach, A. Wokaun
Structural changes of model Cu/ZnO catalysts during exposure to methanol reforming conditions surface
Surf. Sci. **532,** 383-389 (2003).

B. Schnyder, T. Lippert, R. Kötz, A. Wokaun, V.-M. Graubner[1], O. Nuyken[1]
UV-irradiation induced modification of PDMS films investigated by XPS and spectroscopic ellipsometry
Surf. Sci. **532-535**, 1067-1071 (2003).
[1] TU Munich, Germany

M.E. Spahr[1], H. Wilhelm[1], T. Palladino[1], N. Dupont-Pavlovsky, D. Goers, F. Joho, P. Novák
The role of graphite surface group chemistry on the graphite exfoliation during electrochemical lithium insertion
J. Power Sources **119-121**, 543-549 (2003).
[1] TIMCAL SA, Bodio
[2] Université de Nancy I, Vandœuvre-lès-Nancy, France

B. Steiger, C. Padeste, A. Grubelnik, L. Tiefenauer
Charge transport effects in ferrocene-streptavidin multilayers immobilized on electrode surfaces
Electrochim. Acta **48**, 761-769 (2003).

J. Vetter, P. Novák
Novel alkyl methyl carbonate solvents for lithium-ion batteries
J. Power Sources **119-121**, 338-342 (2003).

K. Yamasaki[1], S. Juodkazis[1], T. Lippert, M. Watanabe[1], S. Matsuo[1], H. Misawa[1]
Dielectric breakdown of rubber materials by femtosecond irradiation
Appl. Phys. A **76**, 325-329 (2003).
[1] University of Tokushima, Japan

Other Papers

B.H. Andreaus, G.G. Scherer
Interpretation of the current-voltage characteristics of polymer electrolyte fuel cells by impedance spectroscopy
Proc. 2nd European PEFC Forum, Luzern, June 30 - July 4, (ISBN 3-905592-13-4), **1**, 373-382 (2003).
H.-P. Brack, D. Fischer[1], M. Slaski, G. Peter[1], G.G. Scherer
Crosslinked radiation-grafted membranes
Proc. 2nd European PEFC Forum, Luzern, June 30 - July 4, (ISBN 3-905592-13-4), **1**, 127-136 (2003).
[1] Zürcher Hochschule, Winterthur

H.-P. Brack, M. Wyler[1], M. Slaski, G. Peter[1], G.G. Scherer
Wetting properties of membranes
Proc. 2nd European PEFC Forum, Luzern, June 30 - July 4, (ISBN 3-905592-13-4), **1**, 117-126 (2003).
[1] Zürcher Hochschule, Winterthur

F. Büchi, M. Ruge[1], A. Hintermann[2]
Schritte in Richtung Markt – Mobiler Stromgenerator PowerPac wird ausgezeichnet und präsentiert sich der internationalen Fachwelt in Hannover
ENET-NEWS **55**, 29 (July 2003).
[1] ETH Zürich
[2] BFE Bern

F. Büchi, M. Bärtschi, A. Tsukada, Ph. Dietrich, R. Kötz, G.G. Scherer, A. Wokaun, P. Rodatz, O. Garcia, L. Guzzella
Performance and operational characteristics of a hybrid vehicle powered by fuel cells and supercapacitors
Soc. of Automotive Engineers, 01-0418 (2003).

S. Freunberger, A. Tsukada, M. Santis, G. Fafilek[1], F.N. Büchi
1 + 1 Dimensional model for PE fuel cells of technical size
Proc. 2nd European PEFC Forum, Luzern, June 30 – July 4, (ISBN 3-905592-13-4), **1**, 383-389 (2003).
[1] Vienna University of Technology, Austria

V.-M. Graubner[1], R. Jordan[1], O. Nuyken[1], R. Kötz, Th. Lippert, B. Schnyder, A. Wokaun
Wettability and surface composition of poly(dimethylsiloxane) irradiated at 172 nm
Polym. Mat. Sci. and Eng. **88**, 488-489 (2003).
[1] TU Munich, Germany

L. Gubler, H. Kuhn, T.J. Schmidt, G.G. Scherer, H.-P. Brack, K. Simbek, T. Rager, F. Geiger
MEA based on radiation-grafted PSI-membrane: durability and degradation mechanisms
Proc. 2nd European PEFC Forum, Luzern, June 30 – July 4, (ISBN 3-905592-13-4), **1**, 69-77 (2003).

F. Hajbolouri, B.H. Andreaus, G.G. Scherer, A. Wokaun
Comparison of the temperature dependence of CO-poisoning for different anode electrodes in a polymer electrolyte fuel cell
Proc. 2nd European PEFC Forum, Luzern, June 30 - July 4, (ISBN 3-905592-13-4), **1**, 351-362 (2003).

F. Hajbolouri, B.H. Andreaus, G.G. Scherer, A. Wokaun
CO-poisoning in polymer electrolyte fuel cells studied by AC-impedance spectroscopy
Extended Abstracts, Fuel Cell Seminar, Miami Beach, USA, November 3-7, 53-56 (2003).

W. Josefowitz[1], H. Kranz[2], D. Macerata[3], T. Guth[4], H. Mettlach[5], D. Porcellato[6], F. Orsini[7], J. Hansson[8], P. Novák, E. Kelder[9], H. Döring[10], P. Blanchard[11], J. Kümpers[12]
EUCAR assessment and testing activities of advanced energy storage systems
AABC-3, Nice, France (2003).
[1] Volkswagen AG, Wolfsburg, Germany
[2] BMW AG, Munich, Germany
[3] Centro Ricerche Fiat, Torino, Italy
[4] DaimlerChrysler AG, Stuttgart, Germany
[5] Adam Opel AG, Rüsselsheim, Germany
[6] PSA Peugeot Citroën, Vélizy-Villacoublay, France
[7] Renault, Guyancourt, France
[8] Volvo AB, Göteborg, Sweden
[9] TU Delft, The Netherlands
[10] ZSW Ulm, Germany
[11] SAFT Bordeaux, France
[12] VARTA NBT, Hannover, Germany

R. Kötz, S. Müller, M. Bärtschi, B. Schnyder, P. Dietrich, F.N. Büchi, A. Tsukada, G.G. Scherer, P. Rodatz[1], O. Garcia[1], P. Barrade[2], V. Hermann[3], R. Gallay[3]
Supercapacitors for peak-power demand in fuel-cell-driven cars. In: Advanced batteries and super-capacitors
Edts. G. Nazri[4], R. Kötz, B. Scrosati[5], E.S. Takeuchi[6], The Electrochemical Society, Inc., Pennington, NJ, ECS Proceedings **PV 2001-21**, 564 (2003).
[1] ETH Zürich
[2] EPF Lausanne
[3] Maxwell Technologies SA, Rossens
[4] General Motors, Michigan, USA
[5] University of Roma, Italy
[6] Wilson Greatbatch, New York, USA

R. Kötz, M. Hahn, O. Barbieri, J.-C. Sauter, R. Gallay[1]
The electronic side of the double-layer: Impact on diagnostics and improvement of carbon double layer electrodes
Proc. 13th International Seminar on Double Layer Capacitors and Similar Energy Storage Devices, December 8–10, Deerfield Beach, USA, (2003).
[1] Maxwell Technologies SA, Rossens

D. Kramer, A. Geiger, A. Wokaun, G.G. Scherer
In situ visualisation of anodic two-phase flow patterns in a direct methanol fuel cell by neutron radiography and its influence on the current distribution
Proc. 2nd European PEFC Forum, Luzern, June 30 - July 4, (ISBN 3-905592-13-4) **2**, 565-574 (2003).

H. Kuhn, B.H. Andreaus, G.G. Scherer, A. Wokaun
Simultaneous local electrochemical impedance spectroscopy in polymer electrolyte fuel cells
Proc. 2nd European PEFC Forum, Luzern, June 30 – July 4, (ISBN 3-905592-13-4) **1**, 363-371 (2003).

N. Lempola, B. Steiger, G.G. Scherer, A. Wokaun
Metal oxides dispersed on Vulcan XC-72 as electrocatalysts for the oxygen reduction reaction in aqueous acidic electrolyte
Proc. 2nd European PEFC Forum, Luzern, June 30 - July 4, (ISBN 3-905592-13-4), **1**, 407-412 (2003).

T. Lippert
Excited materials
Materials Today **53**, March (2003).

M. Nagel[1], T. Lippert
Polymeric materials designed for laser ablation lithography (LAL) based on photosensitive triazene containing building blocks
Chimia **57**, 428 (2003).
[1] EMPA, Dübendorf

P. Rodatz[1], O. Garcia[1], L. Guzzella[1], F.N. Büchi, M. Bärtschi, A. Tsukada, P. Dietrich, R. Kötz, G.G. Scherer, A. Wokaun
Performance and operational characteristics of a hybrid vehicle powered by fuel cells and supercapacitors
Proc. of the Session "Fuel Cell Power for Transportation", SAE 2003 World Congress, Detroit MI, USA, March 3-6, paper 2003-01-0418, **1741**, 77-88 (2003).
[1] ETH Zürich

M. Ruge[1], M. Santis, G. Paganelli, D. Schmid[1], J. Hoffmann[1], F.N. Büchi
PowerPac – A portable fuel cell system with technological innovations
Proc. Fuel Cell World Conference 2003, The Fuel Cell World, Luzern, June 30 – July 4, 119–128 (2003).
[1] ETH Zürich

S. Salchenegger[1], W. Brandstätter[1], B.H. Andreaus, G.G. Scherer, P. Prenninger[2]
A one-dimensional computational model to study dehydration effects in polymer electrolyte fuel cells
Proc. 2nd European PEFC Forum, Luzern, June 30 - July 4, (ISBN 3-905592-13-4), **1**, 103-115 (2003).
[1] University of Leoben, Austria
[2] AVL-List, Graz, Austria

M. Santis, R.P.C. Neto[1], F.N. Büchi
Measurement of current density distribution in technical PE fuel cells
Proc. 2nd European PEFC Forum, Luzern, June 30 – July 4, (ISBN 3-905592-13-4), **1**, 391-397 (2003).
[1] Instituto Superior Téchnico, Lisboa, Portugal

M. Santis, D. Schmid[1], M. Ruge[1], S. Freunberger, F.N. Büchi
Modular stack-internal humidification concept – verification in an 1 kW portable system
Proc. 2nd European PEFC Forum, Luzern, June 30 – July 4, (ISBN 3-905592-13-4), **2**, 793-800 (2003).
[1] ETH Zürich

G.G. Scherer, B.H. Andreaus, D. Kramer, A. Geiger, H. Kuhn, A. Wokaun
In situ diagnostic methods for polymer electrolyte fuel cells
Extended Abstracts, Fuel Cell Seminar 2003, Miami, USA, November 3-7, 157-160 (2003).

J. Vetter, H. Buqa, D. Goers, A. Wuersig, P. Novák
Relationship of carbon structure and surface morphology to the formation and composition of the SEI layer
Lithium Battery Discussion - Electrode Materials, Extended Abstracts, Arcachon, France, Abstract No. 39 (2003).

F. Vogel, G.G. Scherer
Nachhaltige Verfahren der Wasserstofferzeugung und –nutzung
SATW-Bulletin **4/03**, 21 (2003).

TALKS

Invited Talks

H.-P. Brack
Radiation-grafted membranes: Investigations of structure-proberty relationships and fuel cell performance
Gordon Research Conference on Ion-Containing Polymers, Mount Holyoke College, South Hadley, MA, USA, July 16, 2003.

H.-P. Brack
The development and testing on proton-conducting polymeric membranes for application as electrolyte in fuel cells
DuPont Experimental Station, Wilmington, DE, USA, July 22, 2003.

F.N. Büchi, S. Freunberger
1+1 Dimensional model of a technical PEFC single cell
Computational Fuel Cell Dynamics-II, Banff, Canada, April 19-24, 2003.

F.N. Büchi, S. Freunberger
Investigation and analysis of in-plane inhomogeneity
Gordon Research Conference on Fuel Cells, RWU, Bristol, RI, USA July 27 - August 1, 2003.

F.N. Büchi
Brennstoffzellen: Technologie und Anwendungen
Faktor 4-Club Basel, June 12, 2003.

F.N. Büchi
Brennstoffzellen: Grundlagen und Anwendungen
13th Face to Face Meeting, HTI Biel, Biel, September 2, 2003.

F.N. Büchi
Diagnostics and modelling of PE-fuel cells
Seminar Festkörperphysik, Universität Fribourg, November 4, 2003.

N. Bukowiecki, J. Dommen, C. Ordóñez, A.S.H. Prévôt, E. Weingartner, U. Baltensperger
Räumliche und zeitliche Verteilung von Aerosolparametern im Raum Zürich
ACP Workshop 2003, Strassenverkehr und Luftqualität, ETH Zürich, September 11, 2003.

T. Lippert
Various applications of laser ablation
- EMPA Akademie, Dübendorf, January 2003.
- Institute of Optics, Madrid, Spain, March 2003.
- Data Storage Institute, National University of Singapore, July 2003.

T. Lippert
Inaugural lecture
The Poor Man's Star Wars-Laser Ablation und Ihre Anwendungen
ETH Zürich, June 17, 2003.

T. Lippert
Laser fabrication of microoptical elements in band-gap materials and polymers
XXIst International Conference on Photochemistry, Nara, Japan, July 2003.

T. Lippert
Thin epitaxial oxide films as model systems for electrocatalysts
The International Nanophotonics Symposium Handai, Osaka, Japan, July 2003.

T. Lippert
Fabrication of microoptical elements in UV transparent materials
6th International Symposium on Photoreaction Control and Photofunctional Materials, Tsukuba, Japan, October 2003.

P. Novák
Materialwissenschaftliche Herausforderungen auf dem Gebiet der Lithiumionen-Batterien
Materialforschungstag 2003, TU Darmstadt, Germany, October 15, 2003.

P. Novák
Graphitelektroden für Lithiumionen-Batterien
Vienna University of Technology, Austria, October 2, 2003.

P. Novák
Advanced in situ methods for the characterization of electroactive materials
International Workshop on Electrochemistry of Electroactive Materials WEEM-2003, Bad Herrenalb, Germany, July 26, 2003.

P. Novák
Advanced methods for in situ characterization of material-electrolyte interfaces in lithium-ion batteries
Meeting 'Developing an Atomistic Understanding of Materials for Energy Production and Storage', Rutherford Appleton Laboratory, Chilton, Oxfordshire, UK, March 6, 2003.

G.G. Scherer
Die Brennstoffzelle
Seminar für Institutionelle Anleger "Die Brennstoffzelle für die Erzeugung von Strom und Wärme im stationären, dezentralen Einsatz"
Bank Sal. Oppenheim jr. & Cie. (Schweiz) AG, Zürich, January 22, 2003.

G.G. Scherer
Research & development of electrochemical energy conversion and storage devices at Paul Scherrer Institut
Uppsala University, Angstrom Laboratory, Sweden, August 28, 2003.

G.G. Scherer, B.H. Andreaus, D. Kramer, A. Geiger, H. Kuhn, A. Wokaun
In Situ Diagnosemethoden für Polymer Elektrolyt Brennstoffzellen
Jahrestagung der Gesellschaft Deutscher Chemiker, Fachgruppe Angewandte Elektrochemie, Munich, October 6-11, 2003.

G.G. Scherer
A survey on polymer electrolyte fuel cell research at Paul Scherrer Institut
DuPont Central Research & Development, Experimental Station, Wilmington, DE, USA, October 31, 2003.

A. Wokaun
Fermentation fuels as a vector for using biomass in fuel cells
European Science Foundation, BFC Net Workshop, Genua, January 29-30, 2003.

Other Talks

H.P. Brack, L. Gubler
Performance and durability of MEAs based on the radiation grafted PSI membrane
Swiss Fuel Cell Research Symposium, Yverdon-Les-Bains, May 19-20, 2003.

F.N. Büchi
Current issues in PEFC research and development
Swiss Fuel Cell Research Symposium, Yverdon-les-Bains, May 19-20, 2003.

S. Freunberger, A. Tsukada, M. Santis, G. Fafilek[1], F.N. Büchi
1 plus 1 dimensional model of a technical PE fuel cell
203rd Meeting of the Electrochemical Soc., Paris, France, April 27 - May 2, 2003.
[1] Vienna University of Technology, Austria

S. Freunberger, A. Tsukada, M. Santis, G. Fafilek[1], F.N. Büchi
Water transport modelling for PEFC's of technical size
Swiss Fuel Cell Research Symposium, Yverdon-les-Bains, May 19-20, 2003.
[1] Vienna University of Technology, Vienna, Austria

L. Gubler
Diagnostic tools for MEA characterization
Swiss Fuel Cell Research Symposium, Yverdon Les Bains, May 19-20, 2003.

M. Hahn
Interfacial capacity and electronic conductivity of carbon double layer electrodes
GDCh-Jahrestagung Chemie Munich, October 6-11, 2003.
F. Hajbolouri, B.H. Andreaus, G.G. Scherer, A. Wokaun
CO-tolerance of commercial PtRu gas diffusion electrodes
Euromat 2003, Lausanne, September 1, 2003.

F. Hajbolouri
CO-tolerance of commercial fuel cell electrodes
Swiss Fuel Cell Research Symposium, Yverdon-Les-Bains, May 20, 2003.

M. Hauer, T. Lippert, A. Wokaun
Ns-surface interferometry measurements on designed and commercial polymers
7th International Conference on Laser Ablation, Hersonissos, Crete, Greece, October 2003.

M. Hauer, D.J. Funk[1], T. Lippert, A. Wokaun
Time resolved study of the laser ablation induced shockwave
E-MRS Symposium on Photonic processing of surfaces, thin films and devices, Strasbourg, France, June 2003.
[1] Los Alamos National Laboratory, USA

R. Kötz
The electronic side of the double-layer: Impact on diagnostics and improvement of carbon double layer electrodes
13th International Seminar on Double Layer Capacitors and Similar Energy Storage Devices, Deerfield Beach, USA, December 8–10, 2003.
[1] Maxwell Technologies SA, Rossens

G. Kopitkovas, T. Lippert, C. David, A. Wokaun, J. Gobrecht
Laser micromachining: fabrication of optical elements in quartz
CLEO/Europe-EQEC Symposium Surface and Volume Structuring, Munich, Germany, June 2003.

D. Kramer
Stoffverteilung in Direkt-Methanol Brennstoffzellen
8. Kolloquium Kraftfahrzeug- und Verkehrstechnik, Zwickau, Germany, January 15, 2003.

D. Kramer
Radiation-grafted membranes in direct methanol fuel cells
Swiss Fuel Cell Research Symposium, Yverdon-Les-Bains, May 19-20, 2003.

D. Kramer
In situ investigation of two-phase flow patterns by neutron-radiography
Swiss Fuel Cell Research Symposium, Yverdon-Les-Bains, May 19-20, 2003.

D. Kramer
In situ visualisation of anodic two-phase flow patterns in a direct methanol fuel cell by neutron radiography and its influence on the current distribution
2nd European PEFC Forum, Luzern, June 30 - July 4, 2003.

D. Kramer
Brennstoffzellen – Von den Grundlagen bis zur Anwendung
Workshop Klima- und Umwelttag, Thun, December 6, 2003.

H. Kuhn
Electrochemical impedance spectroscopy for polymer electrolyte fuel cells, applications to cells of technical interest
Swiss Fuel Cell Research Symposium, Yverdon-Les Bains, May 19-20, 2003.

M. Kuhnke, T. Lippert, G.G. Scherer, A. Wokaun
Microstructured glassy carbon model electrodes for fuel cells
Swiss Fuel Cell Research Symposium, Yverdon-les-Bains, May 19-20, 2003.

N. Lempola, B. Steiger, G.G. Scherer, A. Wokaun
Oxide catalyst for oxygen reduction
Swiss Fuel Cell Research Symposium, Yverdon-Les-Bains, May 19-20, 2003.

F. Raimondi, J. Wimmer, J. Wambach, A. Wokaun
Catalyst characterisation "NanoKat" (understanding heterogeneous catalysis on an atomic level)
1st Infrared Users Meeting, SLS, PSI Villigen, October 31, 2003.

M. Santis, D. Schmid[1], M. Ruge[1], S. Freunberger, F.N. Büchi
Stack and system concepts for PE fuel cell systems
Swiss Fuel Cell Research Symposium, Yverdon-les-Bains, May 19-20, 2003.
[1] ETH Zürich

M. Santis, D. Schmid[1], M. Ruge[1] S. Freunberger, F.N. Büchi
Modular stack-internal humidification concept - verification in a 1kW portable system
2nd European PEFC Forum 2003, Luzern, July 3, 2003.
[1] ETH Zürich

B. Schnyder
Investigation of the electrochemical behaviour of tungsten carbide with electrochemical and surface analytical methods
22nd European Conference on Surface Science, Prag, Czechia, September 7-12, 2003.

J. Vetter
Relationship of carbon structure and surface morphology to the formation and composition of the SEI layer
Lithium Battery Discussion - Electrode Materials, Arcachon, France, September 14-19, 2003.

J. Wambach
The SLS infrared beamline
1st Infrared Users Meeting, SLS, PSI Villigen, October 31, 2003.

A. Wokaun, F. Raimondi, J. Wambach
Structural modifications of model Cu/ZnO catalysts during methanol reforming
EuropaCat-VI Conference, Innsbruck, Austria, August 31 – September 4, 2003.

A. Würsig
Exfoliation of graphite negative electrode material in lithium-ion batteries: The in situ approach
GDCh Jahrestagung, Munich, Germany, October 6-11, 2003.

POSTERS

S. Alkan Gürsel, J.R. Reynolds[1]
High quality electrochromic polyfurans
Polymer Group of Switzerland (PGS) Spring Meeting 2003, Formulating Polymers for Product Design, Institute of Physics Auditorium, Fribourg University, May 9, 2003.
[1] University of Florida, Gainesville, FL, USA

S. Alkan Gürsel, J.R.Reynolds[1]
Conducting polymers as electrochromics
Polymer Group of Switzerland (PGS) Fall Meeting 2003, Functional Optical Polymers, EMPA Akademie, Dübendorf, November 28, 2003.
[1] University of Florida, Gainesville, FL, USA

Th. Dumont, T. Lippert, A. Wokaun, P. Leyvraz[1]
Laser writing of 2d data matrices in glass
E-MRS Symposium Photonic Processing of Surfaces, Thin Films and Devices, Strasbourg, France, June 2003.
[1] Frewitt Printing SA, Fribourg

Th. Dumont, S. Lazare[1], T. Lippert, A. Wokaun
Laser ablation of a photosensitive polymer: Differences between quartz crystal microbalance and atomic force microscopy
7th International Conference on Laser Ablation, Hersonissos, Crete, Greece, October 2003.
[1] Université de Bordeaux1, France

L. Gubler, T.J. Schmidt, G.G. Scherer, H.-P. Brack, K. Simbeck, T. Rager, F. Geiger, M. Arcaro
Performance and durability of MEAs based on the radiation grafted PSI membrane
Euromat 2003, 8th European Congress and Exhibition on Advanced Materials and Processes, Lausanne, September 1-5, 2003.

L. Gubler, T.J. Schmidt, H. Kuhn, G.G. Scherer, H.P. Brack, A. Wokaun
Performance and durability of membrane electrode assemblies based on radiation grafted proton exchange membranes
8th Grove Fuel Cell Symposium, London, UK, September 24-26, 2003.

L. Gubler, S. Alkan Gürsel, H.-P. Brack, G.G. Scherer
Radiation grafted membranes for polymer electrolyte fuel cells
Polymer Group of Switzerland (PGS) Fall Meeting 2003, Functional Optical Polymers, EMPA Akademie, Dübendorf, November 28, 2003.

M. Hahn, M. Baertschi, J-C. Sauter, O. Barbieri, R. Kötz
Interfacial capacity and electronic conductivity of carbon double layer electrodes
54th Annual Meeting of the International Society of Electrochemistry, Sao Pedro, Brazil, August 31 - September 5, 2003.

F. Hajbolouri, B.H. Andreaus, G.G. Scherer, A. Wokaun
CO-poisoning in polymer electrolyte fuel cells studied by AC-impedance spectroscopy
Fuel Cell Seminar, Miami Beach, USA, November 3-7, 2003.

S. Hochstrasser-Kurz[1], S. Virtanen[1], C. Jaeggi[2], N. Eichenberger[2], E. Szöcs[2], H. Siegenthaler[2], C. Stössel-Sittig, R. Kötz, B. Schnyder, P. Ziegler[3], I. Beltrami[3]
Corrosion aspects of the EDM process
Nanoconference St. Gallen, September 9-11, 2003.
1 ETH Zürich
2 University of Bern
3 AGIE SA, Losone

G. Kopitkovas, T. Lippert, C. David, A. Wokaun, J. Gobrecht
New concepts for a fabrication of micro-optical elements in UV transparent materials
E-MRS Symposium Photonic processing of surfaces, thin films and devices, Strasbourg, France, June 2003.

M. Kuhnke, T. Lippert, E. Ortelli[1], G.G. Scherer, A. Wokaun
Microstructuring of glassy carbon: comparison of laser machining and reactive ion etching
E-MRS Symposium Photonic processing of surfaces, thin films and devices, Strasbourg, France, June 2003.
1 Dyconex AG, Bassersdorf

M. Kuhnke, L. Cramer[1], T. Dickinson[1], T. Lippert, A. Wokaun
TOF-MS study of photoreactive polymers ablated by F_2 excimer laser (157 nm)
7th International Conference on Laser Ablation, Hersonissos Crete, Greece, October 2003.
1 Washington State University, USA

N. Lempola, B. Steiger, G.G. Scherer, A. Wokaun
Oxide catalyst for oxygen reduction reaction
Euromat 2003, Lausanne, September 2003.

K. Meissner[1], T. Lippert, D. Guenther[2], A. Wokaun
Analysis of trace metals in comparison of laser induced breakdown spectroscopy with LA-ICP-MS
E-MRS Symposium Photonic processing of surfaces, thin films and devices, Strasbourg, France, June 2003.
1 now Ivoclar Vivadent AG, Schaan, Lichtenstein
2 ETH Zürich

M.J. Montenegro, M. Döbeli[1], T. Lippert, S. Müller[2], A. Weidenkaff[3], P.R. Willmott[4], A. Wokaun
Microstructures and film properties of $La_{0.7}Ca_{0.3}CoO_3$
E-MRS Symposium Photonic processing of surfaces, thin films and devices, Strasbourg, France, June 2002.
1 ETH Zürich and PSI Villigen
2 Euresearch, Bern
3 University of Augsburg, Germany
4 University of Zürich and PSI Villigen

A. Mourato[1,2], A.S. Viana[1], R. Kötz, B. Schnyder, H. Siegenthaler[2],L.M. Abrantes[1]
In-situ SPM, voltammetric, and XPS studies of polyaniline films modified with sub-micrometer Pd Particles
54th Annual Meeting of the International Society of Electrochemistry, Sao Pedro, Brazil, August 31 - September 9, 2003.
1 Universidade de Lisboa, Portugal
2 University of Bern

M. Santis, G. Paganelli[1], D. Schmid[1], M. Ruge[1], J. Hoffmann[1], F.N. Büchi
PowerPac, portable fuel cell system with technological innovations
18th One Day Symposium, PSI Villigen, May 28, 2003
1 ETH Zürich

M. Seemann, S. Biollaz, Ch. Aichernig[1], H. Hofbauer[2], R. Koch[3]
Methanation of biosyngas in a bench scale reactor using a slip stream of the FICFB gasifier in Güssing
Energy Technologies for a Sustainable Future ETSF4, PSI Villigen, December 5, 2003.
1 Repotec Umwelttechnik GmbH, Güssing, Austria
2 Vienna University of Technology, Austria
3 Biomasse Kraftwerk Güssing GmbH, Austria

C. Stössel-Sittig, B. Schnyder, R. Kötz
XPS and AES characterisation of WC-Co after electro-discharge machining
10th European Conference on Applications of Surface and Interface Analysis, Berlin, Germany, October 5-10, 2003.
R.P.W.J Struis, O. Haas, A. Wokaun
EXAFS and XRD Investigation of $LaCoO_3$ Perovskite
4th SLS Users'Meeting, PSI Villigen, October 30-31, 2003.

L. Tiefenauer, C. Padeste, A. Grubelnik, B. Steiger
Charge transport in ferrocene-streptavidin monolayers
17th International Symposium on Bioelectrochemistry and Bioenergetics, Florence, Italy, June 19-24, 2003.

J. Vetter, H. Buqa, D. Goers, A. Wuersig, P. Novák
Relationship of carbon structure and surface morphology to the formation and composition of the SEI layer
Lithium Battery Discussion - Electrode Materials, Arcachon, France, September 14-19, 2003.

A. Züttel[1], R. Kötz, U. Vogt[2], F. Corti[3], R. Gallay[4]
Synthesis of supported, nanosstructured, high porosity carbon as electrode material.
Nanoconference St. Gallen, September 9-11, 2003.
1 University of Fribourg,
2 EMPA, Dübendorf
3 TIMCAL SA, Bodio
4 Maxwell Technologies SA, Rossens

PATENT APPLICATIONS

F.N. Büchi, S. Freunberger
Method and device for the stacking of fuel cells
European Patent Application Nr: PCT/EP03/07480, July 10, 2003.

CK Shin[1], G. Maier[1], G.G. Scherer
A block copolymer for use as a solid polymer electrolyte, an ion conductive membrane made from a block copolymer and methods of making a block copolymer
DP 102 58 175.4, eingereicht am 12.12.2002.
[1] TU München, Germany

CONFERENCES, WORKSHOPS & EXHIBITIONS

T. Lippert
Photon Processing of Surfaces, Thin films and Devices
E-MRS conference, Strasbourg, France, June 2003.
Co-chair of the symposium

T. Lippert
Lasers in Material Processing
CLEO/EQEC conference Munich, Germany, June 2003.
Member of program committee

P. Novák
International Scientific Committee of the "International Meeting on Lithium Batteries" conferences
Member

P. Novák
International Scientific Committee of the "International Battery Association" conferences.
Member

G. Paganelli
Exhibition of PacCar, experimental vehicle with PowerPac fuel cell
18th One Day Symposium, PSI Villigen, May 28, 2003.

M. Santis, F.N. Büchi
Exhibition of PowerPac project, including prototype
Fuel Cell 2003, Luzern, June 30 – July 4, 2003.

G.G. Scherer
European Fuel Cell Forum
Advisory Board

D. Schmid[1], M. Santis, M. Ruge[1], F.N. Büchi
Exhibition of PowerPac project, including prototype
Hannover Messe Industrie, Germany, April, 7-13, 2003.
[1] ETH Zürich

MEMBERSHIPS IN EXTERNAL COMMITTEES

R. Kötz
International Society of Electrochemistry
Chair, Division Officer, Division 3, Electrochemical Energy Storage and Conversion

and

Regional Representative of Switzerland

T. Lippert
Special issue: *Polymers and Light*
Springer Series *Advances in Polymer Science, Vol. 168*
Guest editor

T. Lippert
Special issue: *Photonic Processing of Surfaces, Thin Films and Devices*
Thin Solid Films
Elsevier Guest editor

T. Lippert
European Material Research Society
Board of Delegates

P. Novák
International Society of Electrochemistry
Member of Executive Committee (Treasurer) and Council

G.G. Scherer
Neuartige Schichtstrukturen für Brennstoffzellen
Deutsche Forschungsgemeinschaft, Mitglied der Prüfungsgruppe für das Schwerpunktprogramm

G.G. Scherer
Fuel Cell Handbook
Advisory Board

G.G. Scherer
Beirat Forschungsallianz Brennstoffzellen Baden-Württemberg, Germany
Deputy Speaker

G.G. Scherer
Fuel cells in a sustainable society
MISTRA – Foundation for Strategie Environmental Research, Sweden
Advisory Board

SCIENTIFIC CONTRIBUTIONS FROM THE ELECTROCHEMISTRY LABORATORY FOR THE PSI SCIENTIFIC REPORT 2003 VOLUME V, GENERAL ENERGY, ISSN 1423-7342

Please note that the following page numbers refer to the original page numbers in the PSI Scientific Report 2003, Volume V, General Energy.

Please cite the following contributions as indicated

Author, Title, ISSN No.

For example:

M.C. Bärtsch, P. Novák
Electrochemical characterization of phenolic based hard carbons
PSI Scientific Report 2003/ Volume V, ISSN 1423-7342, p. 79-80.

ELECTROCHEMICAL CHARACTERIZATION OF PHENOLIC BASED HARD CARBONS

M.C. Bärtsch, P. Novák

Phenolic resin is a very cheap precursor for the production of hard carbon, the latter being a promising candidate as future anode material in lithium-ion batteries. Hard carbon was produced under defined, reproducible conditions allowing electrochemical measurements for an in-depth investigation of this class of carbons. The electrochemical characterization of the carbon samples comprised constant current and constant potential measurements at different currents and potentials. The carbon samples were heat treated at different temperatures ranging from 650 °C to 1000 °C.

1 INTRODUCTION

Lithium-ion batteries are the most used energy sources in mobile phones and portable computers. They offer at the same time excellent energy and power specifications and have played a decisive role in the stormy dissemination of mobile electronic devices. Nevertheless, research continues to develop lithium-ion batteries with even higher specific capacities in order to meet the demands of modern electronic devices, like laptops, digital cameras and mobile phones.

The negative electrode of today's lithium-ion batteries contains a mixture of graphite and mesocarbon micro beads (MCMB). The maximum specific charge of graphite is 372 Ah/kg, the one of MCMB is even smaller. Several experiments on hard carbons show, however, that much higher specific charges are possible [1,2]. Unfortunately, the gain of specific charge resulted in much higher irreversible capacities and worse cycling behaviour. In order to eliminate these disadvantages, much better understanding of the hard carbon properties is necessary, that means controlled production and tests.

2 EXPERIMENTAL

We used a commercially available phenolic resin (PF 0434 SW 08, Bakelite AG, Germany) as precursor for the hard carbon production. The fabrication of the final carbon powder consists of four process steps each of them having a set of parameters which may influence the final quality of the hard carbon powder (Figure 1). The phenolic resin was spread to about a 1 mm thick layer on a Teflon plate. The important curing step included slow heating up to 200 °C in air within 12 hours (3-dimensional cross-linking). The brittle resin layer was then broken into little pieces and ground to granules by means of an herb-mill. 5 g of the granulate material was filled into a self-made stainless steel pyrolysis chamber (Figure 2). Pyrolysis was performed by flooding the chamber with Argon gas (0.5 L/min) and heating in a muffle oven to the final heat-treatment temperature (HTT). The heating rate was 10 °C/min and the HTT was maintained for 30 minutes. The pyrolysis chamber was flooded with Ar until the temperature dropped to ambient temperature. The HTT ranged from 650 °C to 1000 °C in 50 °C steps. The higher the HTT the more intense the crystalline shine of the black pyrolysis product, which was afterwards ground in a planetary ball mill to a fine carbon powder.

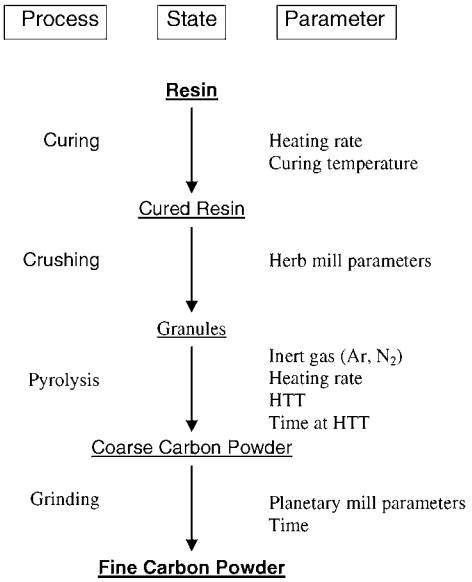

Fig. 1: Manufacturing of phenolic resin in four steps to a fine hard carbon powder.

The carbon samples were worked up to electrodes for testing in lithium half-cells (counter and auxiliary electrodes were made from lithium, working electrode was the carbon sample). LP30 electrolyte (Merck KGaA, Germany) was used in all measurements as standard electrolyte. The samples were electrochemically tested by cycling the half-cells between 1.5 V and –5 mV vs. Li/Li^+ (lithium plating of the working electrode occurs at much lower negative potentials). Charging/discharging was performed according to the constant current/constant potential method (CCCP). The constant current was 10 µA/mg in the first (formation) cycle and five times higher for the following ones. Constant potential was applied after reaching 1.5 V and –5 mV until the current dropped below 10 µA/mg. The half-cells were cycled one hundred times.

3 RESULTS

Figure 3 shows the cycling behaviour of the hard carbon sample heat-treated at 700 °C. The irreversible capacity of the first cycle is typical for that of a hard carbon sample and lies in the range of 50 %. In the course of the following cycles, the irreversible capacity

dropped quickly to values typical for graphite electrodes. The irreversible capacities yield 0.5% and only 0.3% for the 20th and 80th cycle, respectively.

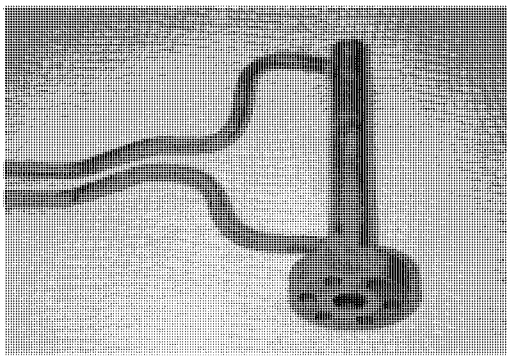

Fig. 2: Stainless steel pyrolysis chamber with inert gas supply. Capacity of about 5 g cured precursor.

The negative potential edge was changed from –5 mV to –20 mV after the 69th cycle. The enlargement of the potential window resulted in an increase of the specific capacity of 9%. Interestingly, this potential change seems also to have a positive effect on the cycling stability. The specific discharge capacity yields 278 Ah/kg at the 80th cycle (-20 mV potential edge).

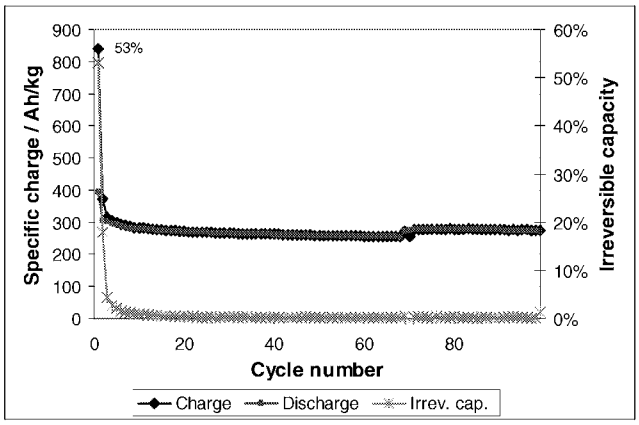

Fig. 3: Cycling behaviour of a hard carbon sample heat-treated at 700 °C. The higher specific charge after the 69th cycle is due to the change of the negative potential edge from –5 mV to –20 mV vs. Li/Li+.

Figure 4 shows the specific discharge capacity values of the 80th cycle as a function of the heat-treatment temperature. The values refer to the potential range between –5 mV and 1.5 V vs. Li/Li+. According to the maximum of the BET surface and micropore volume values at about 700 °C of pyrolysed phenolic resin [3], we also expect a maximum for the discharge capacities at this temperature because of the additional insertion sites for lithium ions in the open pore hard carbon structure. The lithium ions can not only intercalate in the graphene ribbons forming the disordered hard carbon structure but also adsorb at the edges of the ribbons and insert into the pores. The minimum at around 900 °C reflects the change of an open pore structure to a closed one by increasing the HTT. Following the idea of the three-dimensional structural model for isotropic hard carbon (glassy carbon) we would expect the discharge capacity to have its maximum at 700 °C due to the closure of the pores at higher HTT. Astonishingly, the values of the 950 °C and 1000 °C samples increase again! To explain this interesting feature and to find out the optimum parameter set, the experiments have to be continued to higher HTT.

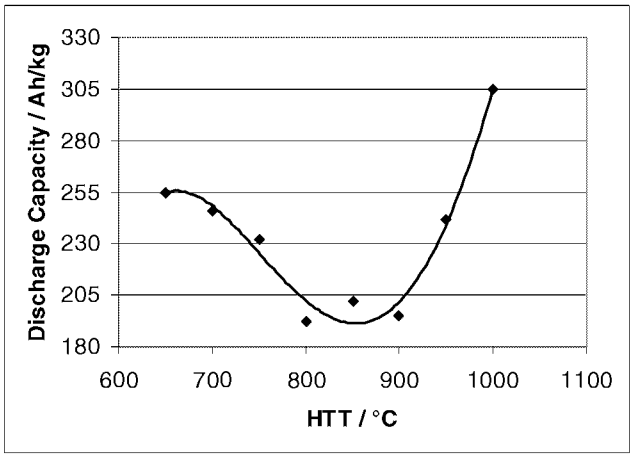

Fig. 4: Discharge capacity values of the 80th cycle as a function of the heat-treatment temperature (HTT). The discharge capacity refers to the potential window between –5 mV and 1.5 V vs. Li/Li+. The fitting curve is a polynomial of 4th order.

4 CONCLUSIONS

Phenolic resin is an ideal precursor for defined manufacturing of hard (glassy) carbon. It excels not only by the high carbon yield after pyrolysis of about sixty percent but also by the comparatively low price and by its pureness.

There are a lot of parameters that may influence the (electrochemical) characteristics of the fine carbon powder to be used as anode material in lithium-ion batteries. A strict control of these parameters is, however, necessary to obtain reliable and reproducible results.

The 700 °C sample shows that two of the four goals were reached: The sample exhibits a stable cycling behaviour, and very low irreversible capacities are measured for higher cycling numbers. What still should be improved are the irreversible capacities at the beginning and the specific charge. These are typical issues of parameter optimisation.

5 REFERENCES

[1] S. Yata et al., Synth. Met. **62**, 153 (1994).

[2] N. Sonobe et al., Ext. Abstr., 35th Battery Meeting, Nagoya, Japan, 49 (1994).

[3] G.M. Jenkins and K. Kawamura, Polymeric carbons – carbon fibre, glass and char, Cambridge University Press (1976).

IN SITU RAMAN STUDIES OF PHENOLIC RESIN BASED HARD CARBON

D. Goers, L.J. Hardwick, P. Novák

Hard carbons made from phenolic resin by pyrolysis are characterised using Raman spectroscopy. To describe the Raman spectra, a model containing four bands (G, D, M1, M2) was used. The behaviour of a hard carbon sample during electrochemical cycling was studied at different positions on the electrode using in situ confocal Raman spectroscopy. During lithium insertion, the centre of the band shifts to lower wavenumbers and the ratio of the D and G band, R_{DG}, significantly increases. After lithium extraction, the centre of the G band and the ratio R_{DG} do not return to their original values, due to irreversible structure changes and trapped lithium in the hard carbon.

1 INTRODUCTION

Lithium-ion batteries frequently contain a carbonaceous material, usually graphite, as the electroactive material for the negative electrode.

In recent years there has been increased interest in utilizing pyrolyzed polymers, such as polyparaphenylene, epoxy resin, and phenolic resin, for this purpose [1]. Pyrolysis of these polymers usually produces hard carbons, which contain several voids and only a small amount of stacked graphene layers. Different models have been developed to explain the insertion of lithium ions into this structure. These models include lithium storage on the surface sites, lithium intercalation, as well as lithium storage in cluster gaps, micro voids or atomic defects.

Microstructural parameters have a strong influence on the lithium insertion mechanism and affect the electrochemical behaviour of hard carbons. To better understand the correlations between structural and electrochemical parameters Raman spectroscopy was used to characterise the structure of hard carbons made by pyrolysis of phenolic resin.

2 EXPERIMENTAL

Preparation and physical properties

A 1 mm thick layer of phenolic resin (Bakelite AG) was subjected to curing. The sample was heated for 12 h from 20 °C to 200 °C. The cured resin was broken into small pieces and milled into a coarse powder. The samples were heat-treated in an argon atmosphere at a temperature rate of 10 K/min and maintained at the heat-treatment temperature (HTT) for 30 minutes. Hard carbon powder was ground for 30 minutes in a planetary mill to give particles in the size range of 1-20 µm.

Raman Spectroscopy

A confocal Raman microscope (Labram, Jobin Yvon, ex DILOR Instruments SA) was used to acquire Raman spectra of the hard carbon powders and electrodes. Electrodes were prepared by pressing a small amount of the electrode mixture (90 % active material, 10 % Teflon binder) into the hole of a copper current collector to allow the observation of the active material *in situ* from the backside of the electrode. An internal HeNe laser at 632.8 nm with approximately 2.5 mW power was used for *ex situ* measurements. During *in situ* Raman spectroscopy, the laser power was reduced to 0.9 mW using a neutral filter. The Raman spectra were recorded in the spectral range from 1000 to 1900 cm^{-1} with a resolution of 4 cm^{-1}. Raman band positions were calibrated against the spectrum of a neon lamp (Penray, Oriel). For *in situ* measurements, the electrochemical cell was charged and discharged by a computer-controlled cell capture (CCCC, Astrol Electronics AG).

3 RESULTS AND DISCUSSION

Ex situ Raman Spectroscopy

Detailed peak-fitting analysis reveals the presence of four bands in almost all hard carbon samples (Figure 1). This is in agreement with other Raman studies of phenolic resin based materials. The pioneering work of Tuinstra and Koenig suggests that, the G band, at ca. 1580 cm^{-1} (E_{2g}), originates from in-plane vibrations of atoms arranged in a large network of perfectly condensed aromatic rings and is found in all graphitic samples such as carbon black, hard carbons, and fibres [2, 3]. This band can be attributed to carbon atoms in the sp^2 electronic configuration.

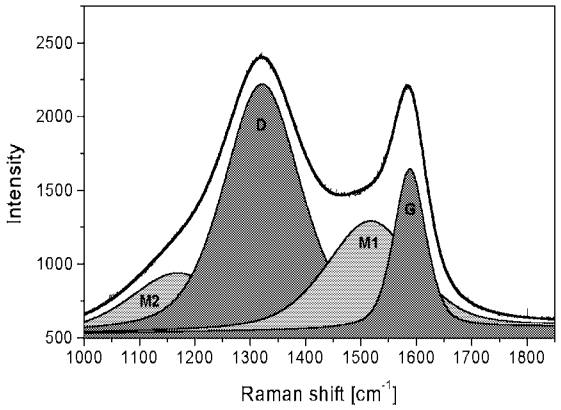

Fig. 1: Band deconvolution of a typical hard carbon Raman spectrum.

The D band, observable at 1330 cm^{-1}, is not an original Raman-active mode (A_{1g}). It is often attributed to some kind of disorder and imperfection in the graphitic material. The origin of this band is quite complex and connected with a breakdown of the local symmetry of the graphite structure [2, 3]. In particular, the D band can also be attributed to carbon atoms appearing in the sp^3 electronic configuration.

The two additional bands M1 and M2 needed to fit the Raman spectra were found to be present in hard carbons only. The broad band M1 was fitted as the sum of a Lorentzian and a Gaussian function. It originates from various compounds resulting from the pyrolytic degradation. The band M2, best fitted using a Gaus-

sian function, probably represents various disordered structures containing condensed aromatic rings.

In situ Raman Spectroscopy

Figure 2 shows a series of Raman spectra measured during the first lithium insertion of hard carbon sample prepared with a heating rate of 5 K/min at 800 °C. Lithium insertion and extraction was done with a C/5 rate and analogous to graphite, a 1:1 (w/w) mixture of ethylene carbonate (EC) and dimethyl carbonate (DMC) with 1M $LiClO_4$, was used as the electrolyte. The G band at 1580 cm^{-1} shifts to lower wavenumbers with decreasing potential vs. Li/Li^+ and the intensity ratio R_{DG} is increasing. The analysis of the band deconvolution of the *in situ* Raman spectra suggests only small variations of the M1 and M2 bands during lithium insertion.

Some spectra of this hard carbon sample suggest the presence of a fifth band, M3, to allow a perfect fit of the spectra and provide a low χ^2 value. This band is usually located very close to the D band around 1330 cm^{-1} and fits best using the Gaussian function. The origin of the M3 band is still not yet clear. If the best fit of the Raman spectra is obtained by including the M3 band, then the M3 band is also considered in the intensity ratio to allow comparability of peak-fitting results.

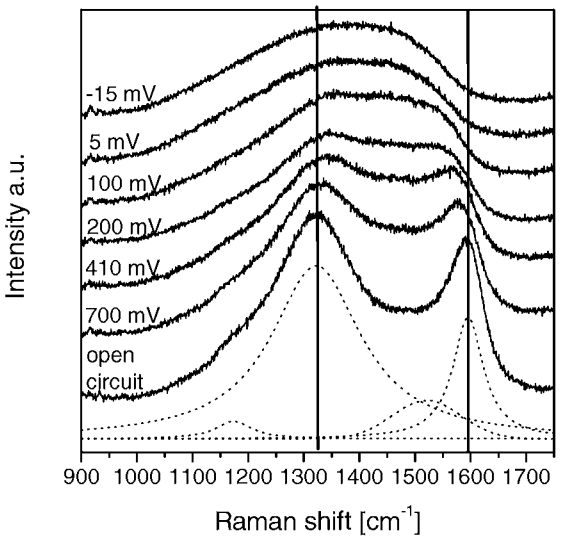

Fig. 2: Typical *in situ* Raman spectra of hard carbon during lithium insertion.

It should be noted that because of the cell design the overpotential strongly depends on the position on the electrode, resulting in a spatial distribution of the lithium content. A series of Raman spectra were measured at different positions on the electrode surface. They reveal small changes in the associated cell voltage due to different lithium content. It was found that the given series of Raman spectra in Figure 2 represents most of the electrode positions.

Figure 3 shows the shift of the G band to lower wavenumbers during lithium insertion. The shift can be explained by the interaction of adsorbed and/or intercalated lithium atoms with the C-C bonds of the hard carbon. This affects the force constant of the C-C vibrations and shifts the related G band to lower wavenumbers. During lithium extraction, the G band shifts back to higher wavenumbers (Figure 3).

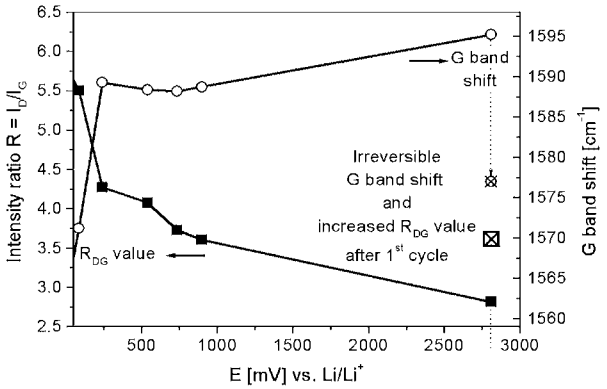

Fig. 3: Increase of the R_{DG} value and the shift of the G band to lower wavenumbers during lithium insertion. The values after the first lithium extraction indicate irreversible behaviour.

After complete lithium extraction, the centre of the G band remains shifted to lower wavenumbers compared to the initial band position before the first lithium insertion. One could assume that this is because of irreversible structural changes during the first lithium insertion and of trapped lithium into collapsed micropores.

An increase in the intensity ratio R_{DG} was observed during lithium insertion (Figure 3). The increased relative D band intensity can be explained by the distortion of the local symmetry of the graphene sheets due to adsorbed or intercalated lithium atoms and collapsed micropores and crystallites. In agreement with the results related to the shift of the G band, the individually ratio $R_{DG} = I(D)/I(G)$ of each measurement position does not decrease during lithium extraction to the original value. This result supports the described theory of irreversible structure changes and trapped lithium atoms.

4 ACKNOWLEDGEMENTS

We wish to thank Richard Lachmann for the preparation of the phenolic resin hard carbons. The financial support of the Swiss National Science Foundation is also gratefully acknowledged.

5 REFERENCES

[1] K. Sato, M. Noguchi, A. Demachi, N. Oki, M. Endo, Science **264,** 556 (1994).

[2] F. Tuinstra, J.L. Koenig, J. Chem. Phys. **53,** 1126 (1970).

[3] D. Goers, M.C. Bärtsch, A. Würsig, L. Hardwick, P. Novák, Proc. Electrochem. Soc. in print, (2004).

SEM INVESTIGATIONS ON MODIFIED GRAPHITE ELECTRODES FOR LITHIUM-ION BATTERIES

J. Vetter, H. Buqa, D. Goers, A. Würsig, F. Krummeich (ETH Zürich), P. Novák

The solid electrolyte interphase (SEI) layer, i.e. the passivation layer formed on the surface of the carbonaceous negative electrode material, is the key component in the negative electrode, determining electrochemical performance and safety of the whole lithium-ion battery. A clear identification of all components of the SEI is important for thorough understanding and further improvements of lithium-ion batteries. Structure and chemistry of the carbonaceous bulk material play an important role in SEI formation.

1 INTRODUCTION

Models assume that the SEI is composed of two major constituents described as inorganic and organic interpenetrating layers [1]. The composition of the inorganic layer is fairly well known, but understanding the organic layer is still a challenge because common surface analytical methods exposing the SEI film to vacuum cause severe changes within the layer.

Both, surface chemistry and morphology of graphite play a major role in chemical and electrochemical reactivity and interaction with SEI products. Graphite has two kinds of surfaces, basal planes which mainly consist of carbon atoms and prismatic edge planes which include various functional surface groups, mostly containing oxygen and/or hydrogen atoms. In short, morphology, chemical composition, ratio of prismatic to basal planes, defects, etc. of carbon material have a significant impact on negative electrode performance in lithium-ion batteries, namely on the formation of the SEI. On prismatic edges and structural defects the growth of the layer is initiated. The ratio of edge planes to basal planes influences the extent of electrolyte decomposition [2]. Surface morphology and the chemistry of functional groups present at the surface determine electrochemical stability and decomposition pathways of the electrolyte and, thus, composition and properties of the SEI.

2 GRAPHITE TREATMENT

To enforce significant changes in the electrochemical behavior of synthetic graphite, drastic methods have to be applied. By treatment of graphite with air, ozone, ammonia, hydrogen, silane, and other gases, surface chemistry and morphology can be altered, leading to an improvement of the graphite's electrochemical behavior [3,4]. Since surface groups are scarce on graphite, most surface analytical techniques fail due to their detection limit, and it is hard to find suitable methods to detect any changes. However, correlation of crystallite structures and morphology with electrochemical behavior can give valuable information on changes during heat treatment and oxidation.

For this study, we chose synthetic TIMREX® SLX50 graphite (TIMCAL SA, Bodio) as the starting material. The graphite was treated in a muffle furnace with (moist) air at various temperatures between 500 and 800 °C. During the process, the graphite was oxidized at the surface, indicated by a mass loss of 3.3-34.0 %.

The oxidized samples were characterized by XRD, Raman, and SEM, and investigated by electrochemical cycling against lithium in various electrolytes.

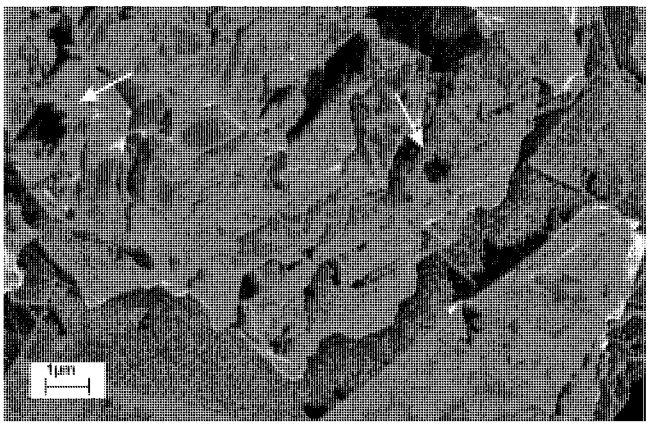

Fig. 1: SEM image of SLX50 graphite after oxidation at 700 °C. The prismatic edge planes are corroded. Jagged surface with deep holes (arrows).

3 SURFACE MODIFICATIONS

Scanning electron microscope (SEM) pictures show large cavities and holes for samples oxidized in the muffle furnace at temperatures above 700 °C (Figure 1). Material loss due to oxidation is observed especially at the graphite edge planes, leading to rough, jagged surfaces (Figures 1+2).

Raman spectroscopy of graphites treated in the muffle furnace indicates a slight increase of the crystallite size L_a in the surface region. This can be explained by the preferred burn-off of smaller particles containing small crystallites. With XRD, no changes in crystallite

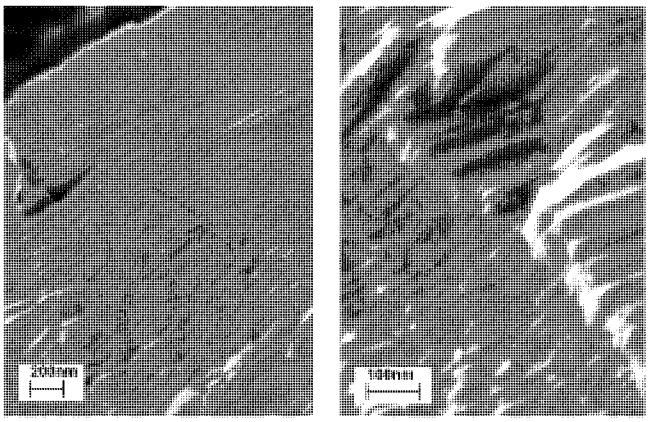

Fig. 2: SEM images of the prismatic edge plane of SLX50 oxidized at 800 °C. The formerly smooth edge planes are roughened.

size (L_a or L_c values) could be observed. This may be due to the fact that the oxidative treatment only affects the surface of the particles, while with XRD the bulk material is examined [5]. As expected, the rhombohedral fraction of SLX50 decreases with raising treatment temperature

4 ELECTROCHEMICAL RESULTS

To investigate the electrochemical behavior of the oxidized graphite, galvanostatic cycling experiments were performed using a solution of $LiPF_6$ in ethylene carbonate (EC) and dimethyl carbonate (DMC) as the electrolyte and metallic lithium as the counter and reference electrode.

In Figure 3 the 1st galvanostatic charge/discharge cycle of half cells with graphites oxidized at different temperatures is shown. Samples treated at temperatures up to 600 °C show the same electrochemical

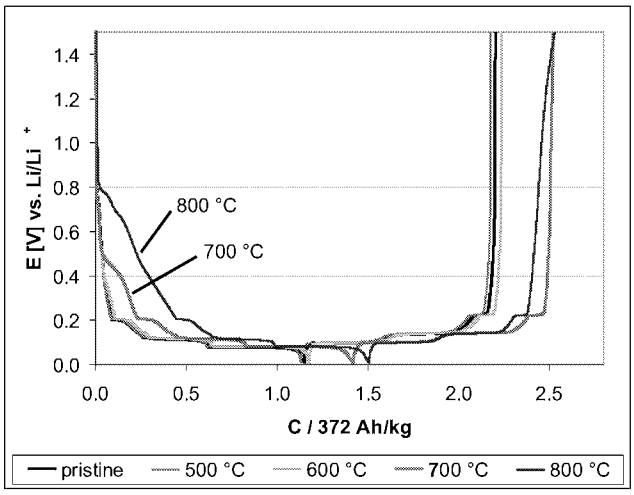

Fig. 3: 1st galvanostatic cycle of SLX50 oxidized at various temperatures (1*M* $LiPF_6$, EC/DMC 1:1).

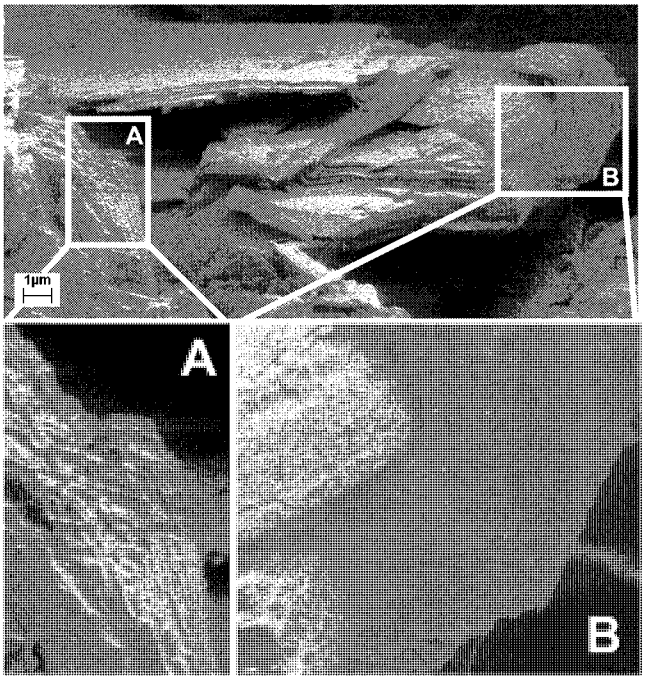

Fig. 4: SEM image of an electrode of SLX50, oxidized at 700°C, after the 1st charge to 300 mV in EC/DMC 1:1, 1*M* $LiPF_6$ vs. Li.

behavior as the pristine material. In samples treated at 700 °C, an additional plateau is observed in the curves. With increasing oxidation temperature the potential plateau grows and shifts to 0.8 V vs. Li/Li^+. This potential is usually associated with the exfoliation of graphite [6].

Post mortem SEM images (Figures 4) after cycling of the electrodes with the graphite treated at 700 °C show the beginning of the process. Some of the particles of the electrode (region A) are widened up and cracked at the prismatic edges, while others (region B) show no signs of exfoliation.

When electrolytes containing propylene carbonate (PC) are used, exfoliation is as expected the dominant process. Figure 5 shows a post mortem SEM image of these electrodes. The extreme exfoliation and the distinct separation of the graphite layers are clearly visible. Furthermore, the polymer-like behavior of the SEI formed under these conditions becomes obvious, since filament-like connections (indicated by arrows) between the graphite layers can be observed.

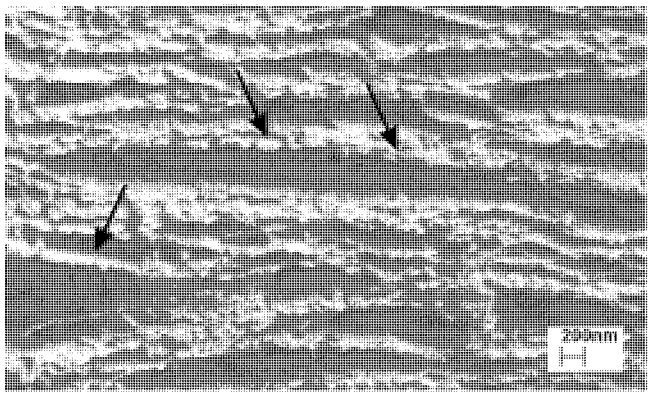

Fig. 5: SEM image of SLX50, oxidized at 500°C, after the 1st charge to 300 mV in EC/PC 1:1, 1*M* $LiPF_6$.

5 ACKNOWLEDGMENTS

Parts of this work were done under the auspices of the Swiss National Science Foundation. We want to thank the TIMCAL Group, Bodio, Switzerland, namely Dr. M. Spahr for support and valuable discussions.

6 REFERENCES

[1] D. Aurbach, B. Markovsky, I. Weissman, E. Levi, Y. Ein Eli, Electrochim. Acta **45**, 67 (1999).

[2] M. Winter, P. Novak, A. Monnier, J. Electrochem. Soc. **145**, 428 (1998).

[3] H. Buqa, P. Golob, M. Winter, J.O. Besenhard, J. Power Sources **97-98**, 122 (2001).

[4] H. Buqa, C. Grogger, M.V.S. Alvarez, J.O. Besenhard, M. Winter, J. Power Sources **97-98**, 126 (2001).

[5] D. Goers, H. Buqa, L. Hardwick, A. Wuersig, P. Novak, Ionics **9**, 258 (2003).

[6] J.R. Dahn, A.K. Sleigh, H. Shi, B.M. Way, W.J. Weydanz, J.N. Reimers, Q. Zhong, U. von Sacken, *Carbons and graphites as substitutes for the lithium anode*, in Lithium batteries - new materials, developments and perspectives, Elsevier, Amsterdam, 1 (1994).

IN SITU INVESTIGATION OF GRAPHITE EXFOLIATION IN LITHIUM-ION BATTERIES

A. Würsig, H. Buqa, M.E. Spahr (TIMCAL SA), P. Novák

Post mortem scanning electron microscopy (SEM) and X-ray diffraction (XRD) analysis were used to investigate the exfoliation process on highly crystalline synthetic graphite. Differential electrochemical mass spectrometry (DEMS) was applied to study the gas evolution during the passivation of the graphite surface. The reduced reactivity of a heat-treated graphite surface towards SEI formation was correlated with the exfoliation of the graphite structure during the first electrochemical reduction.

1 INTRODUCTION

Graphitic carbons are the first choice material as negative electrode in lithium-ion batteries, for reasons of high performance and low cost. Polycrystalline graphite, with a high graphitization degree, is one of the most attractive examples of these materials with a theoretical reversible capacity of 372 mAh/g. One disadvantage of these materials is the exfolation tendency in electrolytes based on organic carbonates. To prevent the material from exfoliation, a protective film, the so-called solid electrolyte interphase (SEI), needs to be formed during the first electrochemical reduction. The formation of this passivation film from organic and inorganic electrolyte decomposition products and finally the exfoliation can be influenced by properties of the graphite material such as surface chemistry, defect structures, and morphology. The exact mechanism is still not well understood. To enhance the knowledge about the exfoliation process different *in situ* methods were applied [1].

2 EXPERIMENTAL

Synthetic graphite TIMREX® SLX50 (TIMCAL) was heated at 3000 °C in an inert helium gas atmosphere for 2 weeks. The product SLX50 (HT) and the untreated material were investigated by X-ray powder diffraction (XRD), scanning electron microscopy (SEM) and differential electrochemical mass spectrometry (DEMS).

3 RESULTS

In the case of SLX50 (HT), galvanostatic measurements show an additional distinct potential plateau at about 400 mV *vs.* Li/Li^+. This leads to a high irreversible charge loss within the formation cycle. To confirm whether or not this plateau can be explained by exfoliation of the graphite material, *post mortem* XRD measurements were performed. The electrodes were stabilized at 600 mV and 300 mV *vs.* Li/Li^+. The result can be seen in Figure 1. The broadening of the (002) Bragg reflection at 300 mV indicates that the exfoliation takes place between these two potentials.

To evaluate the effect of graphite exfoliation on the morphology, *post mortem* SEM images of stabilized electrodes were recorded. An example picture, which displays the effect of exfoliation, is shown in Figure 1. The graphene layers are greatly widened and at some points big caverns arise. Filament like residues of the SEI are recognizable between single layers (arrows). This indicates that the electrochemical graphite exfoliation is caused by the intercalation of the SEI between the graphite layers, as suggested by *Besenhard* et al. [2]. DEMS measurements were performed to monitor the ethylene gas evolution of SLX50 and SLX50 (HT) during the formation cycle, due to electrolyte decomposition and graphite surface passivation in EC-based electrolyte systems. Figure 2 shows the results of these measurements using EC/DMC 1:1, 1*M* $LiPF_6$ as electrolyte. With untreated SLX50, the maximum of ethylene gas formation is reached at 530 mV *vs.* Li/Li^+. In the case of SLX50, (HT) which possesses a lower reactive graphite surface, the maximum is observed at a less positive potential of about 280 mV. Since exfoliation starts at a higher potential it cannot be hindered by the SEI formation.

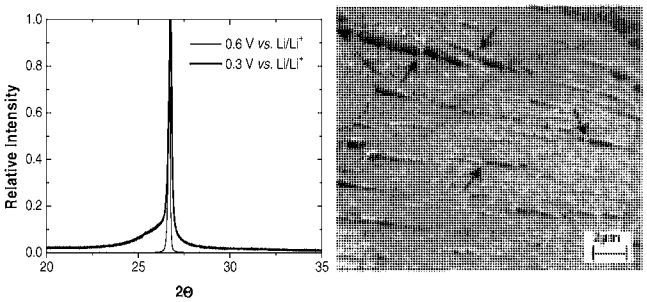

Fig. 1: (002) X-ray diffraction peak of heat-treated SLX50 (HT) graphite (l.) and SEM images of exfoliated SLX50 (r.).

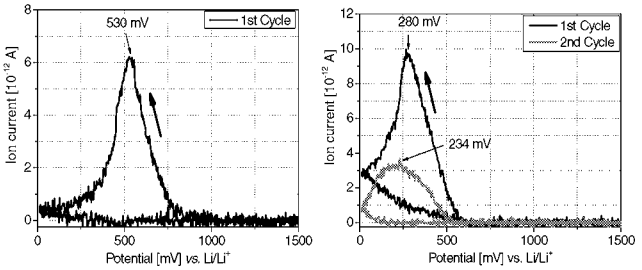

Fig. 2: DEMS measurements of TIMREX® SLX50 (l.) and SLX50 (HT) (r.).

4 ACKNOWLEDGEMENT

The financial support of the Swiss National Science Foundation is gratefully acknowledged.

5 REFERENCES

[1] M.E. Spahr, et al., J. Electrochem. Soc., submitted for publication.

[2] J.O. Besenhard, et al., J. Power Sources **54**, 228 (1995).

MALEIC ANHYDRIDE AS FILM-FORMING ELECTROLYTE ADDITIVE IN LITHIUM-ION BATTERIES

J. Ufheil, M.C. Bärtsch, A. Würsig, P. Novák

The effect of maleic anhydride (MA) as film-forming additive in gamma-butyrolactone (GBL) based electrolytes for use in Li-ion batteries was investigated. Cyclic voltammetric (CV) measurements and charge - discharge cycling tests showed that the presence of small amounts of MA improve the reversibility of lithium intercalation into graphite.

1 INTRODUCTION

Lithium-ion batteries are often restricted in use to a narrow temperature window. This is because the electrolyte must remain liquid with a low viscosity and a high dissociation power for good electrical conducting properties. An interesting solvent in the field of Li-batteries is therefore GBL. The good physical properties of GBL that include a wide liquid range lead to an attractive electrolyte system for electrode research and development [1]. However, graphite anodes with GBL and $LiClO_4$ as solute show a large irreversible charge capacity during the first cycle and poor cycleability. Our present work described the influence of MA as additive in GBL based electrolytes to improve the features of lithium-ion batteries.

2 EXPERIMENTAL

Electrochemical experiments were performed in standard cells at room temperature as described elsewhere [2]. Working electrodes were prepared by doctor blading natural graphite with polyvinylidene fluoride binder onto a copper current collector. The electrodes were vacuum dried at 120 °C and they contained ca. 10 mg of graphite. Li foils were used for both the reference and counter electrode.

3 RESULTS

Half cells composed of graphite and lithium with a glass fleece as separator to separate the anodic and cathodic compartments were used for the electrochemical experiments. Firstly CV measurements were used to investigate the influence of MA to the kinetic abilities of the battery system.

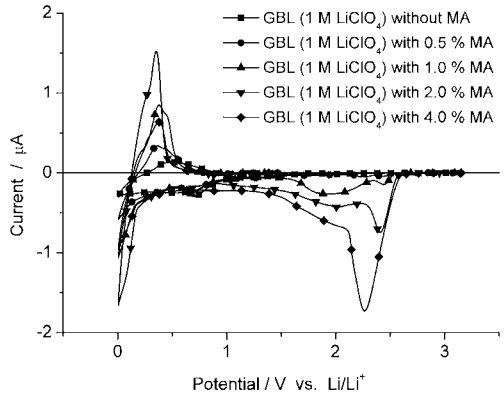

Fig. 1: Current-potential characteristics of different MA concentrations in GBL (1 M $LiClO_4$). Sweep rate was 100 µV/s. The scan started from open circuit potential (2.7 - 3.1 V vs. Li/Li^+). Symbols designate different MA concentrations.

Figure 1 shows CV measurements with different MA concentration in GBL with 1 M $LiClO_4$. Without MA the lithium intercalation and extraction peak (1 - 0.1 V) is poor which indicates slow kinetics. With the presence of MA an increase of the lithium intercalation and extraction peaks was observed. Optimum results were obtained with use of a MA concentration of 2%. This result originates from the MA decomposition products, which were generated about 2.3 V and formed a film at the electrode surface.

In Figure 2 the charge capacity and the irreversible charge loss are reported vs. the cycle number at 25 °C. It is obvious, that the behaviour of the cells has been improved by the addition of MA. This is due to the fact that charge capacity remains more constant and converges towards a constant value over the entire cycling test. Furthermore the irreversible charge loss is significantly reduced with use of MA.

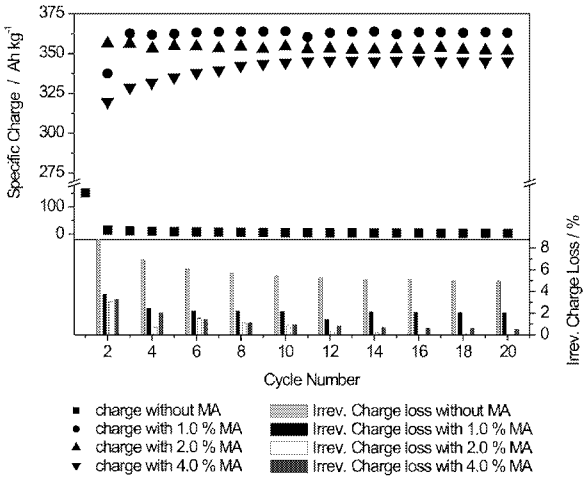

Fig. 2: Cycling behaviour of electrodes in GBL with 1 M $LiClO_4$ as solute with different MA concentrations.

In conclusion the charge/discharge cycling tests of the graphite electrodes described above indicates that the presence of MA in solution has two positive impacts, decrease of the irreversible capacity of the electrodes and improvement of their cycleability.

4 REFERENCES

[1] M. Lanz, P. Novak, J. Power Sources **102**, 277 (2001).

[2] P. Novak, W. Scheifele, F. Joho, O. Haas, J. Electrochem. Soc. **142**, 2544 (1995).

RECENT IMPROVEMENTS IN THE ELECTROCHEMICAL PERFORMANCE OF GRAPHITE ELECTRODE FOR LITHIUM-ION BATTERIES

H. Buqa, D. Goers, M.E. Spahr (TIMCAL SA), P. Novák

The high rate characteristics of TIMREX® SFG44 (TIMCAL SA) synthetic graphite as a negative electrode in an electrochemical lithium half cell were investigated by using a specially developed test protocol. The rate capability of a graphite negative electrode is not only a function of the graphite material but also the electrode engineering plays an important role, suggesting a transport limitation model. The key parameters are the loading, the thickness, and the porosity of the electrode.

1 INTRODUCTION

Lithium-ion technology has been developed on an industrial scale. There is now a strong interest in utilizing Li-ion batteries for transportation applications. In hybrid vehicles, as a power assist, the battery must be able to rapidly store and release large quantities of energy and have a good cycle life. For such applications, high rate capability electrode materials are needed to develop high-power lithium-ion batteries [1]. Thus, new materials must be designed and existing materials need to be adjusted, tested and developed to improve their high rate charge and discharge capabilities. Present lithium-ion battery systems, which use a carbon/graphite negative electrode, need to be improved for power applications. Kinetic diffusion limitations are invoked in literature [2] to explain why graphite electrodes cannot deliver high currents. We applied a new experimental strategy to demonstrate that high currents for the graphite negative electrode are possible.

It is well known that, for producing industrial battery electrodes, relatively large particles with a small surface area (BET) are advantageous. TIMREX® SFG44 synthetic graphite (ca. 4 g/m^2 BET surface area, and with 90% of particles smaller than 44 µm) was used as a model system for the measurements of the electrode discharge capability for different electrode properties (thickness, porosity, graphite loading). To separate the properties of the graphite from those of the counter electrode a metallic lithium counter electrode was used. The latter is known to deliver very high current at low overpotentials.

2 EXPERIMENTAL

Electrochemical charge/discharge measurements were carried out at 25 °C in a temperature controlled box in laboratory cells described elsewhere [3]. Metallic lithium was used as the reference and counter electrode. 1 M $LiPF_6$ in DMC/EC 1:1 (w/w) (E. Merck, Darmstadt, Germany) was used as the electrolyte solution. The graphite electrodes were prepared by blade coating of the graphite materials on to a copper foil current collector. PVDF was used as binder material.

To complete the solid electrolyte interphase (SEI) formation step during the first charge, a relatively low specific current (current density) of 10 µA/mg of graphite was chosen. After a potential of 5 mV vs. Li/Li$^+$ was reached during the galvanostatic Li$^+$ insertion, the charging was then potentiostatically continued until the specific current had dropped below 5 µA/mg. The discharge was performed with currents ranging from a rate of C/5 to higher C-rates, whereby the galvanostatic discharge capacity was terminated at a cell voltage of 1.5 V. When this final cell voltage was reached (i.e., when the galvanostatic discharge has finished), the voltage was kept constant until the specific current had dropped to 5 µA/mg of graphite. This additional step is not usual for discharging commercial lithium-ion batteries. It was performed in order to remove all the lithium ions from the graphite electrode. This ensures reproducible conditions at the end of each cycle. For the following three cycles, the C/5 rate (74.4 µA/mg) was chosen to ensure complete film formation. During subsequent cycles, we choose the same charging rate of C/5, terminated at a cell voltage of 5 mV. The discharge was performed with currents ranging from a rate of C/5 to higher C-rates, while the galvanostatic discharge capacity was terminated at a cell voltage of 1.5 V. For each current density, five consecutive cycles were performed. A detailed description was published in [4].

3 RESULTS

The irreversible capacity observed during the first reduction cycle decreases the energy density of a lithium-ion cell. TIMREX® SFG44 has a coulombic efficiency of about 93 % which is a satisfying value for high power battery applications. The cycling performance of a TIMREX® SFG44 negative electrode shown in Figure 1 indicates a capacity retention of 97 – 98 % after 150 galvanostatic cycles at 0.2C.

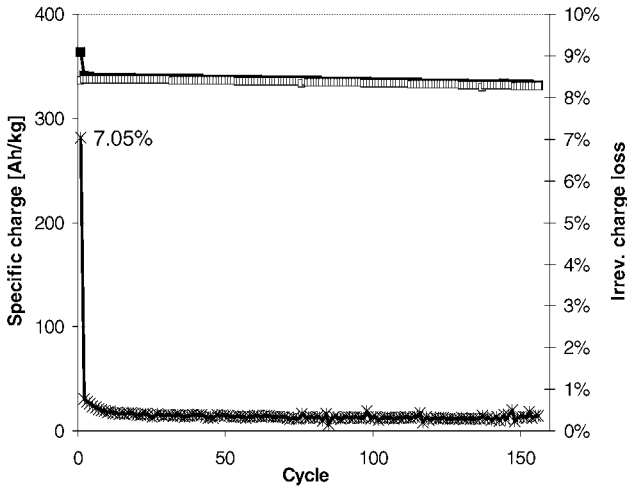

Fig. 1: Cycling performance (■■■ charge capacity, □□□ discharge capacity) and irreversible capacity loss ("charge loss", ⋆⋆⋆) of a TIMREX® SFG44 graphite electrode. Electrolyte 1 M $LiPF_6$ in EC/DMC (1:1), cycling rate ~ C/7).

For the high rate capability measurements, the amount of negative electrode mass deposited on the current collector varied from 2 mg/cm^2 up to above ca. 11 mg/cm^2. This allows the investigation of the roles of both the electrode thickness and porosity on the rate capability.

Figure 2 summarizes the results of various tested C-rates from 0.03C, 0.2C, 1C – up to 12C for a selected 54 µm thick (active material load 5.4 mg) uncompressed SFG44 electrode. The q_g value characterises the electrode properties under high current conditions and the q_t value shows a possible electrode deterioration during cycling. For low discharge rates the graphite electrodes behave very well, most of the capacity is obtained in the galvanostatic step.

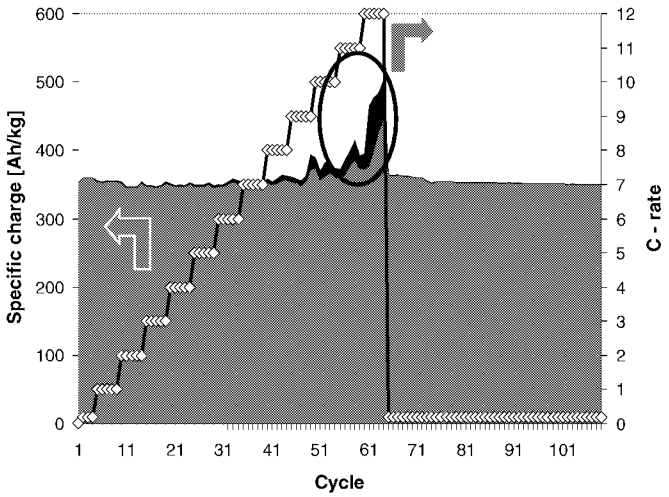

Fig. 2: C-rate (⟿), galvanostatic discharge capacity q_g (▒), and total discharge capacity q_t (▬) of a 54 µm thick TIMREX® SFG44 electrode (electrode loading ca. 3 mg/cm^2). The circle marks features which are due to dendrite formation at the counter electrode.

For the selected electrode, q_g was close to q_t at C-rates up to 8C. At higher discharge rates than 8C, q_g decreases relatively to q_t. Note that at very high discharge C-rates, the specific charge of the discharge process is apparently higher than the specific charge of the charge process. This is a result of "soft" short circuits due to dendrite formation. However, after a few stabilizing cycles at the 0.2C discharge rate, the discharge capacity is again in the normal range. Therefore it can be concluded that even after moderate dendrite formation (and short circuits) at high current densities (12C), the performance of the graphite electrode does not deteriorate (shown by stable charge/discharge cycles in Figure 2).

Figure 3 summarizes the experiments involving various electrode loadings. It shows the correlation between the maximum reached C-rate (defined as $q_g/q_t \geq 80\%$) and the electrode loading with the active graphite mass. The graphite electrodes with low loadings (1.9 – 3.6 mg/cm^2) show excellent high-current performance with good discharge capacity. More than 80 % of the specific charge of the graphite could be used within the galvanostatic discharge step in less than 5-6 min (10-12C), which is relatively high for graphite electrodes.

However, the electrodes with higher loadings (over 6 mg/cm^2) show lower but still good C-rate performances (4-6C), depending on both, the thickness and porosity of the electrode. On the other hand, the maximum current rate for fairly thick electrodes was lower. The behaviour of a cell containing 190 µm thick SFG 44 electrode with an active mass loading of 10.85 mg/cm^2 becomes poor rate capability, probably due to a decrease in the diffusion rate of the electrode. The q_g value is close to q_t at C-rates up to 2C.

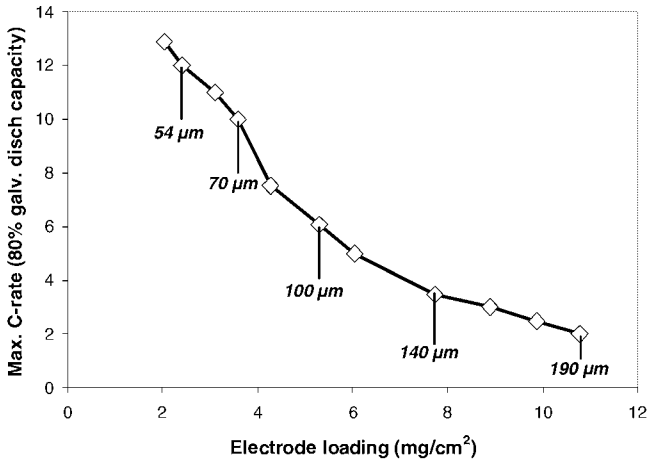

Fig. 3: Rate capability of TIMREX® SFG44 graphite electrode with different electrode loadings (at q_g/q_t>=80%).

4 CONCLUSION

We demonstrated that TIMREX® SFG44 graphite negative electrodes show high current discharge rates. For high C-rates above 2C, the control of electrode loading, electrode thickness and electrode porosity is important. Thin graphite electrodes with a small electrode loading result in a high rate capability with a retention of the cell capacity of above 80% at 12C. A 70 µm thin electrode, which can be applied in a commercial lithium-ion battery, can reach a 10C discharge rate capability.

5 REFERENCES

[1] M. Broussely, P. Biensan, and B. Simon, Electrochim. Acta **45**, 3 (1999).

[2] N. R. Avery and K. J. Black, J. Power Sources **68**, 191 (1997).

[3] F. Joho, B. Rykart, A. Blome, P. Novák, H. Wilhelm, and M. E. Spahr, J. Power Sources **97-98**, 78 (2001).

[4] H. Buqa, D. Goers, M. E. Spahr, and P. Novák, ITE Battery Letters **4**, 38 (2003).

SYNCHROTRON X-RAY ABSORPTION STUDY OF $LiFePO_4$ ELECTRODES

O. Haas, A. Deb (LBL), E.J. Cairns (LBL), W. Scheifele, A. Wokaun

$LiFePO_4$ was investigated in practical Li-ion intercalation electrodes used for Li-ion batteries applying X-ray absorption spectroscopy (XAS). The $LiFePO_4$ electrode was analysed at the initial state ($LiFePO_4$, Fe(II)) corresponding to the uncharged state of the battery, and at the Lithium free state ($FePO_4$, Fe(III)), which corresponds to the battery's charged state. The XANES region of the X-ray absorption spectra revealed a large Fe K-edge shift and pre-edge features corresponding to a high spin configuration for Fe(II) in $LiFePO_4$.

1 INTRODUCTION

$LiFePO_4$ can be used as cathode material in re-chargeable Li-ion batteries. It is chemically very stable, has a high charge density (170 Ah/kg) and should imply lower cost and environmental problems than all other cathode materials proposed for this purpose. We analyzed $LiFePO_4$ electrodes using synchrotron X-ray absorption spectroscopy (XAS). To our knowledge XAS investigations have not been used to characterize $LiFePO_4$ electrodes in electrochemical Li/$LiFePO_4$ cells.

2 EXPERIMENTAL

X-ray absorption measurements were carried out at beam line 7-3 (unfocussed) at the Stanford Synchrotron Radiation Laboratory (SSRL). The electrochemical cell was designed as an *in-situ* cell as depicted in Figure 1. The $LiFePO_4$ electrode with a charge density of 1.45 mAh/cm^2 was obtained from Hydro-Québec power research. A 1 mm thick soft glass-fiber separator soaked in with electrolyte (1M $LiPF_6$ in EC/DMC (1:1)) was used as a separator and a Li-electrode as a counter electrode.

3 RESULTS AND DISCUSSION

Figure 2 shows the voltage time curve for the charging process of the $LiFePO_4$ electrode and the Fe K-edges of the spectra measured before and after charging. It shows a strong shift of the main edge, which is due to the different valence states of the iron in the charged and uncharged state of the electrode. Figure 3 shows the two spectra in the pre-edge region where Fe 1s→3d transitions occur. The ligand field produced by the phosphate oxygen atoms, which are approximately octahedral coordinated to the iron split the 3d states in to t_{2g} and e_g states as indicated in the figure 3. The fact that $LiFePO_4$ d^6 shows both t_{2g} and e_g bands indicates a high spin configuration for Fe(II).

4 CONCLUSION

The strong edge shift and the pre-edge features of the charged and uncharged $LiFePO_4$ electrode can be used to follow the valence state and the electron configuration in the iron phosphate while the battery is cycled. Future investigation of the EXAFS region should also reveal structural changes of the nearest neighbour atoms. We think that in-situ XAS investigations is a very valuable tool to investigate the cycle life of battery materials.

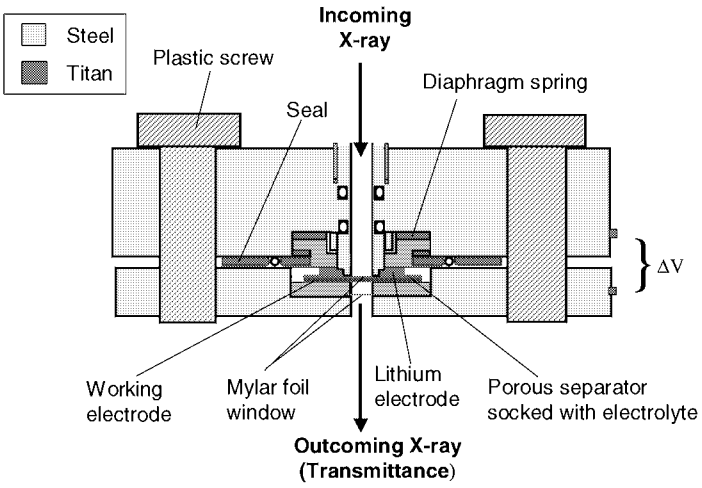

Fig. 1: Electrochemical *in-situ* XAS-Cell used to investigate $LiFePO_4$ electrodes.

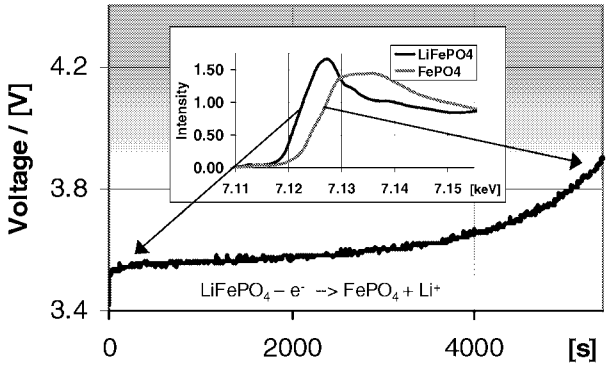

Fig. 2: Charging curve of the $LiFePO_4$ electrode using a current density of 1mA/cm^2. Insert: XANES region of the XAS spectra before and after charging.

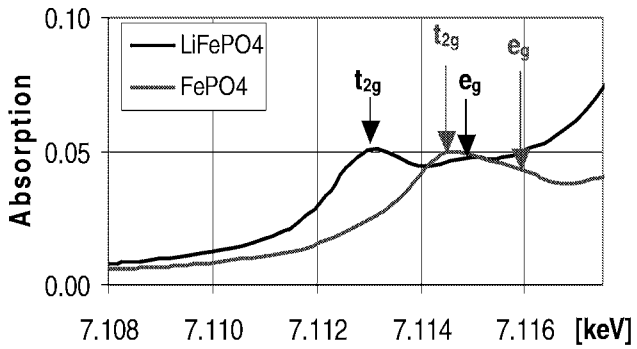

Fig. 3: Pre-edge region of the XAS spectra with indication of the t_{2g} and e_g absorption bands.

ELECTRONIC TRANSPORT PROPERTIES OF CARBON DOUBLE LAYER ELECTRODES

M. Hahn, O. Barbieri, J.-C. Sauter, B. Schnyder, R. Kötz

We have measured two electronic transport coefficients, electronic conductivity, σ, and thermoelectric power, α, of a carbon double layer electrode as a function of the electrode potential, U. The experimental results are in good agreement with the predictions of a rigid band filling model and support our hypothesis that activated carbon (AC) has to be described as a metal with hopping conduction between localised states near the Fermi level.

1 INTRODUCTION

Today's commercial double layer capacitors (DLC) are based on highly porous carbon materials, usually activated carbon (AC), as the electrode material. For these devices, charge and energy are stored in the electric field at the huge interface between the electronically conducting porous carbon and the interpenetrating electrolyte solution. The single electrode capacitance, when related to the specific BET surface area of AC, amounts to 7 $\mu F/cm^2$ near the potential of zero charge (pzc) and increases to either side [1]. On the one hand the minimum value is a factor 2 higher than that reported for the basal plane of crystalline graphite [2], on the other hand it is still lower than that of typical metals in the same electrolyte, about 20 $\mu F/cm^2$. Recently we have proposed that this intermediate behaviour can be explained in terms of a band filling description [1]. According to this model the density of electronic states (DOS) of AC is substantially higher than that of graphite but still orders of magnitude lower than that of a typical metal. The model accounts not only for the capacitance but as well for the observed potential dependence of the electronic conductance along the solid phase of the double layer [1]. Here we present additional support for the band filling model coming from the *in situ* measurement of the thermoelectric power (TEP).

2 EXPERIMENTAL

The experimental set-up is shown in Figure 1. A small sample (S) of a PTFE-bound activated carbon electrode (1050 m^2/g BET-surface area) is clamped between two metal wires (a, b). After immersion into a solution of 1 mol/l Et_4NBF_4 in acetonitrile the sample is stepwise charged by applying a voltage, U, between one of the contact wires and a large counter electrode (CE) made from the same electrode material. During the whole experiment a constant temperature drop ΔT_m (several K) is maintained across the sample by cooling of the electrolyte container (C). At each potential step, and after the capacitive charging current has dropped to almost zero, two measurements are performed.

First, the thermovoltage, u_m (up to 0.2 mV, index denotes contact metal), is measured between the upper terminals of the two wires (a, b).

Second, the electronic conductance, L, is determined by applying a small dc-current, i_{ab}, across the sample and measuring the corresponding potential drop, u_{ab} (several mV): $L = i_{ab}/u_{ab}$.

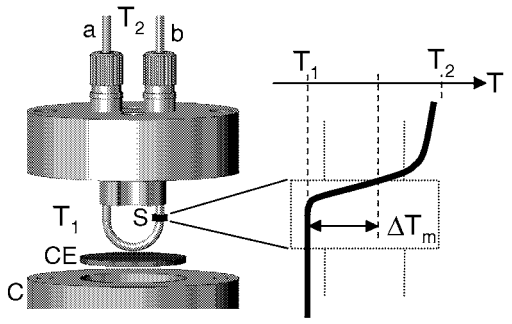

Fig. 1: Exploded view of the experimental set-up (left), and sketch of the estimated temperature profile across the sample (right). T_1 and T_2 are the temperatures in the electrolyte solution and outside the cell. ΔT_m is the actual temperature drop across the sample.

The sought TEP of the carbon, α_c (U), is related to the measured thermovoltage u_m (U) by

$$\alpha_C(U) = \frac{u_m(U)}{\Delta T_m} + \alpha_m \qquad (1),$$

where α_m is the TEP of the contact metal (taken from literature) and ΔT_m is the initially unknown temperature difference across the sample (cf. sketch in Figure 1). ΔT_m is determined from the thermovoltages of two subsequent experiments using first Au, then Pt wires. According to Equation (1) the two thermovoltages u_m (U) are given by

$$u_{Au} = (\alpha_c - \alpha_{Au})\,\Delta T_{Au} \qquad (2)$$

$$u_{Pt} = (\alpha_c - \alpha_{Pt})\,\Delta T_{Pt} \qquad (3),$$

where only u_{Au}, u_{Pt}, and α_C depend on U. (The excess charge affects only the porous sample but not the bulk metals.) Thus α_c (U) can be eliminated from equations (2) and (3) to give a linear relation between u_{Pt} (U) and u_{Au} (U):

$$u_{Pt} = \frac{\Delta T_{Pt}}{\Delta T_{Au}}\, u_{Au} + \Delta T_{Pt}(\alpha_{Au} - \alpha_{Pt}) \qquad (4)$$

From the slope and the intercept of this plot we obtain the actual temperature differences ΔT_{Pt} and ΔT_{Au}. α_c (U) is finally calculated by insertion of e.g. u_{Au} (U) and ΔT_{Au} into Equation (1).

3 RESULTS AND DISCUSSION

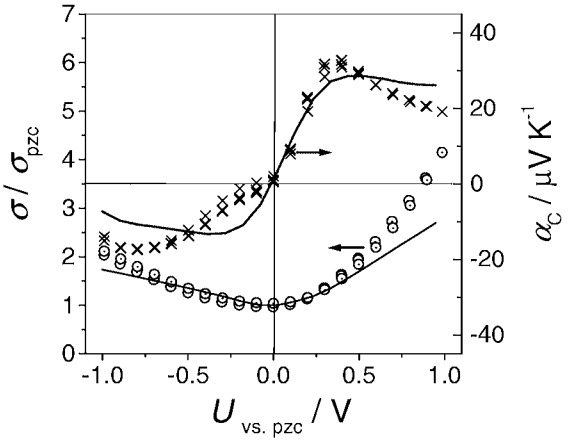

Fig. 2: Normalized conductivity, σ/σ_{pzc} = L/L_{pzc} (circles), and TEP (crosses) vs. electrode potential, U, referenced against the pzc. The lines show the corresponding curves calculated from a rigid band filling model on the basis of the capacitance derived DOS distribution shown in Figure 3.

As shown in Figure 2, the conductivity increases with |U| towards either side from the pzc. For a metal the conductivity may be related to the mobility, μ, and the DOS at the Fermi level, D (E_F), by [3]

$$\sigma = e\mu D(E_F)\,kT \qquad (5),$$

where D (E_F) kT is the thermally available conduction carrier density. Substitution of D (E_F) = 1.5 x 10^{21} cm^{-3} eV^{-1} as estimated from capacitance data for the uncharged material, and σ_{pzc} = 500 S/m gives μ = 0.8 cm^2/(Vs) [1]. This rather low mobility indicates that charge transport in AC is governed by a hopping process (thermally activated tunnelling) between localized states [3].

The TEP may be interpreted as a measure of the average energy, ⟨E⟩ – E_F, of the electronic states involved into the conduction process [3],

$$\alpha = -\frac{k}{e}\frac{\langle E\rangle - E_F}{kT} \quad \text{with k/e = 86 μV/K} \qquad (6).$$

Hence the small magnitude of α (at most 35 μV/K, corresponding to ⟨E⟩ – E_F = 10 meV) indicates that charge transport proceeds between states very close to E_F.

The results of a more quantitative numerical calculation of the two transport coefficients are also given in Figure 2 (lines). The calculation is based on simplified pore geometry (sheet like walls with uniform thickness). Charge injection is treated as filling / depletion of the capacitance derived DOS distribution as shown in Figure 3, i.e. as a shift of the Fermi level within the DOS (rigid band filling). The screening of the electric field inside the carbon walls are taken into account by numerical solution of the Poisson equation, presuming homogeneous phases with sharp boundaries. The electrons are considered to move along the pore walls, in the direction perpendicular to the electric field of the double layer. Thus, the field only affects the transport properties by changing the charge carrier density inside the pore walls. Details of the calculation will be reported elsewhere.

One should note that the model predictions shown in Figure 2 (solid lines) are calculated without using any fit parameter. Much better agreement with experimental results is e.g. obtained by introducing a potential dependent mobility.

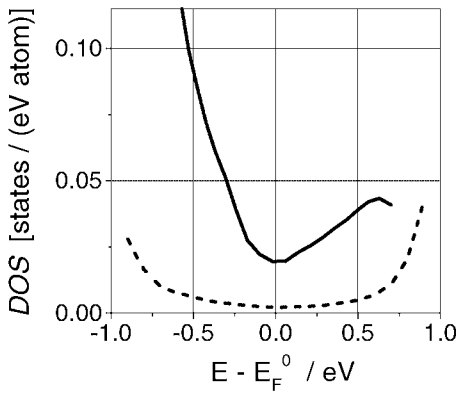

Fig. 3: Density of states (DOS) calculated for activated carbon (solid line) in comparison to literature data for graphite (broken line) [2]. Both curves are calculated from capacitance data on the basis of the band filling model. E_F – E_F^0 is the charge-induced Fermi level shift with respect to the uncharged state.

4 CONCLUSIONS

The observed potential dependence of electronic conductivity and thermoelectric power is in good agreement with the recently proposed band filling model [1]. Accordingly, activated carbon has to be treated as a metal with localized electronic states and with hopping conduction between these states. Although the DOS near E_F^0 is found to be much higher than that of graphite, it is still low compared to a typical metal, thereby limiting the electrode capacitance. As a consequence the modification of the electronic DOS has to be considered as an important issue for further optimization of DLC performance.

5 ACKNOWLEDGEMENTS

We thank the Swiss CTI (project no. 5807.2 KTS-NM, and 5945.2 TNS) and Maxwell Technologies SA, Rossens, for financial support. Maxwell Technologies SA also provided the electrode material.

6 REFERENCES

[1] M. Hahn, M. Baertschi, O. Barbieri, J-C. Sauter, R. Kötz, Electrochem. Solid St. **7**, A33 (2004).

[2] H. Gerischer, J. Phys. Chem. **89**, 4249 (1985).

[3] N.F. Mott, E.A. Davis, Electronic Processes in Non-Crystalline Materials, 2nd ed., Clarendon Press, Oxford (1979).

INFLUENCE OF THE POROUS STRUCTURE ON THE ELECTROCHEMICAL PROPERTIES OF ACTIVATED WOODS

O. Barbieri, M. Hahn, A. Herzog (EMPA Dübendorf), R. Kötz

Pyrolyzed and activated woods were prepared with different activation times. The gravimetric and volumetric capacitance C_g and C_v was measured and compared with the microporous structure of the samples. It appears that the amount of micropores is not the only relevant parameter for the optimization of the performance because at high activation level the pore wall thickness turns out to be the critical parameter.

1 INTRODUCTION

The production of new carbon materials at low cost for the commercial development of double layer capacitors is nowadays a crucial challenge. The use of activated carbons obtained from pyrolyzed woods from northern countries could be an interesting alternative.

The determination of the key morphological parameters of these carbons for the optimisation of their performance in electrochemical devices is a striking problem. Here a series of samples were prepared and analysed using cyclic voltametry (CV) and nitrogen physisorption measurements. The observed correlation between capacitance and the microporous surface are interpreted as the consequence of the limiting charge storage capacity in the thin micropore walls

2 EXPERIMENTAL

Pieces of maple wood with a 50 mm^2 cross section and a thickness of 10 mm were first pyrolysed under a nitrogen atmosphere (Carbagas, quality 99.995) in a high temperature furnace (Gero GLO) with a final temperature of 1100 °C. This temperature was achieved by a heating rate of 10 K/min with no dwelling time and a free cooling ramp. The samples were then activated with CO_2 at 900 °C with the dwelling time varying between 0 and 25 minutes.

The obtained samples were cut in slices in radial wood orientation and their capacitance was measured by cyclic voltammetry (CV) using an organic aprotic solution of 1 mol/L $(C_2H_5)_4NBF_4$ in acetonitrile. The samples were also analysed with an automatic sorption device (ASAP 2010 from Micromeritics®.) using N_2 at 77K as adsorption gas.

3 RESULTS

Figure 1 shows the nitrogen adsorption isotherms of a series of samples activated with a dwelling time of 0, 5, 10, 15, 20 and 25 minutes. These isotherms show a steep increase for small relative pressures and reach a flat plateau for the large values of p. This corresponds to the typical type I isotherms following the BDDT classification [1] which means that the carbon material contains exclusively micropores (pore size d < 2 nm) and no mesopores (2 nm < d < 50 nm). Potential macropores are not considered as they can not be observed with adsorption and do not contribute significantly to the capacitance.

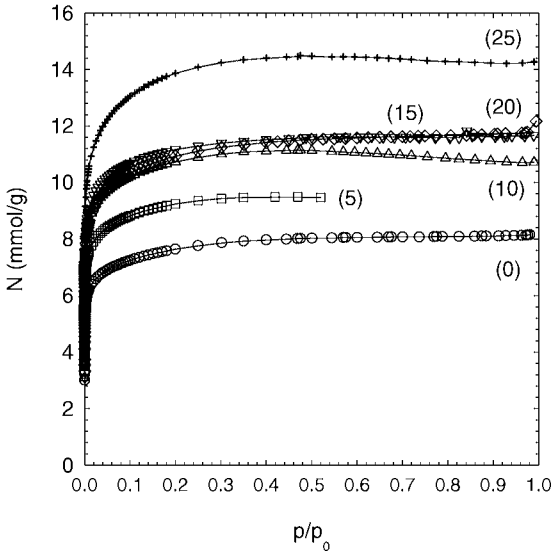

Fig. 1: Nitrogen adsorption isotherms for different activated wood samples. The parameters indicate the dwelling time at 900 °C in minutes.

Dwelling Time (mn)	*C_g (F/g)*	*C_A ($\mu F/cm^2$)*	*S_{BET} (m^2/g)*	*S_{mic} (m^2/g)*	*Δm (%)*
M0	43.1	6.71	644	642	22
M5	37.9	4.91	790	772	30
M10	53.1	6.03	913	880	37
M15	76	8.27	926	919	45
M20	72.4	7.63	950	949	54.5
M25	70.6	6.38	1168	1106	64

Table 1: C_g and C_A are the gravimetric and the specific capacitances at 0 V, respectively. S_{BET} and S_{mic} are the specific surfaces evaluated from the isotherms. Δm is the weight loss of the sample due to activation.

The specific surface of the samples and their microporous surface are evaluated from these isotherms using the BET and the t-plot model, respectively [2]. The results are shown in Table 1, where C_g is the gravimetric capacitance, i.e the capacitance determined by CV and normalised by the sample weight, and C_A the specific capacitance normalised by the microporous surface of 1 gram of sample.

The weight loss Δm of the samples is calculated by weighing the samples before and after the activation process. Actually the activation already starts at a temperature of approximately 700°C, that is before the final activation temperature of 900°C, which explains the mass loss measured for a dwelling time of zero minutes. The microporous surface of the samples, S_{mic}, increases with Δm. Because there are no mesopores all the weight loss is due to the formation of micropores.

Figure 2 shows C_g plotted versus S_{mic}. The capacitance shows first a plateau (zone 1), then a steep increase with S_{mic} until a value of 920 m^2/g is reached (zone 2). Above this value C_g is roughly constant (zone 3).

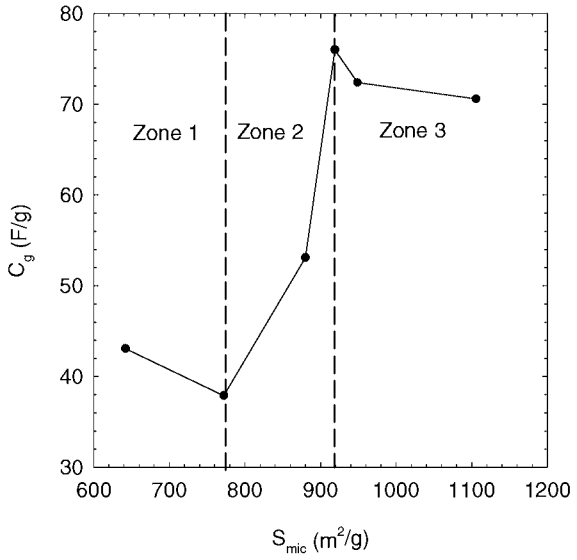

Fig. 2: Evolution of C_g with the microporous surface S_{mic}.

One should explain the first plateau (zone 1) considering that for short dwelling times some microporous surface is created but the size of the micropores created is too small for the ions in the electrolyte to enter the pore. This is also indicated by the "fish shaped" CV for M0 (see Figure 3) compared to the symmetric CV for M20 [3].

Two phenomena explain zone 2: the enlargement of already existing micropores which make the micropores more accessible to the ions in the electrolyte. Then a diminution of the sample weight as more and more matter is removed from the carbon with increasing dwelling time. These two phenomena lead to a steep increase of the gravimetric capacitance with S_{mic}.

Above 920 m^2/g C_g is almost constant because the wall thickness of the micropores formed decreases. This is a consequence of the sample's weight decrease at constant volume. Below a critical thickness of the wall, the maximum amount of charge one can store in the solid part of the double layer is limited. Because the absolute amount of charge must be the same on either side of the interface this phenomenon limits the overall capacitance. At this stage the solid part of the double layer becomes the limiting factor of the capacitance [4].

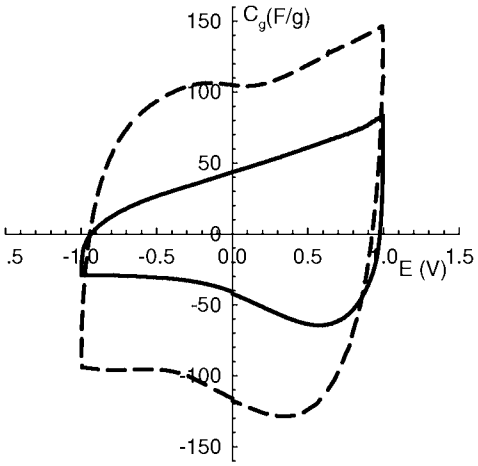

Fig. 3: Cyclic voltamogram for M0 (plain) and M20 (dashed).

4 CONCLUSION

A new kind of carbon material suitable for commercial double layer capacitors has been successfully produced. It appears that a large microporous surface is an important parameter for the enhancement of the electrochemical properties. Nethertheless the micropore morphology and especially the pore wall thickness can be a limiting parameter for the electrochemical properties. The capacitive behaviour, when the carbon part of the double layer is too thin, is limited by the electronic properties of the solid rather than by the properties of the solution side of the double layer.

5 AKNOWLEDGEMENT

Financial support of this project by the Swiss CTI (project No. 5807.2 KTS-NM and 5945.2 TNS)

6 REFERENCES

[1] S. J. Gregg, K. S. W. Sing, *Adsorption, Surface Area and porosity 2nd ed,* Academic Press, London (1982).

[2] P. A. Webb and C. Orr, *Analytical Methods in Fine Particles Technology,* Micromeritics Instrument Corporation, Norcross (1997).

[3] G. Salitra, A. Soffer, L. Eliad, Y. Cohen and D. Aurbach, J. Electrochem. Soc. **147**, 2486-2493 (2000).

[4] M. Hahn, M. Baertschi, O. Barbieri, J.-C. Sauter, R. Kötz, and R. Gallay, Electrochem. and Sol. State Lett. **7**, A33-A36 (2004).

IN SITU AFM-MEASUREMENT OF THE INTERCALATION / DE-INTERCALATION PROCESS OF Li^+-IONS IN ORGANIC ELECTROLYTE SOLUTION

F. Campana, R. Kötz, P. Novák, D. Goers, H. Siegenthaler (University of Bern)

The Solid Electrolyte Interphase (SEI) formed during the intercalation/de-intercalation process of Li^+ into Highly Oriented Pyrolytic Graphite (HOPG) was studied by in situ Atomic Force Microscopy (AFM) and cyclic voltammetry (CV). It could be shown that the SEI embraces the edge planes of the native non-intercalated step height during the intercalation process. Intercalation of Li^+ ions results in a small but detectable swelling of the HOPG.

1 INTRODUCTION

For lithium-ion secondary batteries graphitic and non-graphitic carbon materials appear to be the most adequate hosts for Li^+ at the negative electrode. However, some effects during the charge and discharge cycle are still not fully understood. During the first charge cycle a passivation film is formed by decomposition of the electrolyte, which covers the surface of the carbon. This film (SEI) protects the electrode but consumes charge. The SEI permits the passage of Li^+ ions, so that intercalation/de-intercalation of e.g. the HOPG plane can occur during the charge/discharge process. Dahn et al. [1] showed by *in situ* X-Ray diffraction a spacing change of the graphene layers of ~10.2%. We could confirm these results for the first time using AFM as an *in situ* local probe technique.

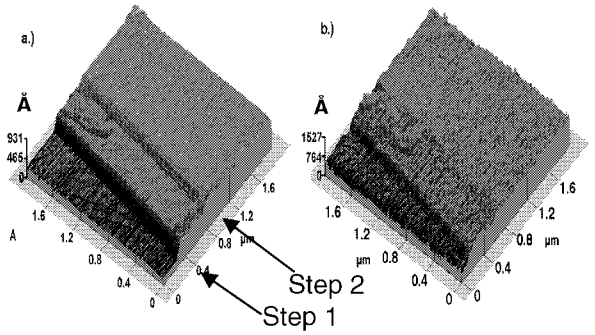

Fig. 1: *In situ* Contact-AFM pictures (1.8 x 1.8µm) of HOPG in EC: DMC (1:1) with 1M $LiClO_4$ during the first charge cycle. a.) At 2V vs. Li/Li^+ without SEI. b.) At 0.01V vs. Li/Li^+ with SEI.

2 EXPERIMENTS

The *in situ* Contact-AFM measurements were performed in ethylene carbonate (EC) and dimethyl carbonate, in a 1:1 (w/w) ratio with 1M $LiClO_4$. The working electrode was HOPG (ZYH-type). The counter and reference electrode was a lithium foil. Cyclic voltammograms were conducted in a potential window of 3V to 0.01V vs. Li/Li^+ with a scan rate of 5mV/s. After processing, the step height was measured by an average of 10 areas on different locations on two arbitrarily selected steps for 5 different images with different potentials (see Figure 2). The step heights were 98 and 51 graphene layers.

3 RESULTS AND CONCLUSIONS

The measured heights of the two steps (see Figure 1) are shown in Figure 2 before the first intercalation cycle and after subsequent intercalation and de-intercalation processes. After the first charge cycle the step height increases by 7 – 27 % depending on the step. During the subsequent discharge the step height decreases again. The observed decrease, however, is smaller than the initial increase. This would confirm that the SEI inhibits the graphene planes to return to their original position. During further cycling, swelling and shrinking can be observed with reduced amplitude of 5 – 11 %.

The rather bad statistics of the height measurements can be explained by various effects such as the voltage change during the scan and a hysteresis of the z-piezo in the AFM. Furthermore, our evaluation method assumes that the roughness profile of the SEI – which might also be affected by the probe - does not change locally on the different steps. With further measurements using the intermitted-contact mode improved results will be obtained.

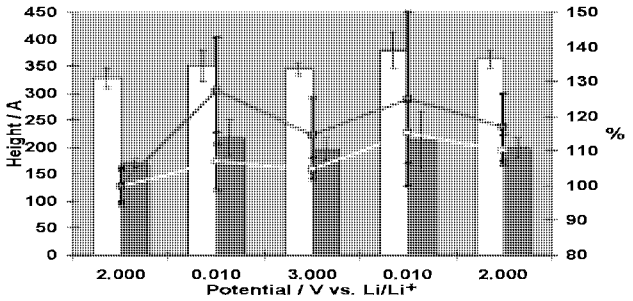

Fig. 2: Heights of Steps 1 and 2 (see Figure 1) for a sequence of electrode potentials. From left to right: before first intercalation, after first intercalation and three successive intercalation/deintercalation cycles. Bars: absolute height, lines: Percentage.

4 ACKNOWLEDGEMENT

Financial support by the Swiss National Foundation, grant no. 21-59224.99, is gratefully acknowledged.

5 REFERENCE

[1] J.R. Dahn, R. Fong, M.J. Spoon, Physical Review B **42,** 6424 (1990).

BENZOTRIAZOLE (BTA), A PROMISING CORROSION INHIBITOR FOR WC-Co HARDMETAL

B. Schnyder, C. Stössel-Sittig, R. Kötz, S. Hochstrasser-Kurz (ETH Zürich), S. Virtanen (ETHZ), Ch. Jaeggi (University of Bern), N. Eichenberger (Uni Bern), E. Szöcs (Uni Bern), H. Siegenthaler (Uni Bern), P. Ziegler (AGIE SA), I. Beltrami (AGIE SA)

Wire Electro-Discharge Machining (W-EDM) of tungsten carbide with Co-binder may lead to corrosion and discolouration at the surface. The corrosion behaviour of WC-Co based hardmetal was investigated in different aqueous solutions (acidic, neutral, and alkaline solutions). At open-circuit potential WC-Co based hardmetals show rather high dissolution rates in all types of electrolyte. An efficient corrosion inhibitor (benzotriazole, $C_6H_5N_3$) could be found for a borate buffer solution, pH = 8.4.

1 INTRODUCTION

Wire Electro-Discharge Machining (W-EDM) is a very promising approach towards micro- and nanomachining. A possible corrosion attack during W-EDM in water makes all efforts towards nanomachining difficult. The corrosion problem can be reduced or avoided by performing the erosion in oil, nevertheless erosion in water has several advantages (higher erosion rate, easier to control, no risk of burning), which justify efforts to study the W-EDM process in water.

The EDM technique is very often used to machine hardmetals. One of the most frequently used hardmetals in industry is tungsten carbide with cobalt as binder metal (WC-Co). Although WC-Co hardmetal is widely used, only few investigations exist on the corrosion behaviour of this type of hardmetal [1].

2 RESULTS

In all electrolytes studied (acidic, neutral, and alkaline solutions), the WC-Co hardmetal shows very high dissolution rates at the open-circuit potential (OCP). Additionally experiments in different solutions illustrate that the pH of the solution dominates the corrosion behaviour, while the influence of different anions as e.g., OH^-, Cl^-, SO_4^{2-}, PO_4^{3-}, ClO_4^-, is only minor.

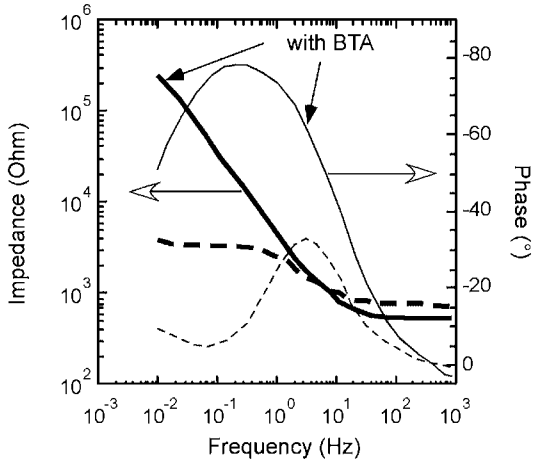

Fig. 1: Impedance spectra for WC-Co in borate buffer, pH 8.4, with and without 0.01 M BTA measured at open-circuit potential.

In order to reduce this corrosion process of WC-Co, the possibility to use inhibitors for hardmetal has been explored. BTA (benzotriazole, $C_6H_5N_3$) was found to be an efficient inhibitor for this type of hardmetal in borate buffer solution, pH = 8.4. Figure 1 shows the impedance spectrum of the hardmetal at the OCP. The impedance value at low frequencies is a measure for the corrosion rate. In the presence of a rather low BTA concentration of 0.01 M, the corrosion resistance is increased by a factor of at least 100 (see Figure 1).

In order to clarify the inhibition mechanism, samples exposed to borate buffer with and without BTA were investigated by XPS (see Table 1). Clearly a nitrogen signal could be detected on the sample exposed to BTA containing solution for one hour, indicating the presence of the nitrogen containing inhibitor on the surface. Due to the presence of this molecule on top of the surface, the signals of the other elements are reduced. This type of inhibitor seems to block at least a part of the electrode surface by adsorption and reduces the total corrosion rate of the WC-Co. More details can be found elsewhere [2].

	O [at%]	C [at%]	Carbide [at%]	W [at%]	Co [at%]	N [at%]
a	28.1	29.1	16.3	20.5	6.0	-
b	13.1	57.9	6.8	7.5	2.3	12.4

Table 1: Surface composition determined by XPS of a polished sample WC-Co exposed at OCP for one hour to a) a borate buffer solution, pH =8.4, b) a borate buffer solution with 0.05 M BTA.

3 ACKNOWLEDGEMENTS

Financial support of the TOP NANO 21 program of the Commission of Technology and Innovation (CTI) and AGIE SA, Losone (CH), are gratefully acknowledged.

4 REFERENCES

[1] M.H. Ghandehari, J. Electrochem. Soc. **127**, 2144 (1980).

[2] B. Schnyder, C. Stössel-Sittig, R. Kötz, S. Hochstrasser-Kurz, S. Virtanen, Ch. Jaeggi, N. Eichenberger, H. Siegenthaler, accepted for publication in Surface Science in (2004).

VOLTAMMETRIC INVESTIGATIONS OF THE UNDERPOTENTIAL DEPOSITION OF HYDROGEN ON POLYCRYSTALLINE PLATINUM ELECTRODES IN H_2SO_4

A. Reiner, B. Steiger, G.G. Scherer, A. Wokaun

Polycrystalline Pt electrodes with different surface characteristics were investigated by cyclic voltammetry (CV) in 0.5 M H_2SO_4. While plane electrodes showed a decrease in electrochemically active surface area during the measurements in the potential region where underpotential deposition of hydrogen (H_{upd}) occurs, different kinds of porous electrodes showed a stable electrochemically active surface.

1 INTRODUCTION

The costs of polymer electrolyte fuel cells can be lowered by reducing the amount of Pt required as catalyst while utilising the Pt more efficiently. Today, carbon supported Pt particle electrodes are mostly used. A Pt surface which features continuous Pt-Pt contacts up to the membrane enables also remote Pt particles to be electrochemically active [1]. CV and impedance spectroscopy in the H_{upd} region are used to understand the mechanism behind this effect, but these methods require stable active surfaces, where no disturbing reactions superimpose with the H_{upd} process.

2 EXPERIMENTAL

All CV measurements were carried out with a three electrode arrangement in 0.5 M H_2SO_4 (H_2O: 6 ppb TOC, H_2SO_4: 99.999 %) saturated with purified argon.

Electrode description	Label	Electrochemical active surface	Roughness factor (r.f.)
Flat Pt disc	E-1	0.00083 cm^2	1.7
Pt pellet	E-2	253 cm^2	432
Porous Pt disc	E-3	0.022 cm^2	44
Pt mesh	E-4	16.6 cm^2	2.4

Table 1: Electrode specification.

For E-1 a Pt wire was heat-sealed in a glass capillary and mechanically polished. E-2 was formed by pressing 25.7 mg of Pt powder under a weight of 1 t. E-3 was obtained from an E-1 electrode by cycling between -0.64 V and 0.8 V vs. Hg/Hg_2SO_4 reference at 100 mV/s for 21 h. E-4 is a commercial Pt mesh. Before recording the cyclic voltammograms, all electrodes were electrochemically activated until a stable CV curve was reached (several minutes).

3 RESULTS

Through underpotential deposition the hydrogen forms a monolayer on the Pt surface before the H_2 evolution starts. This allows to calculate the electrochemically active surface by the amount of charge required for forming the monolayer. This charge is represented by the area under the CV curve in the H_{upd} region corrected for the double layer capacitance. Figure 1 shows the CV curves of E-1 after different periods of time without an extended activation into the oxygen region. The area under the curves decreases with time which means that the electrochemically active surface is becoming smaller. Two different explanations for this phenomenon exist. Conway [2] presumed that traces of organic impurities contaminate the Pt surface. Hoare's [3] explanation is that the deactivation of the Pt surface occurs by removing catalytic active oxide species (which are stable in the H_{upd} region) while limiting the cycling range to the hydrogen and double layer region.

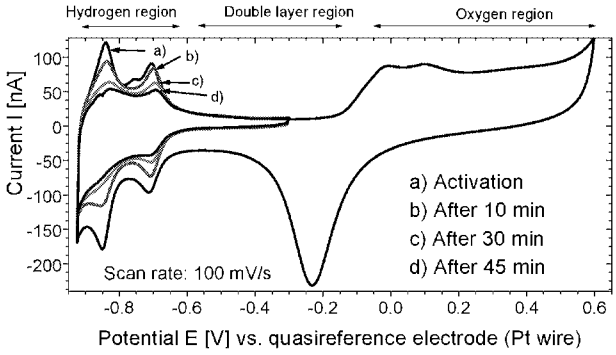

Fig. 1: Cyclic voltammograms of a flat Pt disc electrode (d=250 µm) in argon saturated 0.5 M H_2SO_4.

Contrary to the behaviour of E-1, Figure 2 shows that E-2 exhibits a stable active surface. This is due to the Pt pellet's large inner surface and its porosity.

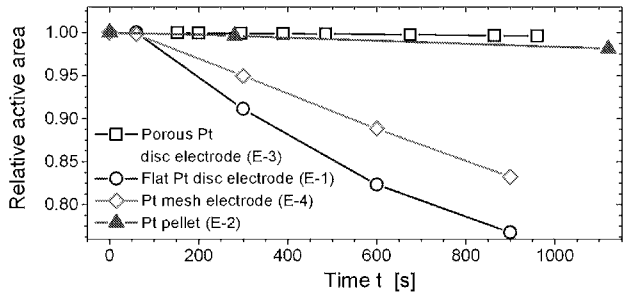

Fig. 2: Active electrode surface stability vs. time.

E-3 also showed a stable electrochemically active surface as can be seen in Figure 2. To clarify whether or not the increased surface area (compared to E-1) or the porosity is the reason for this stability, the measurement was repeated with E-4. Like E-1 the mesh electrode showed a decrease in active surface area. E-4 has a much larger surface than E-3, therefore the porosity alone is responsible for the stable properties of E-3. Using such electrodes, it should be possible to carry out experiments that require stable surface conditions in the H_{upd} region.

4 REFERENCES

[1] U.A. Paulus, Z. Veziridis, B. Schnyder, M. Kuhnke, G.G. Scherer, A. Wokaun, J. Electroanal. Chem. **541**, 77 (2003).

[2] B.E. Conway, H. Angerstein-Kozlowska, W.B.A. Sharp, E. Criddle, Anal. Chem. **45**, 1331 (1973).

[3] J.P. Hoare, Electrochim. Acta. **27**, 1751 (1982).

CHARACTERIZATION OF CO-SPUTTERED PT/C-LAYERS

F. Hajbolouri, G.G. Scherer, T. Vad (FZ Jülich), B. Schnyder, S. Abolhassani-Dadras, M. Horisberger, A. Wokaun

The electrochemical activity and the structure of co-sputtered Pt/C layers with different Pt-loading are investigated by Cyclic Voltammetry (CV), X-ray Photoelectron Spectroscopy (XPS), X-ray Absorption Spectroscopy (XAS), Anomalous Small Angle X-ray Scattering (ASAXS), and Transmission Electron Microscopy (TEM). The size of the Pt particles increased with increasing Pt-loading.

1 INTRODUCTION

Reducing the noble metal loading of the fuel cell electrodes is one of the crucial factors for making the fuel cell technology cost efficient and competitive to the traditional combustion engines. Recently, a sputtering technique has been explored with the aspiration to manufacture electrodes with low catalyst loading. In all of these studies a continuous Pt film is deposited on a substrate, gas diffusion electrode or directly on a membrane [1].

In this study, we have co-sputtered Pt/C layers with different Pt-loadings by DC-magnetron sputtering. The samples in the sequence of increasing Pt-loading are called I, II, and III. The electrochemical activity and the structure of these layers have been investigated by the techniques mentioned above. The experimental details will be explained in reference [2].

2 RESULTS

Figure 1 demonstrates the cyclic voltammograms of the Pt-film and the co-sputtered Pt/C-layers with varied Pt-loading, measured by CV in a half-cell containing 0.5 M H_2SO_4 as electrolyte. The intensity of the H-adsorption and –desorption peaks increases with increasing Pt-loading. Further, a discrepancy in the shape and position of the peaks is observed with varying Pt-loading. The position and the shape of H-peaks depend on the surface bond energies between Pt and H_{upd}, which might be different for different Pt structures. The XAS- and XPS- analysis provided evidence from the shift of the peaks and edges that the size of the Pt particles in the co-sputtered layer increases systematically when the Pt-loading is raised, Figure 2. The experimental results obtained from ASAXS-measurements indicate that the Pt-particles have a size of only a few nano-meters, confirmed by TEM, and very likely create a columnar structure in the sputtered layer. The specific active surface areas, A_s, and the surface roughnesses, A_r, could be calculated from the modelling of the ASAXS experimental data [2]. These values are shown in Table 1. As a comparison, the corresponding values obtained from CV-measurements are reported in the same table. Both the CV- and ASAXS- results show the same tendency for the three co-sputtered samples, i.e. the largest A_s is obtained for the sample II, and a systematic increase of the surface roughness with increasing Pt-loading. The catalyst utilization ε for H–adsorption and –desorption, of the co-sputtered layers was estimated from the ratio A_s^{cv} / A_s^{ASAXS}; it is more or less the same for all samples.

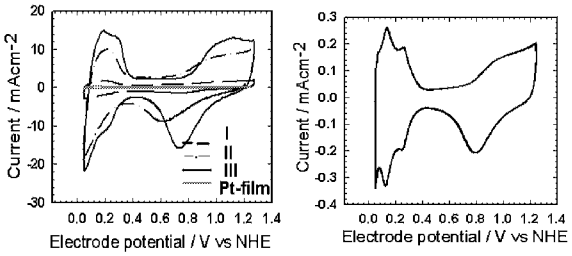

Fig. 1: Voltammograms of sputtered Pt-film (right figure) and co-sputtered Pt/C with different Pt-loadings (left figure), 0.5 M H_2SO_4, 50 mV/s. Note the different scales.

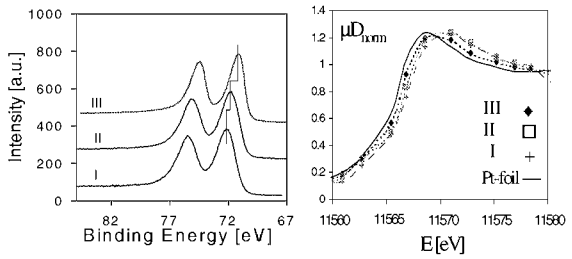

Fig. 2: XPS Pt 4f signals (left figure). Normalized X-ray absorption spectra and the reference Pt-foil (right figure).

Prepared Sample	Pt-loading mg/cm²	A_s^{cv} m²/g	A_r^{cv} cm²/cm²	A_s^{ASAXS} m²/g	A_r^{ASAXS} cm²/cm²	ε %
III	1.288	15	193	31	393	48
II	0.468	27	128	81	379	33
I	0.207	11	23	33	68	33

Table 1: Pt-loadings obtained from XAS, specific active surface, A_s, surface roughness, A_r, determined from CV and ASAXS model, and utilization factor ε for the three Pt/C samples.

3 REFERENCES

[1] S. Hirano, J. Kim, S. Srinivasan, Electrochim. Act. **42**, 1587 (1997).

[2] F. Hajbolouri, G.G. Scherer, S. Abolhassani-Dadras, B. Schnyder, T. Vad, M. Horisberger, A. Wokaun, in preparation.

METHANOL TOLERANT $Bi_2Pt_yIr_{2-y}O_7$ PYROCHLORES AS ELECTROCATALYSTS FOR THE REDUCTION OF O_2 TO H_2O

N. Lempola, B. Steiger, G.G. Scherer, A. Wokaun

The oxygen reduction reaction (ORR) and methanol tolerance of pyrochlores of the general formula $Bi_2Pt_yIr_{2-y}O_7$ have been evaluated in half-cell experiments using the thin-film rotating ring-disk electrode (RRDE) technique in acidic solution. It was found that some of these electronically conductive oxides show good ORR activity and methanol tolerance.

1 INTRODUCTION

The efficiency of the direct methanol fuel cell (DMFC) is lowered considerably as a consequence of depolarisation of the oxygen/air cathode, caused by methanol that is permeating through the polymer electrolyte membrane. Therefore, it is highly desirable to develop a methanol tolerant oxygen reduction electrocatalyst. Pyrochlores of the general formula $Bi_2Pt_yIr_{2-y}O_7$ [1] have shown both oxygen reduction activity and methanol tolerance.

2 EXPERIMENTAL

$Bi_2Pt_yIr_{2-y}O_7$ (y=0, 0.5, 0.75, 1, 1.5, 2) were prepared using the solid state synthesis method [1]. The product was characterised by powder X-ray diffraction. Pt traces in the product were removed by boiling in aqua regia. The kinetics of the ORR of the metal oxides was studied using the thin-film RRDE technique [2] in air saturated 0.5 M H_2SO_4, and methanol tolerance was measured by recording current-potential curves at 100 rpm in 0.5 M methanol in air saturated 0.5 M H_2SO_4. A suspension of catalyst mixed with Vulcan XC-72 was pipetted onto a glassy carbon disk electrode, which led an equal platinum loading of 14 $\mu g_{Pt}/cm^2$ for all examined samples. The catalyst powders were attached to the electrode surface via a thin Nafion® film. As a comparison commercially available Pt supported on Vulcan XC-72 (14 $\mu g_{Pt}/cm^2$, 20% Pt/C, E-TEK, Inc.) was used.

3 RESULTS

Current-potential curves for the ORR of $Bi_2Pt_{1.5}Ir_{0.5}O_7$ and Bi_2PtIrO_7 mixed with Vulcan XC-72 compared to Pt supported on Vulcan XC-72 are shown in Figure 1. Plateau currents and half-wave potentials are very similar to Pt/Vulcan. The higher the amount of Pt^{4+} ions in the pyrochlore the higher the ORR activity was.

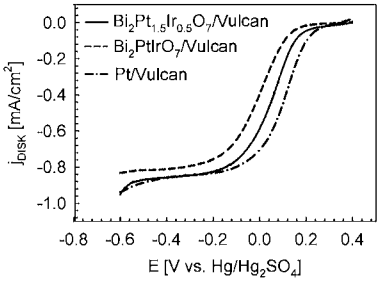

Fig. 1: Oxygen reduction on a thin-film of $Bi_2Pt_{1.5}Ir_{0.5}O_7$ and Bi_2PtIrO_7 mixed with Vulcan compared to Pt/Vulcan in air saturated 0.5 M H_2SO_4 at 1600 rpm. Negative sweeps shown at 5 mV/s.

A direct quantitative comparison of pyrochlores to the commercial Pt/Vulcan is not possible because platinum (particle size ~ 4nm) is supported on Vulcan whereas much larger particles of pyrochlores are mixed with Vulcan XC-72.

Current-potential curves for the methanol oxidation of $Bi_2Pt_{0.5}Ir_{1.5}O_7$ and Bi_2PtIrO_7 mixed with Vulcan XC-72 in comparison to Pt/Vulcan are shown in Figure 2. The peaks at the potential of 60 mV correspond to methanol oxidation activity.

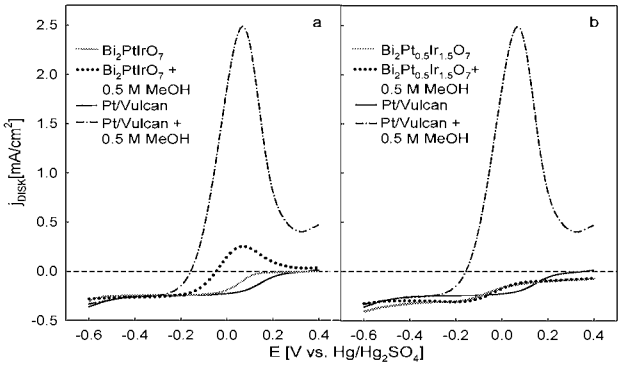

Fig. 2: Methanol oxidation activity of a) Bi_2PtIrO_7 and b) $Bi_2Pt_{0.5}Ir_{1.5}O_7$ mixed with Vulcan compared to Pt/Vulcan.

The higher the amount of Pt^{4+} ions in the pyrochlore the less methanol tolerant is the oxide, but the methanol oxidation activity is still low compared to the Pt/Vulcan XC-72.

The demonstrated oxygen reduction activity and methanol tolerance of the pyrochlores of the general formula $Bi_2Pt_yIr_{2-y}O_7$ make these oxides interesting candidates as cathode electrocatalysts in direct methanol fuel cells. The balance between high ORR activity and low methanol oxidation activity is possible by optimisation of the pyrochlore structure.

4 ACKNOWLEDGEMENTS

We are grateful to Dr. Claus Schüler for numerous helpful discussions. This work was supported by the Swiss Federal Office of Energy (BFE).

5 REFERENCES

[1] E. Beck, S. Kemmlersack, J. Less. Common-Met.**135**, 257 (1987).

[2] U. A. Paulus, T.J. Schmidt, H.A. Gasteiger, R.J. Behm, J. Electroanal. Chem. **495**, 134 (2001).

GRAFTING INVESTIGATIONS AND SCREENING DESIGN OF EXPERIMENTS FOR RADIATION GRAFTING POLY (ETHYLENE- *ALT*- TETRAFLUOROETHYLENE) AND STYRENE

S. Alkan Gürsel, H.P. Brack, G.G. Scherer

Radiation grafting of styrene monomer into poly (ethylene-alt-tetrafluoroethylene) (ETFE) in the presence of a crosslinker has been studied. Statistically-based experimental design was applied for the optimization of grafting conditions. Irradiation dose, grafting temperature and grafting time were identified to have significant effects on the degree of grafting. These three significant factors were subsequently optimized using central composite design.

1 INTRODUCTION

Radiation grafting, mainly performed by creating active sites for grafting by gamma or electron beam irradiation, is a useful method for the preparation of proton-conducting membranes. This method offers the advantages including low preparation costs, lack of need for chemical initiators, and modification of materials in already fabricated form. Numerous studies have been carried out to prepare the membranes by the radiation grafting of styrene monomer into poly (tetrafluoroethylene-*co*-hexafluoropropylene) and ETFE films [1,2,3]. In the present work, we investigated the influence of grafting parameters on the degree of grafting for the radiation grafting of styrene into ETFE films in the presence of divinylbenzene (DVB) as crosslinking agent. The Design of Experiment (DOE) methodology with three factors, central composite design (CCD), was applied to estimate the effects of factors and to optimize the response [4].

2 EXPERIMENTAL

The base polymer, ETFE, Tefzel® 100 LZ film having a thickness of 25 µm, was purchased from DuPont Circleville, OH. The grafting reactions were performed in a stainless steel reactor using an isopropanol: water mixture with 9:1 styrene:DVB under a nitrogen atmosphere. DOE, Design-Expert software (V 6.0 Trial. Stat-Ease Inc., MN, 2001) was used to perform the experimental design and analyze the results.

3 RESULTS AND DISCUSSION

This investigation considered the 3 mentioned factors labelled A, B, C. The factor levels are summarized in Table 1. CCD with two replicates of each run was used for determination of graft levels.

Factor	Name	Unit	Low level -	High level +
A	irradiation dose	kGy	1.5	3.5
B	grafting temperature	°C	50	80
C	grafting time	h	2	6

Table 1: Factors and levels for DOE.

An ANOVA approach was applied to fit a full three way interaction statistical model. After determination of the main and interaction coefficients, the following quadratic equation was obtained for the graft level in terms of coded factors:

$$\textit{Graft level} = 35.2 + 9.91A + 4.61B + 10.07C - 1.78A^2 - 5.41B^2 + 4.65C^2 + 1.23\,(A \times B) + 4.91\,(A \times C) + 0.11\,(B \times C)$$

The results of statistical analysis show that all 3 factors have a significant effect on graft level (Figure 1). The degree of grafting shows an increasing trend with the increase in the dose of irradiation. In addition, the graft level increases with increasing temperature up to 80 °C, then decreases in the case of experiment at 90 °C. The graft level was found to increase with increasing grafting time. The maximum graft level, 50.6 mol %, was reached with 3.5 kGy dose, at 80 °C for 6 hrs reaction.

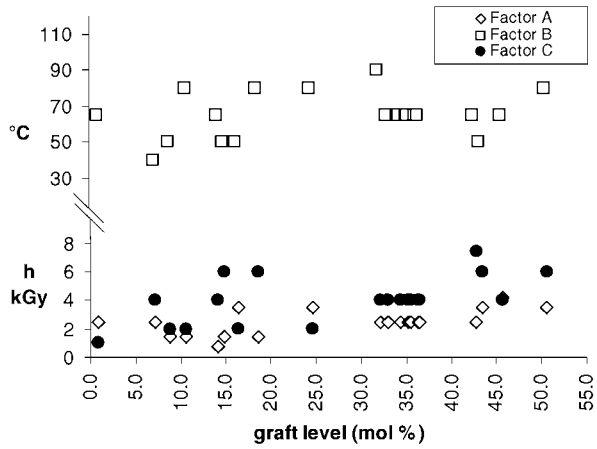

Fig. 1: Variation of graft level with 3 factors.

DOE provides more information compared to a common approach of changing only one factor at a time. With the optimized and generally applicable equation in hand, it is possible to prepare grafted films at desired graft levels.

4 REFERENCES

[1] B. Gupta, F. N. Büchi, G. G. Scherer, A. Chapiro, J. Membrane Sci. **118,** 23 (1996).

[2] F. N. Büchi, B. Gupta, O. Haas, G. G. Scherer, Electrochim. Acta **40,** 345 (1995).

[3] H. P. Brack, H. G. Bührer, L. Bonorand, G. G. Scherer, J. Mater. Chem. **10,** 1795 (2000).

[4] R. Carlson, *Design and optimization in organic synthesis*, Elsevier (1992).

RADIATION GRAFTED MEMBRANES: FUEL CELL PERFORMANCE AND INTERFACIAL ASPECTS

L. Gubler, S. Alkan Gürsel, F. Geiger, M. Arcaro, G.G. Scherer

The electrochemical heart of the polymer electrolyte fuel cell is obtained by laminating the proton exchange membrane to the electrodes under temperature and pressure. This study reports on the improvement of interfacial properties in the membrane electrode assembly, using crosslinked membranes fabricated at PSI via the radiation grafting technique.

1 INTRODUCTION

The radiation grafting process represents a low cost route to obtain membranes for the polymer electrolyte fuel cell (PEFC). The PSI membrane is a mature component, promising cell performance and materials durability have been demonstrated (e.g. [1]). One of the challenges is the optimization of the interface between membrane and electrodes. In this study, the influence of membrane impregnation with ionomer solution (Nafion®) and water content of the membrane prior to hotpressing was investigated.

2 EXPERIMENTAL

Proton exchange membranes on the basis of FEP film (25 µm thickness) were prepared using our established process [2]. The crosslinker content was 10 %. The membranes were then hotpressed with standard electrodes to obtain membrane electrode assemblies (MEAs). The MEA "FEP-hp" was hotpressed with the membrane in dry state, "FEP-hp(wet)" with the membrane in water swollen state. A second set of membranes was coated with Nafion® ionomer, and then hotpressed in dry and wet state, respectively. These MEA samples are designated "FEP-ni-hp" and "FEP-ni-hp(wet)". The MEAs were characterized in single cell fuel cells and compared against a standard MEA with Nafion® 112 membrane, which was hotpressed in the wet state.

3 RESULTS AND DISCUSSION

It is observed that both impregnating the membrane with ionomer solution and hotpressing with the membrane in water swollen state leads to higher performance (Figure 1), approaching the Nafion® 112 benchmark. The reason for higher performance is an improved interface between membrane and electrodes, as evidenced by a lower charge transfer resistance R_{CT} (Table 1), which is a measure for the quality of the interface in this case. The bulk resistance of the membrane R_{Ω} is not affected substantially by the different MEA fabricating conditions. Yet there is room for improvement, as the resistance values of the Nafion® 112 based MEA are still lower. In case of wet membrane lamination, the improved interface is believed to be caused by a "softer" membrane, because water acts as a plasticizer. The Nafion® impregnation of the membrane increases the surface energy and hydrophilicity of the membrane, resulting in a better contact of the membrane to the electrodes. A patent for an improved MEA has been applied for [3].

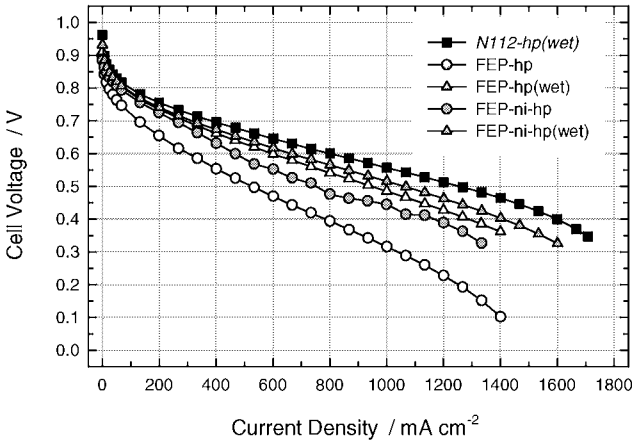

Fig. 1: Polarization curves for membrane electrode assemblies comprising radiation grafted membranes on the basis of FEP, differently pretreated and hotpressed, compared against a Nafion® 112 standard.

	R_{Ω} mΩ cm^2	R_{CT} mΩ cm^2
Nafion® 112–hp(wet)	*101*	*195*
FEP-hp	132	358
FEP-hp(wet)	132	222
FEP-ni-hp	129	297
FEP-ni-hp(wet)	124	229

Table 1: Ohmic resistance R_{Ω} and charge transfer resistance R_{CT} of the MEAs at a current density of 0.5 A cm^{-2}, determined from AC impedance spectroscopy.

4 ACKNOWLEDGEMENT

Financial support by the Swiss Federal Office of Energy is gratefully acknowledged.

5 REFERENCES

[1] J. Huslage, H.P. Brack, F. Geiger, F.N. Büchi, A. Tsukada, G.G. Scherer, PSI Scientific Report 1998, **V**, 51-52 (1999).

[2] T.J. Schmidt, K. Simbeck, M. Arcaro, T. Rager, G.G. Scherer, PSI Scientific Report 2002, **V**, 81-82 (2003).

[3] European Patent Application EP 03 021 845.7.

INVESTIGATION OF THE EFFECT OF REACTOR TYPE ON RADIATION GRAFTING REACTIONS

S. Alkan Gürsel, H.P. Brack, G.G. Scherer

Radiation-grafted films have been prepared by grafting pre-irradiated poly (ethylene-alt-tetrafluoroethylene) (ETFE) with styrene using two types of reactors. The influence of grafting parameters on degree of grafting for each reactor type was investigated by a design of experiment (DOE) approach. Experiments in glass reactors yielded higher graft levels compared to ones in a stainless steel reactor.

1 INTRODUCTION

The radiation grafting method has been used to modify the properties of polymers for over thirty years. Preparation of radiation grafted ion-exchange membranes was extensively studied previously by using different reactor types [1, 2]. However, glass and stainless steel (SS) reactors were found to yield different graft levels and film properties for the grafting reactions at the same conditions. In this work, the effect of reactor type on radiation grafting reaction of styrene and ETFE was investigated. Two level full factorial design of experiments (DOE) [3] was performed for both reactor types and the effect of grafting parameters like irradiation dose, grafting temperature, grafting time on the degree of grafting was examined.

2 EXPERIMENTAL

Reactions were carried out in glass reactors (3 cm diameter, 18 cm height, 50 mL capacity) and a SS reactor (600 mL capacity) with 14 cm × 16 cm ETFE films (Tefzel® 100 LZ, 25 µm, DuPont) using an isopropanol:water mixture with 9:1 styrene:DVB under a N_2 atmosphere. Experimental design was performed with DOE, Design-Expert software (V 6.0 Trial. Stat-Ease Inc., MN, 2001).

3 RESULTS AND DISCUSSION

Two level factorial designs were performed for both reactors in order to explore the significant factors for each reactor. The factor list including the experimental ranges is shown in Table 1.

	levels	
Factors	-	+
A, irradiation dose (kGy)	1.5	3.5
B, grafting temperature (°C)	50	80
C, grafting time (h)	2	6

Table 1: Factors and levels for full factorial design.

According to ANOVA results, factors A and C have a significant effect on the graft level for both reactor types. Graft levels increased drastically with increasing irradiation dose and grafting time; however, increasing grafting temperature caused only a slight increase in graft levels for both reactors. Table 2 shows the graft levels obtained for each reactor type at low and high levels of the factors. Glass reactors yielded higher graft levels than SS reactor at the same conditions. The highest graft level obtained with a glass reactor is 76.8 mol % at high levels of all three factors; by comparison, 50.6 mol % was obtained with SS reactor at the same conditions.

	factors			graft level (mol %)	
run	A	B	C	glass reactor	SS reactor
1	-	-	-	16.8± 0.5	8.8± 0.5
2	+	-	-	32.5± 0.7	16.3± 0.7
3	-	+	-	24.3± 0.2	10.6± 1.6
4	+	+	-	39.9± 0.6	24.5± 0.9
5	-	-	+	27.1± 0.6	14.8± 0.1
6	+	-	+	65.5± 1.0	43.4± 1.1
7	-	+	+	31.7± 0.9	18.5± 0.2
8	+	+	+	76.8± 1.8	50.6± 1.2
9	mid	mid	mid	56.2± 1.0	35.4± 0.2

Table 2: Design matrix and experimental data from full factorial design for two types of reactors.

When the all levels of factors in the DOE are considered, the conversion factor between the two reactors was found to be 1.3573 (Figure 1).

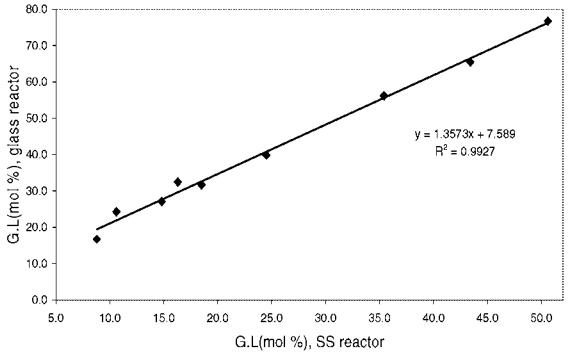

Fig. 1: Graft levels for two types of reactors.

4 REFERENCES

[1] H.P. Brack, F.N. Büchi, J. Huslage, G.G. Scherer, *Recent progress in the development of the radiation-grafted PSI membrane*, Electrochemical Society Proceedings 98-**27,** 52 (1998).

[2] F.N. Büchi, B. Gupta, O. Haas, G.G. Scherer, Electrochim. Acta **40,** 345 (1995).

[3] E.G. Watts, *Explaining power using two-level factorial designs,* J. Quality. Tech. **29,** 121 (1997).

CROSSLINKED RADIATION-GRAFTED FILMS

M. Slaski, H.P. Brack, D. Fischer (Zürcher Hochschule Winterthur), G. Peter (Zürcher Hochschule Winterthur), A. Wokaun, G.G. Scherer

Radiation-grafted membranes prepared by using styrene (S) and divinyl benzene (DVB) as graft components and subsequent sulfonation can be applied as solid polymer electrolytes in fuel cells and other electrochemical devices. The use of DVB as crosslinker has an important influence on the ex-situ properties like swelling, ionic resistivity, mechanical properties, surface energy, and oxidative stability. DVB also influences gas crossover, polarization performance, and lifetime in the fuel cell application. In spite of this importance, the actual DVB content and its extent of reaction has not been well investigated.

1 INTRODUCTION

The primary focus of this investigation is to determine ratios of para/meta species and pendent double bonds in FEP films grafted with styrene/DVB. Typically the composition of the technical grade 80% DVB is: 56% of meta-DVB, 25 % para-DVB, and the rest is ethylvinylbenzene (EVB) with 10% of meta and 9% of para isomer. When determining isomer ratios with IR or Raman spectroscopy, it is impossible to distinguish DVB from EVB species, the result is the overall amount of meta or para disubstituted benzenes (DSB). Another complexity of this system is that the difunctional monomer DVB may be incorporated in the copolymer even if only one vinyl group reacts [1].

2 EXPERIMENTAL

The preparation of these radiation grafted crosslinked membranes has been reported already [2]. Some important parameters in the preparation of these fuel cell membranes are that they were prepared from the 25 µm thick base polymer film FEP 100A (DuPont, Circleville, OH, USA), an alcoholic/water mixture as the solvent in the grafting process, and a concentration of 10 % DVB relative to S (vol/vol). In order to obtain the desired graft levels of between 16 and 24 %, reaction temperatures of either 60 or 80 °C were maintained and reaction times were varied between 3.5 to 8 hours. For the peak areas of the three bands shown in Table 1 the molar ratios of isomer meta and para were calculated according to the equations:

$$[\text{MSB}]/[\textit{meta}\text{-DSB}] = (A_{1493}/A_{1513} - 0.269)/0.443$$

$$[\text{MSB}]/[\textit{para}\text{-DSB}] = (A_{1493}/A_{1486} - 0.269)/0.443$$

MSB is mono substituted benzene (styrene). The ratio of pendant double bonds to mono substituted benzenes was calculated using the equation:

$$[=]/[\text{MSB}] = 0.0241x(A_{1630}/A_{620}) + 0.0044$$

3 RESULTS

The content of total DVB species and also residual unreacted pendent double bonds incorporated was constant for all membranes. Further, the molar ratio of double bonds ([=]) to mono substituted benzenes is around a value of 0.50±0.16, studied over a graft level of about 16 to 24 mass % [1]. This range covers our target graft level of 18 to 20 %.

Approximately 25 % of all DVB species incorporated into the membrane precursors are actually inactive in crosslinking due to their residual unreacted pendent double bond.

Functional group	Spectroscopic method	Band wave number /(cm-1)
Mono-subst. Benzene (MSB)	Infrared	1493*
	Raman	1030
	Raman	620*
Meta-subst. Benzene (meta-DSB)	Infrared	1486*
Para-subst. Benzene (para-DSB)	Infrared	1513*
Pendent double bonds(=)	Raman	1630*

Table 1: Functional groups used in the spectroscopic analysis. *Bands used for calculating molar ratios.

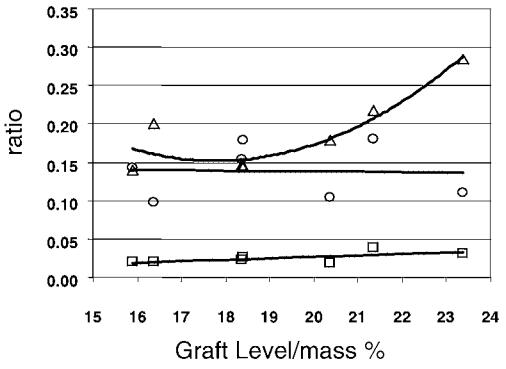

Fig. 1: Molar ratio of (□) para-DSB/MSB, (O) meta-DSB/MSB, (△) para-DSB/meta-DSB species in PSI membrane precursors.

The meta-species were found to be the more reactive species (Figure 1), causing their relatively higher total DVB species content in the membrane precursors versus their content in the grafting solution. This fact has important consequence for the surface properties of membranes [3].

4 REFERENCES

[1] H.P. Brack, D. Fischer, G. Peter, M. Slaski, G.G. Scherer, Journal of Polymer Science Part A: Polymer Chemistry **42,** 59-75 (2003).

[2] J. Huslage T. Rager. B. Schnyder. A. Tsukada, Electrochim. Acta **48**, 247-254 (2002).

[3] H.P. Brack, M. Wyler, G. Peter. G.G. Scherer, Journal of Membrane Science **214**, 1-19 (2003).

HETEROGENEOUS BEHAVIOR OF ROTATING DISK ELECTRODE SURFACES COVERED WITH CATALYST POWDER FOR THE REDUCTION OF O_2

B. Steiger, N. Lempola, G.G. Scherer, A. Wokaun

The rotating ring-disk electrode was used to examine the oxygen reduction reaction as catalyzed by Sr_3NiPtO_6. Several factors were identified that could account for the unusual ratio of ring to disk currents.

1 INTRODUCTION

The rotating ring-disk electrode (RRDE) is a powerful tool for examining mechanisms of electrode processes [1]. Attaching high-surface-area electrocatalysts powders on the disk electrode via a thin Nafion® film allows the determination of kinetic data for the oxygen reduction reaction (ORR) on Pt/Vulcan XC72 under low temperature polymer electrolyte fuel cell relevant conditions [2]. We have adapted this thin-film rotating disk electrode method to the investigation of the ORR on metal oxides mixed with Vulcan XC72 [3].

2 EXPERIMENTAL

Sr_3NiPtO_6 [4] was ground with a pestle to a fine powder in an agate mortar, a portion was sonicated in H_2O for 15 min and placed in a Beckman-Coulter LS-230 laser particle size analyzer. RRDE experiments were conducted as reported in ref. [3]. Levich currents were calculated taking the kinematic viscosity, ν, of H_2O as 0.01 $cm^2\ s^{-1}$, the diffusion coefficient, D, for O_2 as 1.93 x 10^{-5} $cm^2\ s^{-1}$ and the solubility of O_2 in 0.5 M H_2SO_4 as 1.26 mM at 25 °C. The diffusion layer thickness was calculated from $\delta = 1.61 D^{1/3} \omega^{-1/2} \nu^{1/6}$.

3 RESULTS

The slope of the least-square line (Figure 1b) of the measured (Figure 1a, lower part) (plateau current)$^{-1}$ vs. (rotation rate)$^{-1/2}$ corresponds to an apparent number of exchanged electrons of 3.1. The amount of H_2O_2 production expected on the basis of this slope is greater than observed in the RRDE experiment where less than 7 mol-% H_2O_2 was detected on the Pt ring.
It is known from experiments with partially masked rotating Pt disk electrodes containing surface patterns [5] that the degree of deviation of the limiting currents from Levich behavior depends on the active area fraction (determined by the ratio of the size of an active site to the site spacing) and the ratio of the site spacing to the diffusion layer thickness.

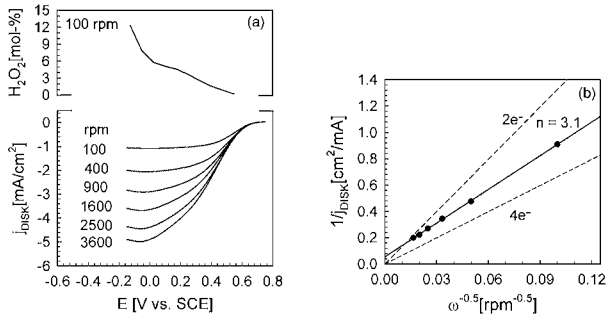

Fig. 1: (a) ORR of Sr_3NiPtO_6/Vulcan at a RRDE and fractional H_2O_2 formation. (b) Koutecky-Levich plot.

The distribution of Sr_3NiPtO_6 particles attached on the RRDE used for the measurement shown in Figure 1 was probably not homogeneous on the scale of the diffusion layer thickness (Figure 2).

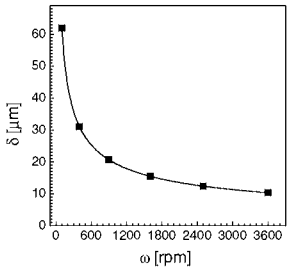

Fig. 2: Diffusion layer thickness, δ, vs. rotation rate, ω. Squares: δ for values of ω as in Figure 1.

The Sr_3NiPtO_6 particle size distribution (Figure 3) is resulting in a much more heterogeneous coating at 14 $\mu g_{Pt}\ cm^{-2}$ compared to the same amount of Pt nanoparticles supported on Vulcan. We have been able to prepare more uniform coatings but not, as yet, as homogeneous as supported Pt/Vulcan.

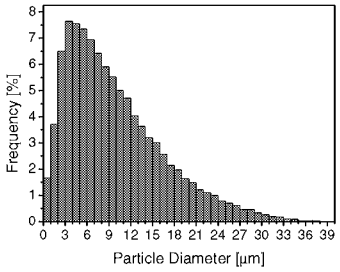

Fig. 3: Particle size distribution of Sr_3NiPtO_6 powder.

4 ACKNOWLEDGEMENTS

This work was supported by the Swiss Federal Office of Energy (BFE). We are grateful to Bastian Bommer (EMPA) for measuring particle size distributions and to Dr. Claus Schüler for numerous helpful discussions.

5 REFERENCES

[1] W.J. Albery, M.L. Hitchman, *Ring-disc electrodes*, Clarendon Press, Oxford (1971).

[2] U.A. Paulus, T.J. Schmidt, H.A. Gasteiger, R.J. Behm, J. Electroanal. Chem. **495**, 134 (2001).

[3] N. Lempola, B. Steiger, G.G. Scherer, A. Wokaun, Proc. 2nd European PEFC Forum, ISBN 3-905592-13-4, Lucerne, 407 (2003).

[4] W.H. Henley, J.B. Claridge, P.L. Smallwood, H.-C. zur Loye, J. Cryst. Growth **204**, 122 (1999).

[5] N. Juhasz, W. Deen, AIChE J. **39**, 1708 (1993).

INVESTIGATION OF GAS DIFFUSION LAYERS OF POLYMER ELECTROLYTE FUEL CELLS BY MICRO COMPUTER TOMOGRAPHY

B. Andreaus, H. Kuhn, M. Stampanoni, G.G. Scherer, A. Wokaun

Micro computer tomography (μCT) allows for obtaining 3-dimensional information of a porous structure. This data can be used to analyse and determine mass transport through the porous structure with the aid of the Lattice Boltzmann Method (LB). The results can be used to model mass transport in polymer electrolyte fuel cell (PEFC) electrodes to give a further insight into the reactant supply of the active layer and the removal of product water that results in a two phase flow within the gas diffusion layer.

1 INTRODUCTION

In polymer electrolyte fuel cells (PEFCs) electrodes, an effective mass transport of reactants to as well as of products off the reaction zone is of utmost importance to achieve high reaction rates with minimal efficiency losses. Accordingly, such electrodes include a porous gas diffusion layer (GDL) between the flow field of the (bipolar) plate and the reaction zone of the electrode's active layer to ensure a homogeneous and efficient mass transport over the whole active area of the cell. Typically, this GDL is one up to two orders of magnitude thicker than the active layer where the reactions take place. Therefore, a detailed knowledge about the structure of this porous gas diffusion layer, such as porosity and tortuosity, is a prerequisite for any successful modelling work [1] on the complicated two-phase mass transport in the electrodes [CDLabor LB method].

Here we present a method to investigate the nature of the porous GDL structure by using the micro computer tomography (μCT) facility of the SLS, at PSI.

2 EXPERIMENTAL

Two types of electrodes were investigated by means of micro computer tomography (μCT): ETEK ELAT/Std/Ds/V2 with a GDL consisting of a woven carbon fibre material and fuel cell electrodes with Torray paper as GDL. This GDL has a paper like structure of pressed carbon fibres. These two GDLs represent the most commonly used types of GDLs presently used in PEFCs. The electrodes were measured in compressed state with a defined GDL thickness in order to mimic fuel cell conditions with their specific pore structure.

The samples were irradiated by X-rays with an energy of 10 keV. As a result we obtain the 2-dimensional transmission image of the samples cross section for a certain angle of rotation of the rotation axle perpendicular to the beam. To obtain 3-dimensional information, the sample rotates by steps of 0.36° from 0° to 180°.

From these 2-dimensional cross section images, the 3-dimensional structure of the GDL was reconstructed [Stampanoni et al.].

Figure 1 shows results for ETEK and Torray GDLs. On both pictures we see a circle around the sample that is due to the plastic canopy of the sample holder, which was used for compression of the electrodes. Differences in both structures are obvious. For ETEK GDL the woven structure is observable [2]. Dark regions mark the carbon fibres whereas light-colored regions can be assigned to the pores. Torray paper GDL has much larger pore sizes (dark regions) compared to ETEK GDL. Here, light-colored needles mark the carbon fibres. The carbon fibres are distributed arbitrarily and have no preferred position. These results are helpful for image editing programs in combination with evaluation programs to perform mass transport simulations in this gas diffusion layers.

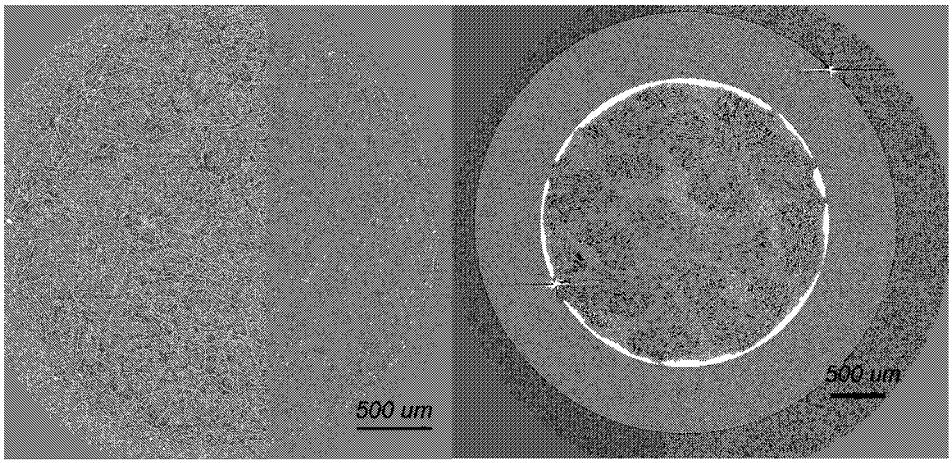

Fig. 1: μCT recordings of ETEK ELAT (right) and Torray paper (left) electrodes. Obvious are the differences in the structures of both materials.

3 REFERENCES

[1] S. Salchenegger et al., Proceeding 2nd European PEFC Forum, Luzern, 103, ISBN 3-905592-13-4.

[2] G. Rubenstein et al., Proceeding 2nd European PEFC Forum, Luzern, 449, ISBN 3-905592-13-4.

SIMULTANEOUSLY LOCALLY RESOLVED ELECTROCHEMICAL IMPEDANCE SPECTROSCOPY

H. Kuhn, B. Andreaus, I. Schneider, G.G. Scherer, A. Wokaun

Inhomogeneities in the current density respectively electrode overpotential in fuel cells with active areas of several hundred square centimetres are most often unavoidable due to locally changing reactant and water concentrations and possible temperature gradients. However, in standard electrochemical impedance measurements only average properties of the system parameters can be assessed when measuring integrally over the whole active area. We have developed a device that allows for the simultaneous measurement of the local impedance values in several segments of a fuel cell so that the local values can be determined.

1 INTRODUCTION

Electrochemical impedance spectroscopy (EIS) is a powerful *in situ* method to investigate parameters limiting the performance of a fuel cell under operating conditions. It allows for the determination of the charge transfer kinetics as well as a quantitative analysis of the double layer capacity and the ionic resistance of the electrolyte membrane [1]. However, only average properties of the characteristic process parameters can be determined in EIS measurements when measuring integrally over the whole active area. Hence, locally rate-limiting steps may remain undetected by such integral impedance measurements.

2 EXPERIMENTAL

A graphite cell with a rectangular active area of 29 cm^2 was used. The anode, with a vertical parallel flow-field, was divided into nine segments, whereas the cathode, with a meander type flow-field, was made of a single plate. Electrodes from Johnson-Matthey with a Pt/C catalyst loading of 0,6 mg/cm^2 were employed for both anode and cathode. Nafion 115 from DuPont served as electrolyte. The cell was operated at a cell temperature of 75°C. The hydrogen was humidified at a dew point of 80°C, whereas oxygen was fed dry. Hall-Sensors connected in series with each segment served as current/voltage (I/E) converters. A Zahner IM6 workstation was used to obtain the impedance spectra. The AC signals of the hall sensors were analysed to determine the local impedance spectra of the individual segments.

3 RESULTS AND DISCUSSION

In a first step, we have evaluated the local cell performance from the steady state current densities in each segment. In a second step, we have tried to evaluate the local impedance spectra from each segment as it was mentioned in the foregoing section. Figure 1 shows the local impedance spectra of selected individual segments. In order to validate the impedance responses of the segments, we have compared the individual impedance spectra with the impedance measurement of the complete cell scaled to the area of one segment, depicted as a solid line in Figure 1.

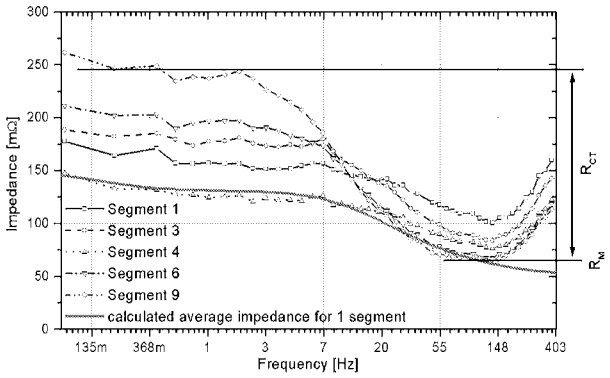

Fig. 1: Bode diagram for selected segments as well as the scaled impedance spectrum of the complete cell at 500 mA/cm^2.

Segment 1 was located at the gas inlets. In this segment we find the highest membrane resistance R_M due to the dry oxygen fed to the cell that causes drying out of the membrane. On the other hand segment 1 has the lowest charge transfer resistance R_{CT} due to the optimal reactant supply at the inlets of the gases. Segment 9 exhibits the largest R_{CT} of all segments. This can be attributed to the lower reactant partial pressure or a possible flooding of flow channels with water near the gas outlet. On the other hand, the lowest R_M is measured for this segment as the humidification by both reactant gases has reached the maximum. The best performance was measured in segment 4 that has a very low R_M and R_{CT} as well. This method gives qualitatively correct results over a large frequency range and provides further insight into locally limiting processes of a fuel cell [2]. The mismatch at frequencies above 150 Hz is due to attenuation of the signal caused by amplifiers versus the ideal signal.

4 ACKNOWLEDGEMENT

Financial support by the Swiss Federal Office of Energy (BFE) is gratefully acknowledged.

5 REFERENCES

[1] B. Andreaus, A.J. McEvoy, G.G. Scherer, Electrochim. Acta **47**, 2223 (2002).

[2] H. Kuhn et al., Proceeding 2nd European PEFC Forum, Luzern, p. 363, ISBN 3-905592-13-4.

THE DYNAMIC HYDROGEN ELECTRODE AS A REFERENCE ELECTRODE FOR DIRECT-METHANOL FUEL CELLS

D. Kramer, S. Loher (ETH Zürich), G.G. Scherer

The introduction of a reliable reference electrode in a direct-methanol fuel cell promises a better understanding of the complex current-voltage response by allowing the separate determination of ohmic, anodic and cathodic contributions to the voltage loss. A hydrogen-evolving electrode (DHE) placed beside the anode was investigated and it could be proven that this set-up provides a reliable potential.

1 INTRODUCTION

The direct-methanol fuel cell (DMFC) shows significantly lower performance than a hydrogen-fuelled polymer electrolyte fuel cell, partly due to the more complex and hence slower anodic reaction kinetics resulting in anodic potential losses of the same order of magnitude as those caused by the cathodic oxygen reduction reaction.

A way to achieve the separate determination of the electrode polarisations, and therefore simplify interpretation of polarisation curves, is the introduction of a third electrode with a stable potential. A hydrogen-evolving platinum electrode (DHE) promises to fulfil these demands even in the environment of a DMFC [1].

2 REFERENCE ELECTRODE ARRANGEMENT

In Figure 1 the used configuration of the electrodes is depicted. If the electrodes are congruent and the reference electrode is placed several membrane-thicknesses (D >> d) away from the anode the potential in the middle of the membrane will be probed, so that the voltage between anode and DHE is given by the sum of the anodic voltage drop (kinetic), half of the ohmic drop caused by the current between anode and cathode, half of the ohmic drop caused by the current between DHE and counter electrode and the voltage drop at the DHE (kinetic).

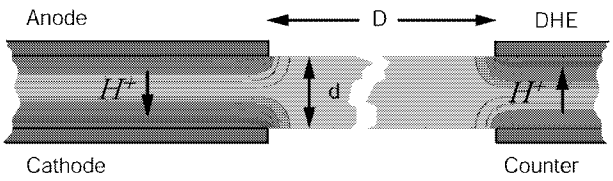

Fig. 1: Arrangement of the electrodes and idealized potential field of the electrolyte (D >> d).

3 INFLUENCE OF ANODIC AND CATHODIC SPECIES

It is well known that the presence of methanol at a platinum or platinum-alloy surface results in the coverage of the surface by a CO-like species and therefore might hinder the evolution of H_2 at the DHE as it does the oxidation of methanol. That this is not the case can be extracted from results shown in Figure 2, where two polarisation curves measured between the DHE and its hydrogen flushed counter electrode are compared. The presence of diluted methanol shows a

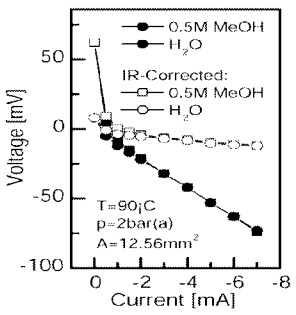

Fig. 2: Influence of methanol on DHE.

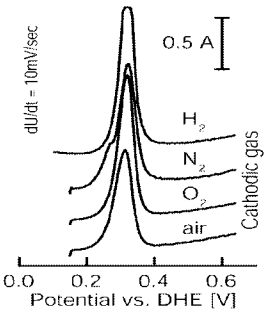

Fig. 3: Influence of cathodic species.

significant impact on the polarisation only at low currents.

To evaluate the possible impact of cathodic reactants, a stripping technique was used. The anode was poisoned with diluted methanol at a potential of 65 mV vs. DHE and after removing the non-adsorbed methanol the potential of the anode was swept up to 650mV vs. DHE. During the sweep the poisoning species can be oxidised, resulting in a characteristic current peak. The fact that different cathodic gases have no serious impact on the position of the peak is evidence that the potential of the DHE is not affected by cathodic reactants.

4 OHMIC COMPENSATION

In general, due to some misalignment of the electrodes, the potential field inside the membrane will not open symmetrically at the electrode edges. To measure this asymmetry the current-pulse method was used, where a defined current pulse introduced between anode and cathode results in a sudden voltage drop. Measurement of the voltage response, as shown in Figure 4, between anode and DHE gives information about the asymmetry and therefore makes ohmic compensation possible.

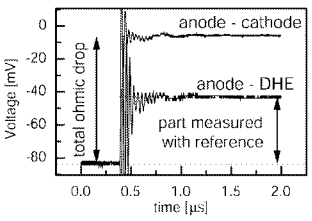

Fig. 4: Voltage response to current step.

5 REFERENCE

[1] X. Ren et al., *Water and methanol uptakes in nafion membranes and membrane effects on direct methanol cell performance.* J. Electrochem. Soc. **147,** 92-98 (2000).

ELECTROCHEMICAL IMPEDANCE SPECTROSCOPY APPLIED TO POLYMER ELECTROLYTE FUEL CELLS WITH A PSEUDO-REFERENCE ELECTRODE ARRANGEMENT

H. Kuhn, B. Andreaus, G.G. Scherer, A. Wokaun

The dimensions of the solid electrolyte in polymer electrolyte fuel cells (PEFCs) makes it difficult to introduce a reference electrode into the fuel cell in order to separate anodic and cathodic contributions. A suitable experimental setup should not disturb the current distribution in the fuel cell. In order to satisfy the boundary conditions we introduced a pseudo reference electrode into the fuel cell. With this setup we have measured the impedance of each electrode separately with respect to the pseudo reference electrode.

1 INTRODUCTION

When applying electrochemical impedance spectroscopy (EIS) to fuel cells one always measures both the anode and the cathode contributions to the whole cell impedance. Up to now, the contributions of the anode of the H_2 oxidation reaction (HOR) to the total cell impedance are mostly neglected, the measured impedance being attributed completely to the cathode and the O_2 reduction reaction (ORR) and the electrolyte. However, it was shown that the anode might contribute substantially to the cell potential loss, especially at high current densities [1,2].

2 EXPERIMENTAL

The experiments were carried out in a 28.3 cm^2 active area stainless steel cell without a flow field to keep the current distribution as homogeneous as possible. The cell was operated with H_2/O_2 at 75°C. E-TEK electrodes with a catalyst loading of 0.6 mg/cm^2 Pt/C, impregnated with 0.6 mg/cm^2 Nafion solution, were employed for both anode and cathode. Nafion 115 from DuPont served as electrolyte. The EIS measurements were carried out using a Zahner IM6 workstation (Kronach, Germany) in galvanostatic mode with an AC current amplitude of 0.2 A. The pseudo reference electrode made of an isolated (except for the tip of the fibre) carbon fibre with a diameter of 25 ⇐m was placed between two membranes, which made up the solid electrolyte.

3 RESULTS AND DISCUSSION

As described in the literature the position of the reference electrode in electrochemical cells has a big influence on the measured impedance spectra [3,4]. The optimum position would be in the centre of the electrolyte near the electrode, which is the object of investigation. This is difficult to realise in PEFC.

Due to the position of the reference electrode between the two membranes, it senses the potential in the middle of the electrolyte. The thickness of the reference electrode is about 10 % of the total electrolyte thickness, hence we assume no significant disturbing effect on the current distribution.

Figure 1 shows impedance spectra in a Nyquist representation at a current density of 500 mA/cm^2. The spectra of the half-cells differ in their characteristic behaviour due to the different reactions taking place at anode and cathode. At the anode we identify three half circles which we assign to hydrogen adsorption, proton generation and proton diffusion (dash-dotted line in Figure 1). At the cathode we recognise an inductive loop that can be attributed to an adsorption process, e.g. that of oxygen. If we sum up both half-cell measurements we match the impedance measured for the whole cell (solid and dashed line in Figure 1).

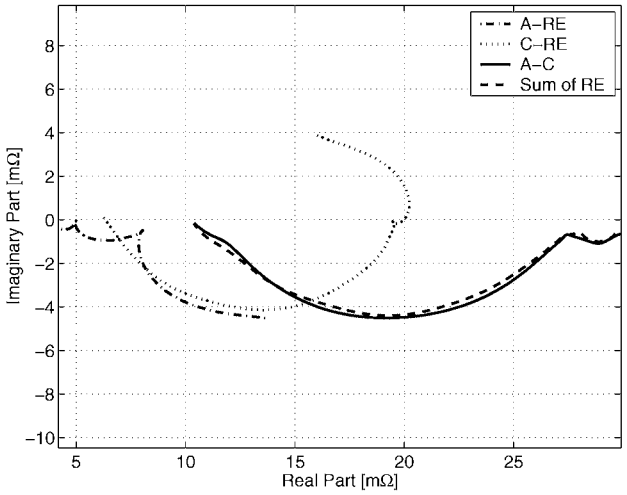

Fig. 1: Impedance measurements with respect to the pseudo reference electrode at a current density of 500 mA/cm^2.

These measurements reveal processes taking place in a fuel cell, which have not been considered up to now, because they are totally masked in the impedance measured integrally across the whole cell.

4 REFERENCES

[1] B. Andreaus, A.J. McEvoy, G.G. Scherer, Electrochim. Acta **47**, 2223 (2002).

[2] B. Andreaus, G.G. Scherer, Solid State Ionics, in press (2004).

[3] H. Kuhn et al., PSI Scientific Report 2002, **V**, 88 (2003).

[4] S.B. Adler, J. Electrochem. Soc. **149,** E166-E172 (2002).

IN SITU NEUTRON RADIOGRAPHY INVESTIGATION OF THE LIQUID WATER FORMATION IN HYDROGEN-FUELLED POLYMER ELECTROLYTE FUEL CELLS

D. Kramer, E. Lehmann, P. Vontobel, A. Wokaun, G.G. Scherer,
J. Zhang (Nissan), R. Shimoi (Nissan), K. Shinohara (Nissan)

For spatially and temporally resolved in situ detection of liquid water in a hydrogen-fuelled polymer electrolyte fuel cell 100 cm² single-cells were operated at NEUTRA and neutron radiographical measurements were performed simultaneously. By comparing serpentine and interdigitated structures as flow distributors, it is shown that interdigitating flow fields are not suited due to the tendency to accumulate liquid water and therefore block the supply of reactants to the waterclogged regions.

1 INTRODUCTION

The reaction product of a hydrogen-fuelled polymer electrolyte fuel cell (PEFC), where protons generated by the anodic reaction $H_2 \rightarrow 2H^+ + 2e^-$ are recombined with oxygen at the cathode, is water. If the product water is not removed effectively the saturation pressure in the gas flow can be reached with liquid water formation as the consequence. Since liquid water may block the flow fields and porous structures, which serve as distributors for the gaseous educts, a limitation in power density and efficiency is implicated. On the other hand, today's polymer electrolytes conduction mechanisms require a certain amount of water, resulting mostly a humidified supply of the gases and therefore an even higher tendency to form liquid water under high load conditions. Hence, the water management is of utmost importance and therefore one of the main issues to be solved on the way to commercialise fuel cells. Being a highly complex system, the application of standard electrochemical methods can only provide a limited understanding of the processes involved, since models needed to interpret the electrical behaviour are only seldom applicable under the constrains of two-phase flow conditions. Therefore, a method able to detect liquid water spatially and temporally resolved is highly desirable for gaining understanding and evaluating model predictions.

Recently, we have shown that neutron radiography is an *in situ* method capable of investigating two-phase flow phenomena in polymer electrolyte fuel cells [1, 2]. As a continuation of this work we have applied the method successfully to 100 cm² singe-cells for investigating the flooding-behaviour of different flow field types. With the application of in-house developed algorithms for data treatment the data quality could be enhanced, overcoming certain limitations given by the method itself. As a result, even very thin layers of liquid water are detectable.

2 EXPERIMENTAL

Sharing common radiographical principles with methods like X-ray radiography, information about the internal structures of a sample can be gained with neutron radiography by penetrating the object under investigation with a collimated neutron beam. The experimental setup at the facility NEUTRA is depicted in Figure 1. The neutron beam becomes attenuated while penetrating the sample, depending on the local

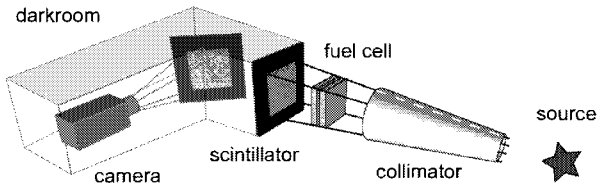

Fig. 1: Schematic drawing of the NEUTRA facility at PSI.

presence of attenuating material (e.g. liquid water). The subsequent conversion into a detectable photonic beam is realised by a scintillator, whereby the intensity of emitted light is proportional to the intensity of the incoming neutron beam. The emitted light is recorded with a charge coupled device (CCD) camera.

3 DATA TREATMENT AND QUANTIFICATION

Referenced data have to be used to extract the information about formed liquid water inside a fuel cell and to compensate for the curvature of the incoming beam intensity and the spatially varying neutron attenuation of the cell housing and flow fields. For evaluation according to the exponential attenuation law, the intensity ratio of two images obtained under different operating conditions is used. By choosing a dry cell as reference condition, the relative neutron transmission x given by the referenced data is directly correlated with the amount of liquid inside the cell. However, the exponential attenuation law holds only for infinitely thin layers of water, because of the occurrence of multiple scattering in water layers of finite thickness. Hence the correlation between water thickness and neutron transmission $\delta(x)$, as shown in Figure 2, has been

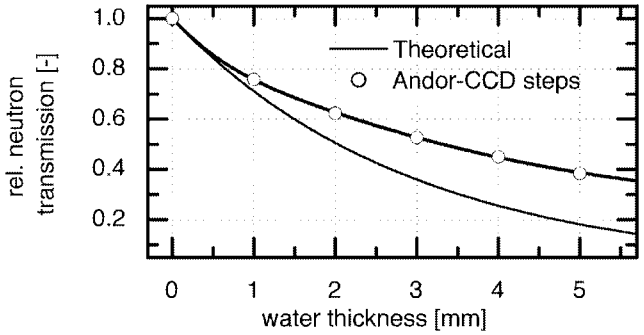

Fig. 2: Dependence of the relative neutron transmission on the water thickness.

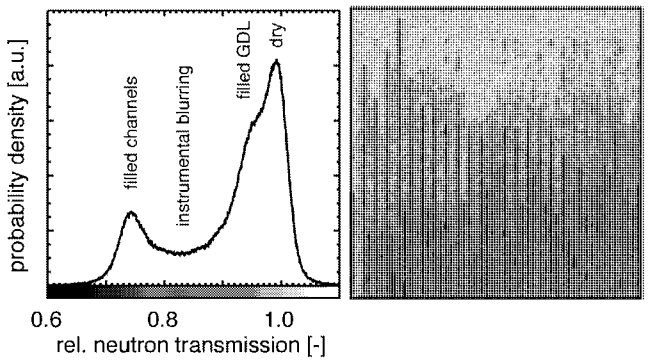

Fig. 3: Histogram and radiogram of a heavily water-clogged PEFC with interdigitated flow field.

obtained experimentally by investigating water layers of know thickness.

Since the image quality in terms of the signal to noise ratio (SNR) is limited by the shot noise, a meaningful quantification even of the thin layers of liquid present in the gas-diffusion layers ($\approx$ 200 µm) has to rely on statistical methods, like the interpretation of the relative neutron transmission probability density function $h(x)$ (histogram). A typical histogram, obtained from the investigation of a heavily water-clogged interdigitated flow field, is depicted in Figure 3. It can be seen that there are two "gaussian-shaped" peaks, corresponding to the water-filled channels (x = 0,74) and non-wetted area (x = 1,00). These peaks are connected by a plateau, to which two effects contribute: (i) water in the gas-diffusion layer (GDL) might have a distribution and therefore does not show up as a peak and (ii) the inherent unsharpness of the system causes a "sinusoidal" profile of the relative neutron transmission where a channel is water-filled and therefore feigns the presence of intermediate values. The inherent instrumental broadening is influenced by a couple of parameters, like beam divergence, scintillator thickness, and quality of the optical system.

The amount of liquid water can be calculated from the relative neutron transmission density function $h(x)$ by

$$V_l = A \cdot \int h(x) \cdot \delta(x) \cdot dx,$$

where A is the area visible in the radiogram. But it has to be kept in mind that this quantity is derived from $h(x)$ and therefore is imprecise, as long as no compensation of the effects caused by the inherent unsharpness and noise is included.

4 RESULTS

Figure 5 compares the liquid water formation and its impact on the cell performance of the interdigitated and the serpentine flow field. The interdigitated structure, which is formed by two interlocked comb-like structures, which forces the gas flow through the porous structures, is not able to remove liquid effectively, resulting in flooded channels (black spots in the radiograms). These accumulations of liquid water inside the channels could not be observed in the serpentine structure, indicating that this type of flow field is better suited for the operating conditions chosen. Nonetheless, it must be concluded that although the serpentine flow field fulfils its function to remove product water better than the interdigitated structure, a heavy flooding of the gas-diffusion layer (middle grey-levels) is not avoidable, resulting in a limited current density as well. This emphasises that an improvement of the GDL morphology is at least of the same importance for the tolerance of PEFC towards flooding, as further improvements of the flow field structures.

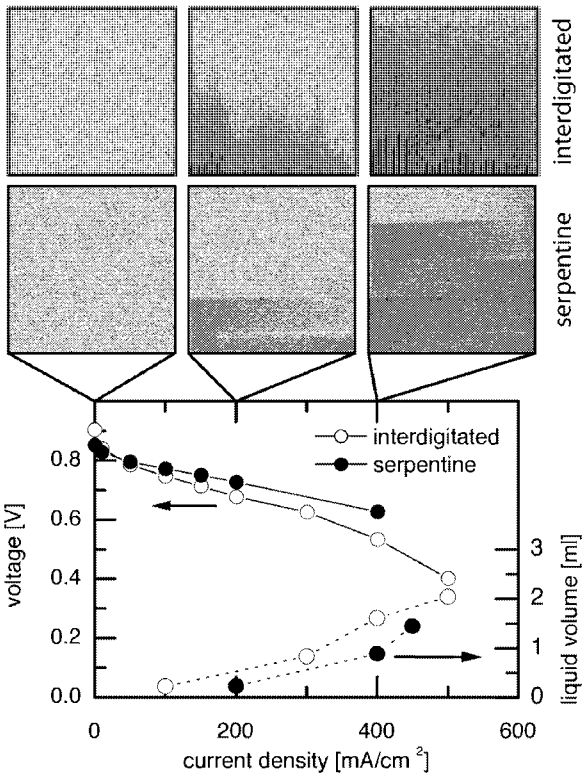

Fig. 4: Polarisation curves, liquid water volume and corresponding neutron radiograms.

5 ACKNOWLEDGEMENTS

Financial support from Nissan Motor Co., Ltd. and Swiss Federal Office of Energy is gratefully acknowledged.

6 REFERENCES

[1] A.B. Geiger, et al., *In Situ Investigation of Two-Phase Flow Patterns in Flow Fields of PEFC's Using Neutron Radiography,* Fuel Cells **2**, 92-98 (2002).

[2] D. Kramer, et al. *In situ Visualisation of Anodic Two-Phase Flow Patterns in a Direct Methanol Fuel Cell by Neutron Radiography and its Influence on the Current Distribution,* Proc. of the 2nd European PEFC Forum, Lucerne, ISBN: 3-905592-13-4, 565-574 (2003).

THE ENE INFRARED BEAMLINE "X01DC" AT THE SLS

J. Wambach, A. Wokaun, R. Abela, F. van der Veen

The ENE Infrared Beamline at the SLS will represent a state-of-the-art Infrared source with a photon energy range covering the entire Infrared (IR) range from the Far Infrared (FIR) to the Near Infrared (NIR) and partly the visible and Near UV regime. In the first stage two FTIR spectrometers will be available, which will be upgraded as soon as possible with IR microscopy and IR ellipsometry.

1 INTRODUCTION

Infrared (IR) spectroscopy is widely applied and belongs to the main analytical techniques in chemistry, physics and biology. IR spectroscopy bases on the excitation of discrete vibrational or rotational states by the absorption of radiation and is a non-destructive, easy-to-use method. Examples are the characterisation of the chemical content of material, optical studies of solids, or vibrational and rotational molecular gas phase spectroscopy. Fourier Transform Infrared (FTIR) spectrometers are used commonly and are typically equipped with conventional thermal sources.

Compared with these, the use of a synchrotron as source of the IR radiation offers several advantages. It represents a broadband source with higher brightness (by two to three orders of magnitude), with well-defined time structure. For this non-thermal source the Boltzmann noise is well reduced. Synchrotron-based IR spectroscopy has allowed important breakthroughs in two areas, namely in the extension to the lowest energy range (the Far Infrared regime) and the study of extremely small samples. IR beamlines are realised or planned at several synchrotron facilities worldwide.

2 THE SOURCE

The source for the IR beamline will be the dipole magnet "BE01S" in the first triple bend achromat of the storage ring. The design makes use of radiation produced in the up-stream fringe field of the magnet ("Edge Radiation"). The first mirror M1 is located directly down-stream of the dipole magnet in about 1 meter distance from the source point. It will reflect the extracted radiation upwards with a maximum acceptance of 84 mrad (horizontal) and 32 mrad (vertical). The reflected radiation will consist mainly of Edge Radiation and some Dipole Radiation. A movable aperture will allow limiting the acceptance to 32 mrad (H) x 32 mrad (V), i.e. mainly Edge Radiation.

3 THE BEAMLINE

The total length of the beamline will be ca. 9 m. A sketch of the optical path is given in Figure 1. The optical system will consist of two toroidal mirrors (M2 and M4) as optical elements and several flat mirrors (M1, M3, M5). Mirror M5 will be movable and direct the light to one of the two FTIR spectrometers positioned at F2 and F2'. The beamline is designed to produce a 1:1 image of the source at the entrance of the spectrometer. Further mirrors will adapt the incident IR beam to match the angular acceptance of the interfereometer. At the first focal point F1 a window will be placed to separate the synchrotron UHV from the HV in the rest of the beamline.

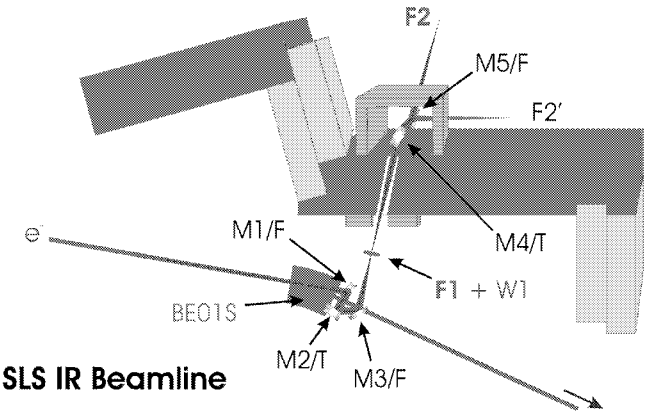

Fig. 1: Sketch of the optical design of the beamline. Flat (F) and toroidal (T) mirrors are employed.

The ENE IR Beamline will deliver photons covering the entire IR regime from the Far Infrared (FIR) to the Near Infrared (NIR) and partly the visible and Near UV regime, i.e. 1 meV – ca. 5 eV (see Figure 2).

4 THE SPECTROMETERS

Two FTIR spectrometers will be available, namely a BOMEM DA8PC.3SCV and Bruker IFS66v/S. Both spectrometers have a maximum range from < 4 cm^{-1}

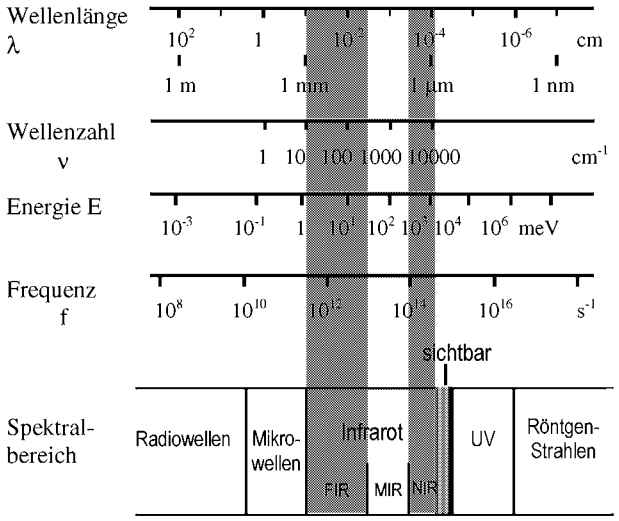

Fig. 2: The electromagnetic spectrum.

to 55000 cm^{-1} and a resolution of 0.0026 cm^{-1} (DA8), respectively 0.1 cm^{-1} (IFS66). As soon as possible the FTIR spectrometers will be upgraded, offering IR microscopy and IR ellipsometry in addition.

CHANGES IN THE ETCH RATE OF PHOTOSENSITIVE POLYMERS AS A FUNCTION OF THE PULSE NUMBER

Th. Dumont, S. Lazare (Université Bordeaux), T. Lippert, A. Wokaun

The ablation rates of a triazene polymer were studied gravimetrically by a quartz micro balance for 248 and 308 nm irradiation. Special care was taken to examine the dependence of the ablation rate at constant fluences for single pulses and the influence of consecutive pulses at the same position. A clear trend was observed in these measurements, i.e. that the mass loss after the first pulse is always different from values for the following pulses. The differences of the mass loss between the first pulse and the following pulses is most probably due to carbonization of the material, resulting in varying ablation rates for the following pulses.

1 INTRODUCTION

Studies of the laser-induced decomposition or transformation of polymers with single pulses and laser fluences close to the threshold of ablation require very sensitive techniques, such as quartz crystal microbalance (QCM) and atomic force microscopy (AFM). A mass loss (e.g. by QCM) due to photochemical reactions detected is expected for photosensitive polymers prior to changes of the surface morphology (e.g. detected by atomic force microscopy), due to the photochemical formation of N_2 by the decomposition of the triazene group. A triazene polymer (TP) was studied with QCM after irradiation with fluences below and above the threshold of ablation for irradiation wavelengths of 248 and 308 nm by observing the dependence of the frequency change and ablation rate, for single pulses as a function of the pulse number at a given position.

2 RESULTS AND DISCUSSION

The changes of the frequency after each pulse were detected at different fluences. A clear deviation of the frequency change following the first pulse is visible for TP at 248 nm irradiation. For a constant removal of mass at a constant laser fluence a constant frequency change for every laser pulse is expected. This is obviously not the case, as shown in Figure 1, where the curves reveal a clear trend of the frequency change towards lower values. This is especially the case for higher fluences which cannot be explained by fluctuations of the laser energy.

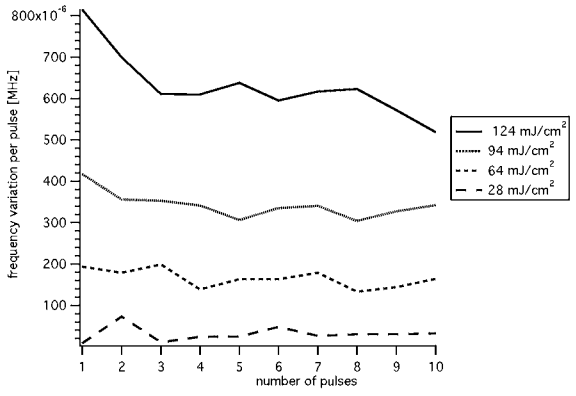

Fig. 1: Frequency change between pulses at different fluences for TP at an irradiation wavelength of 248 nm. One sample was used for each measurement at given fluence.

It can therefore be concluded that the ablation rates are clearly changing after the first pulse at high fluences. This means that less material is removed at the same fluence for pulse numbers > 1 (> 2 for 124 mJ·cm^{-2}).

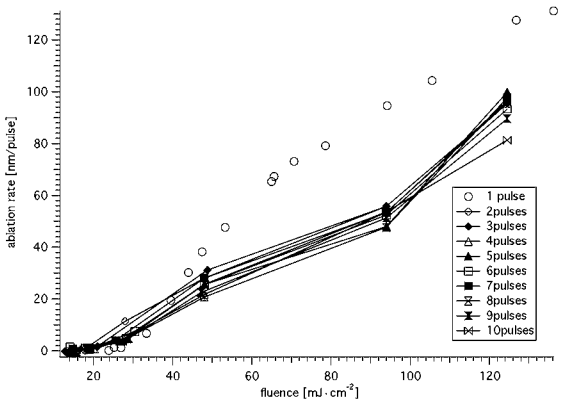

Fig. 2: Ablation behaviour of TP polymer for 248 nm irradiation. Dependence of the pulse ablation rate on the pulse number.

The corresponding ablation rates of TP for various fluences and an irradiation wavelength of 248 nm, derived from the QCM measurements, are shown in Figure 2. The curves show a significant difference of the ablation rate for the first pulse and the following pulses, indicating that the ablation rate of the polymer at this wavelength will vary depending on the number of pulses applied at a given position.

3 CONCLUSION

These results show clearly that data obtained for the ablation rate of a polymer using just one sample for irradiation with various fluences and therefore a large number of pulses, are very probably the superposition of the ablation of the material, carbon, and carbonized material. The experiments for TP at 308 nm did not show such a strong deviation for the following pulses, which is probably due to the fact that carbonization is not very pronounced at this irradiation wavelength.

4 ACKNOWLEDGEMENTS

Support of the Marie Curie Fellowship as well as the help of the laboratory members of the Laboratoire de Physico-Chimie Moléculaire, Université Bordeaux1 is gratefully acknowledged.

ANISOTROPIC REACTIVE ION ETCHING OF CHANNEL STRUCTURES IN GLASSY CARBON FOR MICRO FUEL CELLS

M. Kuhnke, T. Lippert, G.G. Scherer, A. Wokaun

Reactive ion etching of glassy carbon (GC) can be performed with etch rates higher than 40 µm/h, but reasonable aspect ratios can only be achieved at low pressure etching conditions that yield etch rates in the range of 20 µm/h. Another important parameter is the adhesion of the mask, which can be improved by polishing the GC with a diamond suspension prior to metal deposition.

1 INTRODUCTION

Structuring of glassy carbon (GC) by various methods is studied at the PSI for several years. One possible application for micro structured GC are electrodes for micro fuel cells. Typical sizes of these structures are a depth of ≈ 200 µm and a width of ≈ 50 µm. A large surface area is desirable and can only be reached with high aspect ratio channels.

We develop a process that combines the structuring of a metal mask by laser ablation with a subsequent reactive ion etching (RIE) step. Anisotropic etching is required for the fabrication of high aspect ratio structures and can be reached by optimization of the process parameters. A crucial aspect of this process is the adhesion of the metal layer, which can be improved by various pre-treatment procedures.

2 SURFACE PRE-TREATMENT

Several methods have been tested to improve the adhesion of the aluminium mask: ultrasonic cleaning in organic solvents, plasma etching in oxygen, argon or nitrogen, and mechanical polishing.

The best results were achieved by polishing the GC sample (G-type) with a 6 µm diamond suspension. This step roughens the factory-polished surface and reduces the number of surface craters which remain from the production process.

All RIE pre-treatments require an additional ultrasonic cleaning step in DI water, as residues sputtered from the RF electrode (glass cover) are deposited on the sample surface, which drastically reduces the adhesion. After this cleaning step, the O_2-etched surface yields better adhesion than the N_2-etched surface, which is in contrast to [1]. Ultrasonic cleaning alone does not increase the adhesion sufficiently.

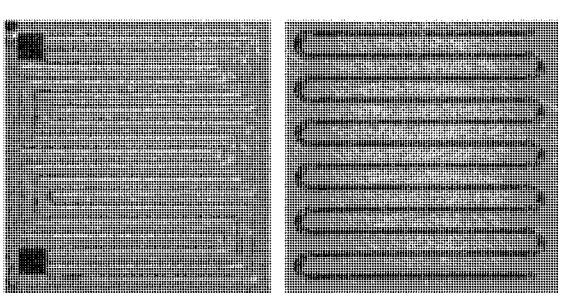

Fig. 1: (a) Meander pattern of 3 parallel lines with a distance of 84 µm (between single lines); (b) Meander pattern with round loops, written in 400 nm thick aluminium layer with 320 µm/s, line distance: 100 µm.

3 MASK WRITING

A new control software for the laser ablation setup was developed that allows high-speed writing of the aluminium mask. The speed was increased by a factor of ≈ 50 compared to the previous software to ~1 mm/s. The desired pattern can be drawn in CAD software and exported as HPGL plotter code. This code can be interpreted by the new software and allows circular and diagonal moves of the xyz stage, suitable for writing various flow field layouts (Figure 1). Lines with a minimum width of <30 µm can now also be prepared.

4 ANISOTROPIC REACTIVE ION ETCHING

Optimized process conditions (60 mTorr, 200 W RF power, low O_2 partial pressure) result in anisotropic etching of GC (Figure 2a), while higher O_2 partial pressure seems to result in more isotropic etching. When the pattern has a narrow line distance of 60 µm, this "under etching" limits the achievable depth to ~70 µm (Figure 2b).

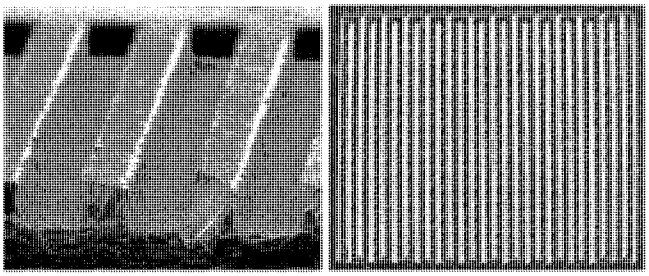

Fig. 2: (a) Reactive ion-etched channels in GC (depth: ~50 µm, width: ~55 µm, spacing: ~45 µm); (b) Meander channels with the smallest achievable line distance (60 µm) in GC, size: 1,64 x 1,64 mm^2.

Tests with a metal cover on the RF electrode result in enhanced "grass" formation in the etched channels and in a reduction of the average etch rate after 3 h by a factor of ~2.5. The deposition of glass or metal from the electrode cover on the sample has been verified by XPS measurements.

5 CONCLUSION

Mechanical polishing results in the best adhesion of the aluminium masks on GC. The ablation process of metal masks is much more flexible and faster with the new software. A lower partial pressure of O_2 seems to improve the anisotropy of the reactive ion etching process in GC.

6 REFERENCE

[1] C. Eisenmenger-Sittner, private communication.

FABRICATION OF BEAM HOMOGENIZERS IN QUARTZ BY LASER MICROMACHINING

G. Kopitkovas, T. Lippert, C. David, J. Gobrecht, A. Wokaun

A one step micromachining process, which utilizes laser assisted chemical wet etching and projection of a diffractive gray tone phase masks is applied to fabricate 3 - dimensional microstructures (such as plano-convex or Fresnel micro-lenses) in UV transparent materials. Arrays of micro-lenses in quartz are tested as a beam homogenizers for quadrupled Nd:YAG laser.

1 INTRODUCTION

Homogenization of the laser beam intensity is usually achieved by using an array of optical elements, e.g. micro-lenses in combination with a collecting (field) lens. Beam homogenizing is based on the idea of splitting the collimated beam into many beamlets, which are superimposed in the focal plane of the field lens. Each micro-lens acts as a divergent optical element, which homogeneously distributes the inhomogenities of the laser beam intensity over the complete irradiated area. An alternative technique to the multi-step photolithography process for the precise structuring of UV transparent dielectrics was developed by H. Niino at al. [1]. The key element of this method is a highly absorbing organic liquid, which is in contact with the UV transparent material. The non-radiative relaxation mechanisms of the excited organic molecules generate a temperature jump at the quartz-liquid interface resulting in softening#melting #vaporising of a UV transparent material. This method is also known as *"Laser Induced Backside Wet Etching" (LIBWE)* [1]. The rapid temperature jump at the quartz-liquid interface results in several different effects, such as chemical decomposition of the organic solution, generation of a high pressure jump, or creation of a plasma in the solution. All of those effects play an important role in the removal of the softened material from the surface.

2 EXPERIMENTAL

Fabrication of complex patterns with continuous profiles, e.g. plano-convex microlenses in quartz is achieved by the combination of LIBWE and projection of a "*Diffractive Gray Tone Phase Mask (DGTPM)*" [3]. These DGTPM's modulate the incoming beam intensity, which is projected on the quartz surface by a lens, as described elsewhere [2]. The DGTPM's are fabricated in quartz by using e-beam lithography and reactive ion etching. A XeCl excimer laser (25 ns, 308 nm) is applied as irradiation source. The wet etching solution is pyrene in acetone at a concentration of 0.4 mol/l.

3 RESULTS AND DISCUSSION

The etch rates of quartz (shown in Figure 1) using a 0.4 M pyrene in acetone solution increases slowly at low fluences, while at higher fluences the slope of the etch curve is much steeper. Studies of the etch rates and confocal Raman microscopy measurements of the etched areas in quartz ca be used to suggest the following LIBWE mechanisms. The etching of the quartz is governed by the chemical decomposition of organic solution at low laser fluences, while at the higher laser fluences the molten quartz may be removed mechanically by the pressure jump (cavitation effect). The role of the formation of the plasma in solution is not clear at the moment.

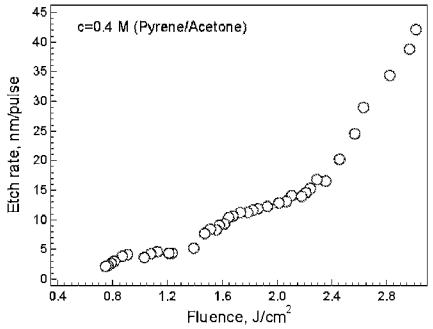

Fig. 1: Etch rates versus laser fluence of quartz.

Arrays of plano-convex micro-lenses are fabricated in quartz and tested as beam homogenizer for high power Nd:YAG laser. Each micro-lens in the array has a diameter of 250 µm and a focal length of 19 mm. A clear improvement of the Nd:YAG energy profile (shown in Figure 2) is obtained by using the micro-lens array.

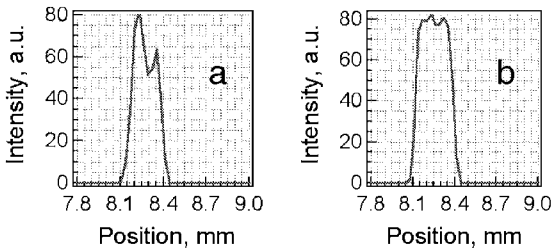

Fig. 2: The beam profile of a quadrupled Nd:YAG laser close to the focal plane of the field lens: (a) without beam homogenizer, (b) with a micro-lens array.

4 REFERENCES

[1] J. Wang, H. Niino, A. Yabe, Appl. Phys. A **68**, 111-113 (1999).

[2] G. Kopitkovas, T. Lippert, C. David, A. Wokaun, J. Gobrecht, Microelectron. Eng. **67-68**, 428-444 (2003).

[3] C. David, T. Lippert, J. Wei, A. Wokaun, Microelectron. Eng. **57-58**, 453-460 (2001).

MICROSTRUCTURES AND FILM PROPERTIES OF $La_{0.7}Ca_{0.3}CoO_3$

M.J. Montenegro, M. Döbeli, T. Lippert, S. Müller (Euresearch), A. Weidenkaff (University of Augsburg), P.R. Willmott, A. Wokaun

The quality and microstructure of $La_{0.7}Ca_{0.3}CoO_3$ (LCCO) films produced by pulsed reactive crossed-beam laser ablation (PRCLA) are analyzed considering the composition (RBS), crystallographic orientation (XRD), and morphology (AFM). The influences of cooling conditions, deposition with an oxygen background, and of an additional N_2O gas pulse are studied. The analysis indicates that the best film quality is obtained for films deposited in the presence of the gas pulse and the oxygen background, followed by a fast cooling. The presence of the different oxidizing sources influences the crystallographic orientation of the resulting films.

1 INTRODUCTION

Perovskite type oxides (ABO_3) are promising candidates as catalysts for solid oxide fuel cells and metal-air batteries. The application of $La_{1-x}Ca_xCoO_3$ as a bifunctional catalyst, i.e. catalyst for oxygen reduction and evolution for metal/air batteries, was advanced for rechargeable zinc/air batteries by Müller et al. [1]. To study and compare the catalytic activity of different perovskite phases, it is necessary to prepare electrodes on inactive substrates with well-defined electrolyte/oxide interfaces to exclude the influence of the binder, or the support material (e.g. carbon). This can be achieved by PRCLA where dense crystalline films of LCCO are obtained on MgO [2].

2 RESULTS AND DISCUSSION

The interaction of the gas pulse with the ablation plume results in an emission that is much brighter and extends further from the target compared to that obtained with an $8x10^{-4}$ mbar background of O_2. The stoichiometry (by RBS) changes with the different deposition conditions. When the films are grown only in the presence of $8x10^{-4}$ mbar of oxygen background, a lower amount of La, Ca and O_2 is observed, while an oxygen stoichiometry closest to the ideal value of 3 is obtained when the film is deposited using the gas pulse and the oxygen background. The presence of only one oxidizing source always produces films with a lower amount of oxygen. In all cases only the formation of a crystalline LCCO phase is observed, but the orientation depends on the oxidizing source. An intense LCCO(200) peak and a weak LCCO(110) reflex are observed for those films which were deposited using the gas pulse and the oxygen background. For films deposited only with the oxygen background, nearly equal intensity reflexes for the (200) and (110) orientation are observed, whereas the films deposited only with the gas pulse reveal nearly an exclusive orientation in the (110) plane. These data strongly suggest that the phase structure and preferential orientation, i.e. from (200) to (110), depends on the applied oxidizing source. The morphologies of the films grown under the different conditions are shown in Figure 1. The film deposited with the oxygen background (Figure 1A) presents a combination between large (25 nm) and small columns (5.7 nm). The roughness (rms) obtained from the AFM images (1.6x1.6 µm) is ≈7 nm. The 2D figure reveals a quite dense structure with almost no holes. The AFM image of the film deposited with the N_2O gas pulse (Figure 1B) presents a very dense microstructure, with smaller grains than for the films grown with the O_2 background. An average grain size of ≈17 nm and a roughness of ≈ 6 nm are observed. Figure 1C shows the AFM for films deposited using both oxidizing sources. The 2D picture of the film appears similar to the films shown in Figure 2A, but with different grain size and a lower density of grains. The average lateral extension of the grains is ≈40 nm with a roughness of ≈11 nm.

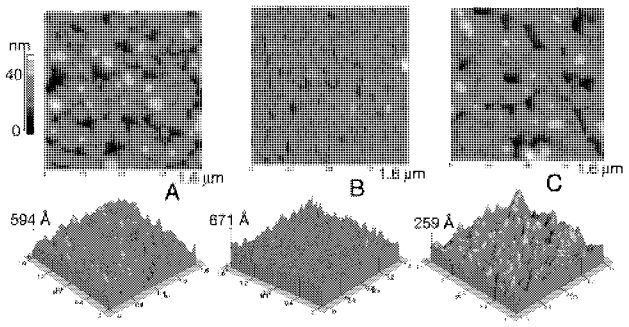

Fig. 1: AFM images of the LCCO films: A) deposited in an oxygen background $8x10^{-4}$ mbar. B) deposited without oxygen background using the N_2O pulse at 2 bar. C) deposited with oxygen background and gas pulse.

3 CONCLUSION

The stoichiometry, crystallographic quality and orientation, and the morphology of LCCO films can be controlled by varying the oxidizing source and the cooling procedure after a complete film deposition. The best film quality is obtained when the films are grown with the N_2O pulse and the O_2 background followed by a fast cooling procedure at atmospheric pressure.

4 REFERENCES

[1] S. Müller, O. Haas, C. Schlatter, C. Comninellis, J. Appl. Electrochem. **28,** 305 (1998).

[2] M.J. Montenegro, T. Lippert, S. Müller, A. Weidenkaff, P. R. Willmott, A. Wokaun, Appl. Surf. Sci. **197-198**, 505 (2002).

NS-SURFACE INTERFEROMETRY MEASUREMENT ON COMMERCIAL POLYMERS

M. Hauer, T. Lippert, A. Wokaun

The effect of the ablation mechanism on surface morphology changes during the ablation process was studied by comparing a polyimide and poly (methyl methacrylate) (PMMA) polymer with nanosecond surface interferometry. For polyimide, a photothermal ablation mechanism is usually used to describe the ablation process at irradiation wavelength ≥ 248 nm. However, the interferometric measurements at 248 nm do not show any indications for a thermal ablation mechanism. A transient surface swelling was only detected for PMMA at an irradiation wavelength of 248 nm and fluences below the threshold of permanent surface modification.

1 INTRODUCTION

Laser ablation is a promising tool to create microstructures in polymers. Until now laser ablation is, due to several drawbacks (i.e. high ablation thresholds, low ablation rates, redeposition of debris), only used in a limited number of industrial applications. It has been repeatedly emphasized that a better monitoring of the temporal evolution of the ablation process is important to understand the physical and chemical processes that characterize ablation.

In this study ns-surface interferometry is applied to observe the morphology changes of the polymer surface during the ablation process. Two different polymers, a polyimide and poly (methyl methacrylate) were studied during / after 248 nm laser irradiation.

2 EXPERIMENTAL

The polyimide was spin coated from a precursor solution and baked for 1 h at 250 °C. The PMMA was dissolved in chlorobenzene, spin coated and dried in a vacuum oven for 12 h (60 °C, 100 mbar).

The material was irradiated with a 248 nm excimer laser and the surface profile was measured with a Michelson interferometer through the substrate from the backside of the polymer. The temporal resolution was achieved by timing the excimer laser and the laser for the interferometric measurements with a delay generator.

3 RESULTS

The surface morphology changes of the polyimide after 248 nm irradiation are shown in Figure 1.The positive phase shift is proportional to the surface removal. The change of the phase shift of the polyimide and therefore of the surface morphology is observed only during the laser pulse. No negative phase shift, which would correspond to a surface expansion, is observed. This is an indication that a photochemical process is active in the laser ablation process of polyimide at 248 nm.

By contrast, the surface interferometry of PMMA shows (in the applied fluence range, below the threshold of permanent surface modification) only a negative phase shift which corresponds to a surface expansion. Measurements several seconds after the laser pulse do not reveal a permanent surface modification.

The expansion of the polymer surface is either due to the decomposition of the polymer and the subsequent diffusion of gaseous products, or due to thermal expansion of the polymer.

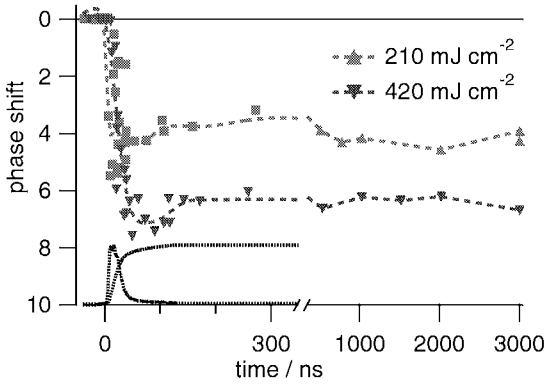

Fig. 1: Changes of the surface morphology during of the polyimide during/after 248 nm irradiation. The laser intensity and the deposited laser energy are also included in the graph.

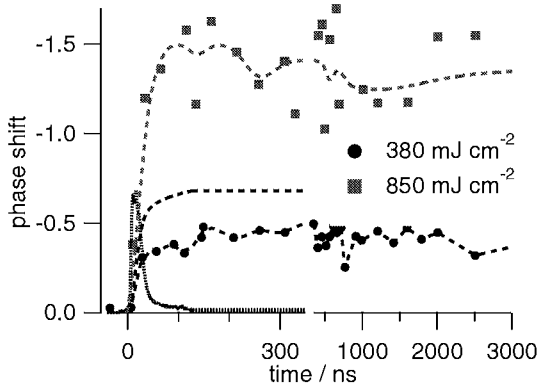

Fig. 2: Changes of the surface morphology during of the PMMA during/after 248 nm irradiation. The laser intensity and the deposited laser energy are also included in the graph.

The small detected phase shifts are proportional to the change of the film thickness and the refractive index and are most probably due to the opposite signs of the thermal expansion coefficient and the thermal refractive index coefficient.

4 ACKNOWLEDGEMENT

This work has been supported by the Swiss National Science Foundation.

CH_4 PRODUCTION FROM BIOMASS-DERIVED SYNTHESIS GAS: EFFECT OF THE FEED COMPOSITION ON THE ACTIVITY OF Ni-BASED CATALYSTS

F. Raimondi, M. Seemann, S. Biollaz, J. Wambach, A. Wokaun

The chemical and structural modifications of a commercial Ni/Al_2O_3-based catalyst during the production of methane from synthesis gas were investigated by post-reaction X-ray photoelectron spectroscopy (XPS). The effect of the composition of the synthesis gas on the structural properties of the catalyst surface and on its catalytic activity under methanation conditions was studied. The organic compounds present as contaminants in typical biomass-derived synthesis gas were found to promote strongly the reduction of Ni in the catalyst to the metallic state and the formation of elemental carbon on the catalyst surface.

1 INTRODUCTION

The need of a more extensive exploitation of renewable energy sources has recently awakened growing interest in the production of methane from biomass-derived synthesis gas. Ni-based catalysts are the established materials for the hydrogenation of carbon oxides mixtures. However, the composition of the synthesis gas typically obtained by biomass gasification imposes specific requirements to the methanation process and to the used catalyst. As a matter of fact, typical biomass-derived synthesis gas presents H:C ratios between 1.2 and 1.8 and is therefore hydrogen-poor with respect to the complete methanation of the contained carbon oxides. Moreover, the gaseous mixtures produced by fast internally circulating fluidized bed (FICFB) gasifiers contain a significant amount (10% and more) of organic compounds, in particular small unsaturated hydrocarbons (ethene, ethyne, propene, propyne, etc.) and complex aromatic molecules, collectively named "tars" [1]. These features of biomass-derived synthesis gas not only require the design of a dedicated methanation process, but also expose the catalyst to especially demanding conditions.

2 EXPERIMENTAL

Catalyst samples were exposed for 16 hours to various methanation conditions in a high-pressure reactor integrated in a UHV system equipped for XPS analyses. Post-reaction XPS experiments were carried out without exposing the catalyst to air after performing the catalytic tests.

3 RESULTS

Figure 1 shows the Ni $2p_{3/2}$ XP spectra obtained after exposure of the catalyst to various methanation feeds at 400°C in the HPR. The complexity of the used reactant mixtures increases from the bottom to the top of Figure 1, approaching the typical composition of the outlet of large-scale biomass gasifiers. For comparison, the bottom trace in Figure 1 shows the Ni $2p_{3/2}$ XP spectrum of a freshly reduced sample. The XP spectra in Figure 1 indicate that the working catalyst contains a mixture of Ni in the metallic and in the 2+ oxidation state. The chemical state of Ni does not change with the composition of the reactant mixture in the investigated range, as long as no hydrocarbon molecules are included in the feed. The presence of the hydrocarbons typically contained in the product stream of biomass gasifier (upper spectrum in Figure 1) causes a significant increase of the fraction of metallic Ni. The reducing properties of the hydrocarbon molecules are probably responsible for the extensive reduction of Ni(II) in this case.

The presence of hydrocarbons in the methanation feed also favours the formation of elemental carbon on the catalyst surface during the reaction. Figure 2 shows that the carbon content on the catalyst surface strongly increases when the hydrocarbons representative of biomass-derived synthesis gas are included in the reactant mixture. Carbon formation is detrimental to the catalytic performance and needs to be minimised in order to extend the catalyst lifetime.

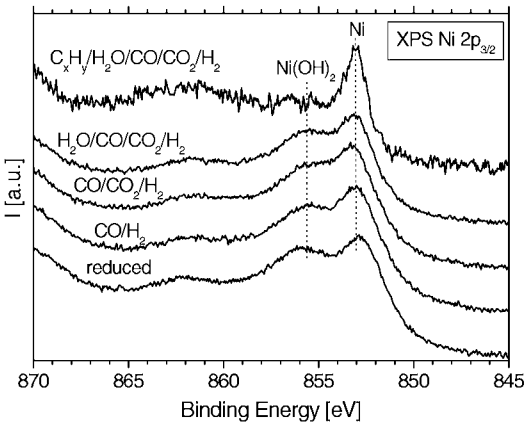

Fig. 1: Ni $2p_{3/2}$ XP spectra after exposure of the catalyst to various catalytic tests in the HPR.

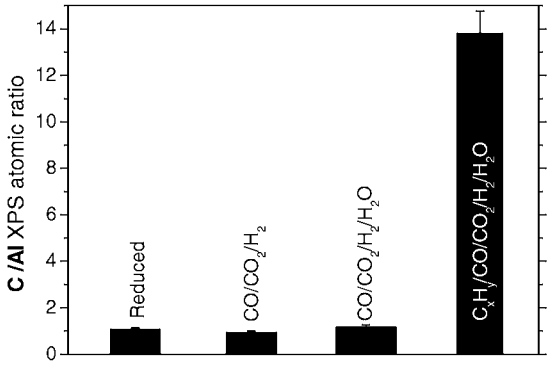

Fig. 2: Surface carbon content after selected catalytic tests in the HPR.

4 REFERENCE

[1] H. Hofbauer, G. Veronik, T. Fleck, R. Rauch, *Developments in Thermochemical Biomass conversion* **2**, 1016-1025 (1997).

LINK-UP OF A GASOLINE REFORMER TO A POLYMER ELECTROLYTE FUEL CELL

F. Hajbolouri, G.G. Scherer, A. Wokaun

A lab-scale gasoline reformer system was linked up to a 30 cm^2 polymer electrolyte fuel cell. A cell voltage of 690 mV and 580 mV at 480 $mAcm^{-2}$ was obtained when O_2 respectively air was used as oxidant. The traces of hydrocarbons in the reformate gas did not lead to performance degradation of the anode catalyst.

1 INTRODUCTION

One possibility to promote the commercialisation of the fuel cell technology is to use hydrogen, H_2, gained from reforming of gasoline or diesel as fuel. One advantage of such a system is that no change of the present fuel infrastructure is required. Further, the traces of hydrocarbons in the reformate do not lead to performance degradation of the anode catalyst at low temperatures, contrary to methanol. However, in order to become an alternative to combustion engines the overall system efficiency of the gasoline reformer-fuel cell system should be high and the total emissions should meet the future emission regulations regarding CO, HC, NO_X, and particles. Using gasoline or diesel as fuel for fuel cell systems is not a long- term solution to the future's energy problems rather a strategy to convey the fuel cell technology into the market. At the *Paul Scherrer Institut (PSI),* a lab-scaled reformer system where gasoline is reformed to H_2 has been connected to a 30 cm^2 polymer electrolyte fuel cell (PEFC). The reformer system was build by the *Catalytic Process Group* at *PSI*. The details about the reformer system can be found in the present *PSI Scientific Report 2003 / Volume VI.*

2 EXPERIMENTAL

All measurements were performed in a 30 cm^2 test cell with meander flow field graphite plates. A catalyst coated membrane (PtRu on anode and Pt on cathode) and two separate gas diffusion layers were used as membrane electrode assembly (MEA). The measurements were performed at a cell temperature of 60 °C. Both the fuel and the oxidant were fed with an excess of 50 % to the stoichiometric requirements and were humidified at 35 °C. When air was used as oxidant the cathode inlet was humidified at 55 °C. The reformer system consisted of two reactors, a Partial Oxidation (POX) reactor where the gasoline is reformed to H_2, CO_2, N_2, and CO and a Preferential Oxidation (PROX) reactor were CO is selectively oxidized to CO_2. After the PROX the reformate gas was fed into the fuel cell through a humidifier. The steady state current-voltage curves were recorded manually.

3 RESULTS

Prior to the link-up of the fuel cell-reformer system the CO-tolerance of the MEA material was explored for different CO-concentrations, Figure 1. Below CO-concentrations of 100 ppm the performance losses due to CO-poisoning proved to be negligible as compared to pure H_2 as fuel, and above 500 ppm, a further increase of the CO-content lead only to a slight additional performance loss. Figure 2 demonstrates the cell performance when the reformate gas is used as fuel. The polarization curves were recorded after operating the cell a couple of hours under steady state condition. The gas composition was 29 % H_2, 27 % CO_2, 35 % N_2, 9 % CH_4, and ~100 ppm CO. Comparing the cell voltage drop at a current density of ~500 mA/cm^2 for H_2/100 ppm CO and reformate containing also other by-products, CO_2 and N_2, only an additional voltage drop of 40 mV can be recognized.

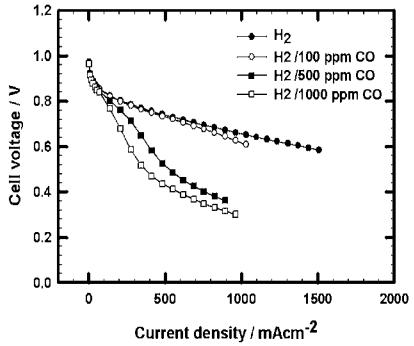

Fig. 1: Polarization curves for H_2 respective H_2/CO with varied CO-concentration at 60 °C. O_2 was used as oxidant. P_{anode}=$P_{cathode}$=1 bar_a.

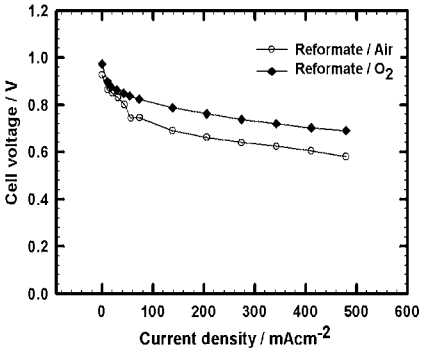

Fig. 2: Polarization curves for reformate gas at 60 °C. O_2 or air was used as oxidant. P_{anode}=$P_{cathode}$=1 bar_a.

4 CONCLUSION

The first results of the link-up between the fuel cell-gasoline reformer system proved to be very promising. However, the influence of the fuel cell operating parameters, such as temperature and pressure on its performance still have to be explored.

"PowerPac", A PORTABLE 1 kW FUEL CELL SYSTEM

M. Santis, D. Schmid (ETH Zürich), M. Ruge (ETHZ), G. Paganelli (ETHZ), F.N. Büchi

In a joint project, PSI and ETHZ have developed a portable 1 kW_{el} power generator on the basis of polymer electrolyte membrane (PEM) fuel cells technology. A new generation of fuel cell stacks with innovative concepts for sealing of bipolar plates, light current collectors, light endplates and integrated modular humidification of the process air was developed. In addition, the entire balance of plant for the three media, hydrogen, process air and coolant, as well as the electronics and controls were designed to meet the requirements of a portable system. The prototype is a portable unit with a net power output of 1 kW_{el} (unregulated DC) and a dynamic >> 1 kW/s.

1 INTRODUCTION

A 1 kW_{el} portable power generator on the basis of PEM fuel cells technology has been developed in the PowerPac project. The PowerPac demonstration unit (Figure 1) is a turnkey system, fuelled with pure hydrogen.

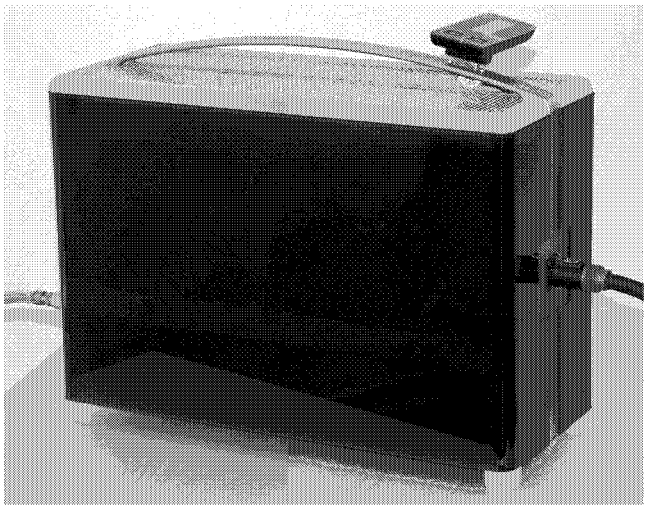

Fig. 1: PowerPac in operation. Bottom left: hydrogen inlet. Centre right: DC-current connector.

The central element of the system is a fuel cell stack with specially designed bipolar plates which allow for an internal humidification of the process air [1, 2] and operation with only a minimal excess of hydrogen [1]. The balance of plant was built with commercially available components and the system is regulated by an optimized turnkey control unit.

PowerPac includes technological innovations for the use in mobile systems:

- No external air humidification device is required.
- Only a small percentage (<10 %) of the hydrogen is recycled.
- A modular concept is employed.

These developments make the fuel cell system less complex, easier to control and cheaper. The overall efficiency is higher, given that no extra energy for the humidification of the process air is needed and only a small amount of the hydrogen has to be recirculated. In addition the fully modular humidification concept [3] makes scaling easier since only small adaptations on the system side and fuel cell stack are necessary in order to adjust to a range of 0.5 – 2 kW_{el} maximum power.

The PowerPac demonstration system produces 1 kW_{el} unregulated DC-power, has a volume of 35 l and a weight of 23 kg.

2 FUEL CELL STACK

For stable operation of a PEM fuel cell stack, humidification of the process air is necessary to maintain the solid polymer membrane humidified under various operating conditions. Basically there are two concepts for humidification of the reactant gases: i) externally, where a separate humidifier provides liquid water or water vapour, and ii) internal humidification, where a gas humidifying facility is integrated into the fuel cell stack.

Internal humidification is more advantageous for function integration. In the PowerPac fuel cell stack humidification of the process air is realized individually in each cell [1, 2], making the process modular, independent from the number of cells and operation temperature and thus fully scalable. The 44 cell stack is shown in Figure 2.

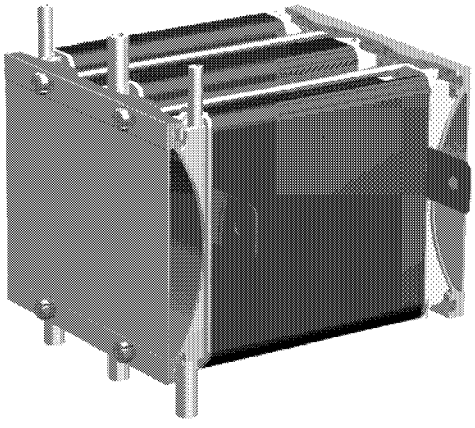

Fig. 2: CAD-Picture of the 44 cell PowerPac-Stack. Volume: 5 l, weight: 6.8 kg.

The performance of the PowerPac stack when operated with externally humidified air and internal humidification is shown in Figure 3. The comparison shows that with internal humidification the power loss at 47 A is of only 4 %.

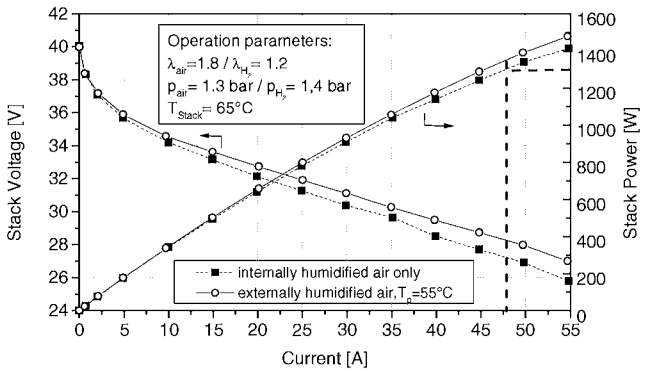

Fig. 3: Current/Voltage and Current/Power curves of the 44 cell stack at 65°C. The dashed line at 1300 W shows the operating point of the stack in the 1kW$_{el}$-PowerPac system at full load.

3 BALANCE OF PLANT

The BoP consists of three media loops, the air path, the hydrogen loop and the coolant loop as well as the electronics and control unit (Figure 4).

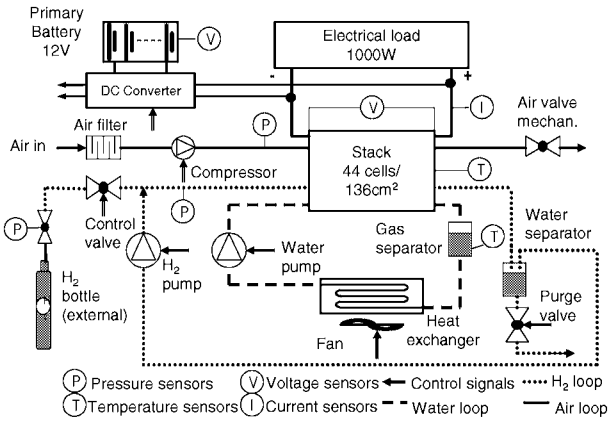

Fig. 4: Scheme of the PowerPac System.

Media streams: i) air path: after being filtered, the process air is compressed by means of a rotary valve compressor and delivered at 1.1 – 1.4 bar (depending on the load) to the stack. ii) hydrogen loop: hydrogen is delivered from an external pressure bottle. After reducing the hydrogen pressure to 2 bar it is fed to the stack with an excess of ca. 10%. This excess fuel is recirculated by a small membrane pump. iii) cooling loop: the cooling media is pure water.

Controls: the overall architecture of the PowerPac System control including a control and a power board (microchip PIC18F452) is designed to achieve fully autonomous, safe and easy operation. The user interface is a removable unit on the carrying handle with ON and OFF buttons and an information panel. On the information panel data regarding current, voltage, pressure of the gases and temperature of the stack are displayed.

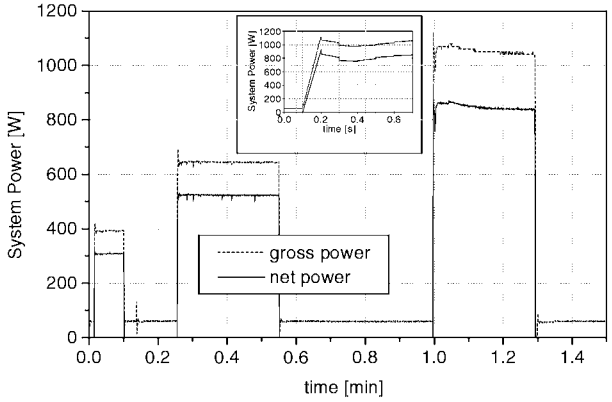

Fig. 5: System dynamics. Power modulation to different output power levels. Inset: power transient from idling (zero net power) to 850 W net power. Stack gross power and system net power are shown.

4 SYSTEM DYNAMIC AND CHARACTERISTIC

Upon cold start (T = 20 °C), 80% power is available in less than 30 s. The system exhibits excellent dynamics (as shown in Figure 5) and automatically follows the external power requirement at rates up to 10 kW/s.

The *system* has a maximum efficiency of 50 % (at a *stack* efficiency of 60 %). The characterization of the system net power output and system efficiency is shown in Figure 6. The efficiency of the system is highest at mid net power rates.

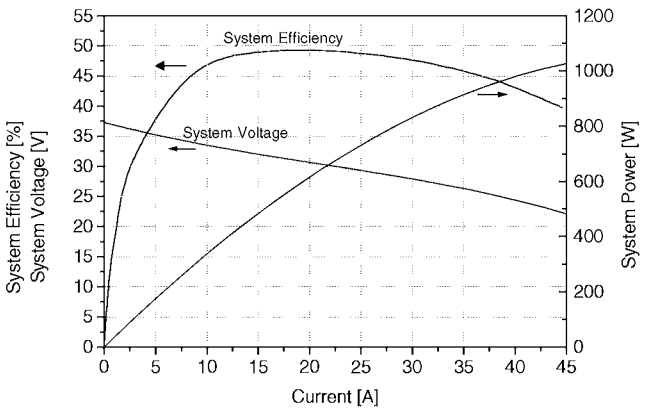

Fig. 6: Current/Efficiency, Current/Voltage and Current/Power curves for the PowerPac system.

5 ACKNOWLEDGEMENTS

Financial support by the Swiss Federal Office of Energy (BFE), contributions from Tribecraft AG, MES-DEA and Brütsch-Elektronik are gratefully acknowledged.

6 REFERENCES

[1] M. Santis, D. Schmid, M. Ruge, F.N. Büchi, PSI Scientific Report 2002, **V**, 96 (2003).

[2] D. Schmid, M. Ruge, F.N. Büchi, Swiss Patent Application Nr. 1031/02, 17.06.02.

[3] S. Freunberger, M. Santis, F.N. Büchi, PSI Scientific Report 2003, **V**, 121 (2004).

BEHAVIOUR OF POLYMER ELECTROLYTE FUEL CELLS WHEN SCALING UP FROM A UNIT CELL TO A STACK

A. Tsukada, S. Freunberger, F.N. Büchi

Often the performance of a unit cell or a small stack of a few cells is used to extrapolate to the power and efficiency of a large stack. An important issue in scale-up is gas distribution to the individual cells in the stack. Due to the parallel gas supply, individual cells may not receive an optimal quantity of fuel or air. The stack may not deliver the maximum power predicted from the single cell measurement. Stoichiometric ratio λ, gas pressure P, pressure difference ΔP and flow field characteristics are the most important parameters for obtaining stable and similar voltage from each cell.

1 INTRODUCTION

In an optimized fuel cell system minimal stoichimetric gas flow rates to the stack are desirable because parasitic power and complexity of the balance of plant are reduced. However when hydrogen and air stoichiometries are significantly reduced then the slightly inhomogeous distribution to the individual cells, due to stochastic water condensation, temperature variations and geometric tolerances, becomes important. So even if the mean stoichiometric ratio of gas is sufficient, individual cell voltages can drop drastically due to insufficient gas supply.

2 EXPERIMENTAL

The test bench comprises a PEFC stack, which was developed at the Paul Scherrer Institut. It consists of 12 cells, each with an active area of 204 cm^2. The nominal power output is 1.3 kW. The stack is supplied with pure hydrogen and air. It is operated at 2 bar_a and at temperatures below 70 °C. The membrane is Nafion™ N112 (Dupont).

3 RESULTS AND DISCUSSION

Performance of the 12-cell stack with standard stoichiometric ratios of 1.5 and 2.0 for hydrogen and air, respectively is shown in Figure1. These stoichiometric ratios are sufficient for homogeous operation of all cells.

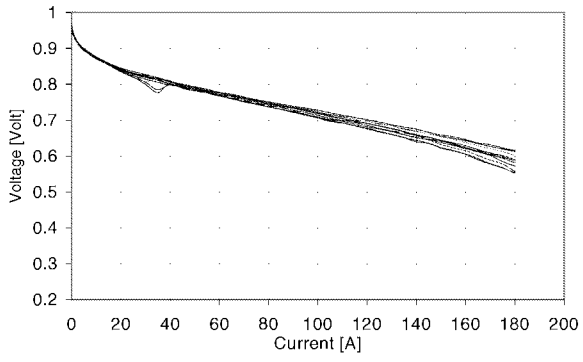

Fig. 1: Polarization curves of individual cells in 12-cell stack, with λ_{H2}= 1.5, λ_{air}= 2.0.

If hydrogen stoichiometry is reduced significantly to λ_{H2}=1.3, then several cells show an unstable behaviour between 20 and 140 A (Figure 2) and the voltage of other cells is even better than that obtained in a single cell experiment. At the low stoichiometry, the slightly inhomogeneous gas-distribution becomes significant.

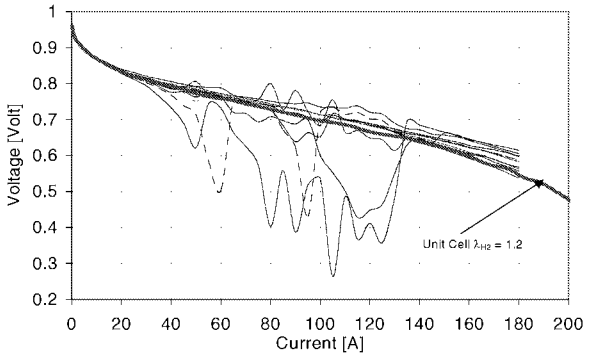

Fig. 2: Polarization curves of individual cells in 12-cell stack, with λ_{H2}= 1.3, λ_{air}= 1.5; Curve for single cell with λ_{H2}: 1.2.

A low stoichiometric ratio of air also destabilizes certain cells between 20 and 60 A (Figure 2). Additionally, at higher currents, the stack voltage drops due to oxygen diffusion limitations.

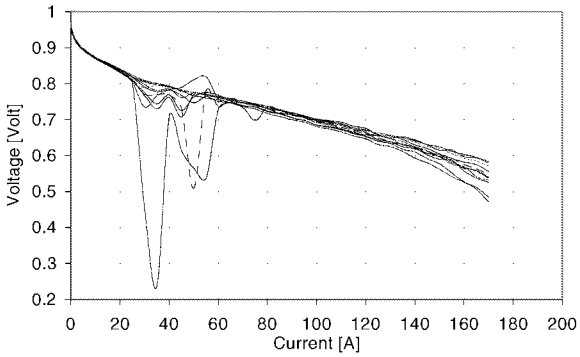

Fig. 3: Polarisation curves of individual cells in 12-cell stack: λ_{H2}= 1.5, λ_{air}= 1.5.

4 CONCLUSION

When scaling up from a unit cell to a stack, the lower limits of stoichiometric ratios for H_2 and air have to be considered carefully. Voltages of individual cells in the stack can become unstable under conditions where the single cell showed completely stable operation. At partial load the pressure drop in the stack is far lower than at maximum flow, for which the flow field dimensions are conceived. Countermeasures, for stabilization of all cells are i) variation of the stoichio-metric ratios as funtion of load; ii) variation of operating pressure as function of load.

DIMENSIONING OF A CELL INTERNAL AIR-HUMIDIFICATION DEVICE FOR PE FUEL CELLS – THEORETICAL CONSIDERATIONS

S. Freunberger, M. Santis, F.N. Büchi

The analysis of the complete H_2/air polymer electrolyte fuel cell system shows that process air humidification is one of the biggest obstacles for a high performing portable system in the kW-range. Passive process air humidification integrated into each cell makes the process independent from the number of cells and operation mode, thus making the concept fully scalable. Special attention has to be paid on the dimensioning of the device in order to cover a wide range of operating conditions in the best possible way. Therefore, a model for examination of the mass balance in the humidification device has been developed.

1 INTRODUCTION

Stable and efficient operation of PE fuel cells requires proper water management for different reasons. Both flooding of the porous electrodes and drying out of the membrane have to be avoided. The latter phenomenon is likely to occur at the air inlet when dry gas is fed. Since membrane resistance increases strongly with decreasing water content this leads to serious overall performance losses in cell operation. Therefore, the air has to be moistened prior to feeding into the cell. External devices require additional controls and energy for heating and enlarge the system through disintegration. Cell internal humidification in contrast scales with stack size and makes the system simpler, cheaper and more compact. In this project this is achieved by transferring water from the moist exhaust air through a membrane to the fresh air (see Fig. 1).

Since the internal humidifier is a passive element there is no possibility to regulate it according to the actual operation. Hence its size has to be dimensioned for the best possible compromise covering a wide range of operating conditions especially in temperature and air stoichiometry. The section should be as small as possible to have a minimum impact on the weight and volume of the stack, but should be big enough to ensure sufficient humidification of the process air under a range of working conditions.

2 MODELLING

A model for the combination of a fuel cell and the humidification area has been developed [1]. Figure 1 shows a schematic of the modelled arrangement.

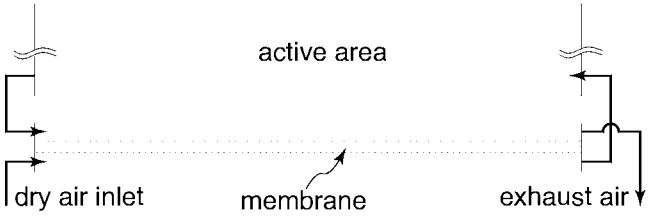

Fig. 1: The configuration of gas flow through the modelled humidifier unit and the cell.

For the sake of simplicity only mass conservation equations were solved in one dimension within the channels adjacent to the membrane. The transport through the membrane is characterised by diffusion with boundary conditions obtained by the water sorption isotherm reported in [2]. The resulting set of equations has been solved by low order finite difference schemes. In order to avoid the calculation of the cells' water balance by applying a full cell model it was assumed that all product water leaves the cell with the exhaust air stream. Thus, the water streaming into the humidifier area with the exhaust air is given by the sum of product water and the resulting humidity of the moistened fresh air. Since that amount of water in the fresh air is initially unknown an iterative procedure had to be applied until convergence was achieved.

3 EXPERIMENTAL

In order to examine the viability of the model mass balance measurements were performed on an exchanger unit similar to that one to be used in the cell. It consisted of two sets of parallel channels adjacent to both sides of a Nafion® 112 membrane and controllable temperature. Dry and wet air with water and gas flow rates regarding to cell operation at a certain current and air stoichiometry were fed into the device. The mass balance was obtained by capturing the water in the two outlet flows.

Using the mentioned concept a stack of 1.3 kW nominal power has been realised and tested [3].

4 RESULTS

There were in principle two different tasks to be accomplished by the model calculations: (i) finding the minimum size of the device delivering sufficient humidification to the fresh air at the specified standard operating conditions in the system, (ii) giving an explanation to the experimentally observed behaviour of the cells that has been observed when testing the finally realized stack.

Results for the humidification efficiency as a function of the ratio between humidifier area and cell area at different gas pressures are given in Fig. 2. The dew point of the humidified air is increasing with increasing area of the humidification section and decreasing air stoichiometry. These calculations suggest to run the system at maximum tolerable pressure within the boundary of rising parasitic power need of the compressor. For the projected pressure of 1.5 bar_a a humidifier area of 15 percent of the active cell appears to be the optimum with respect to volume and air moisturisation.

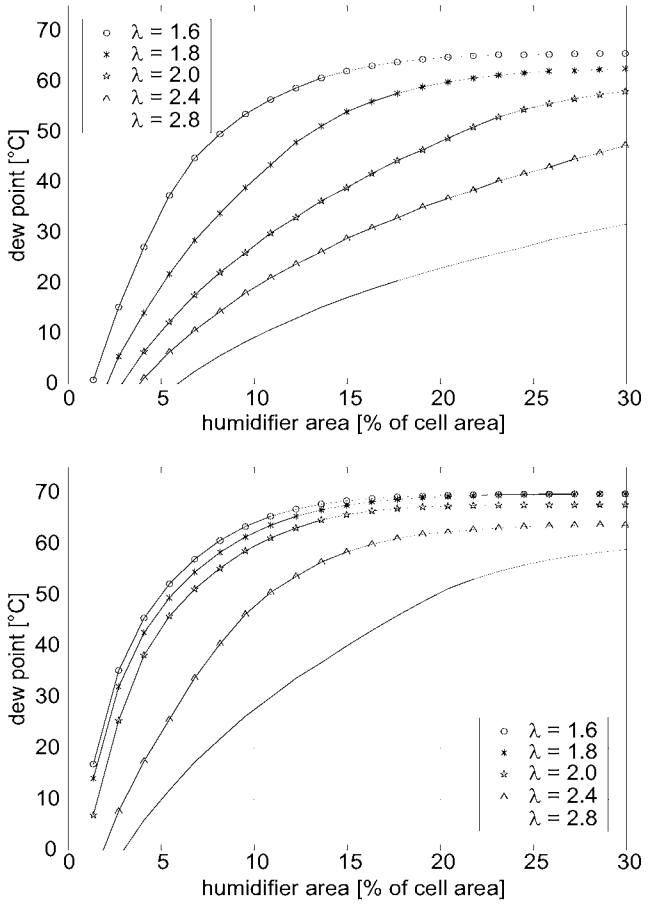

Fig. 2: Resulting dew point at cell inlet as a function of relative humidifier area for different air stoichiometries at a cell pressure of 1 bar_a (top) and 1.5 bar_a (bottom). The average current density is 370 mA/cm^2 at a cell temperature of 70 °C.

In Fig. 3 a cut through the curves in the lower plot of Fig. 2 at 15 % relative area is shown. The decreasing dew point with rising air stoichiometry coincides with the experimentally observed decline of cell performance at higher air flow rates. In contrast this observation, cells operated at constant full humidification do not drop with growing air flow.

Figure 4 shows the simulated humidification together with experimental values for a range of cell temperatures. These results suggest that the model outputs are best case values for feasible operating temperatures below 80 °C. In agreement with these predictions, the stack power showed its maximum value at 70 °C and dropped seriously when it was operated at higher temperatures. Above this point the difference between cell temperature and the dew point of the air increases up strongly.

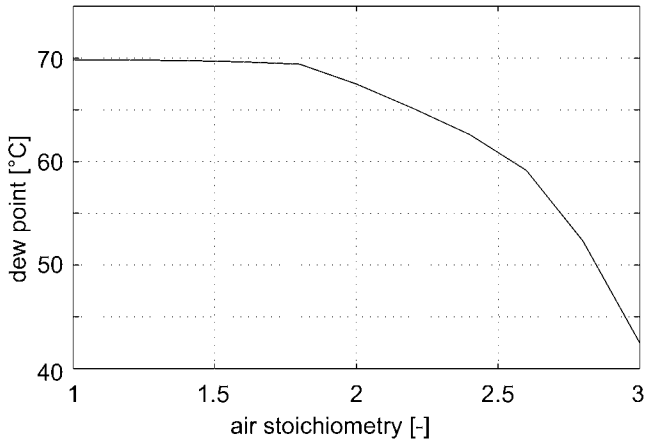

Fig. 3: Dew point as a function of air stoichiometry. The conditions are the same as in Figure 2 (bottom).

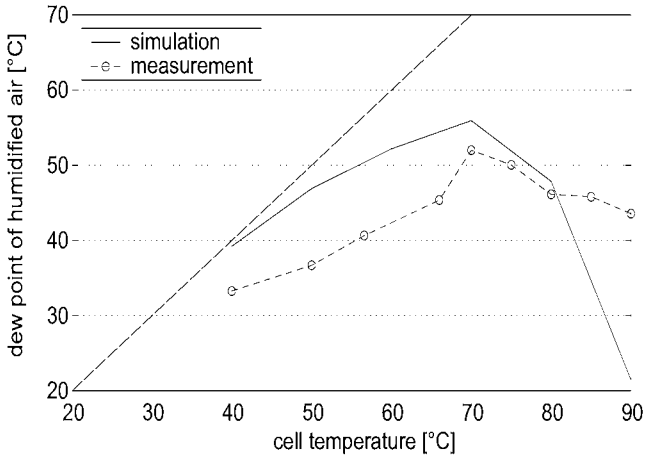

Fig. 4: The simulated and experimentally observed dependence of the dew point on the cell temperature.

5 CONCLUSIONS

For the dimensioning of a cell internal air humidification device a simplistic model has been developed. The simulation shows reasonable agreement with measurements and was therefore used to examine the resulting dew point at the outlet of the humidification device. Internal humidification has both experimentally and theoretically been established as a feasible way to simplify PEFC systems in the 1 kW range and improve their efficiency due to lower parasitic power.

6 REFERENCES

[1] S. Freunberger, Diploma thesis, Paul Scherrer Institute, Villigen PSI, Switzerland and Institute for Chemical Technologies and Analytics, TU Vienna, Austria, October (2002).

[2] J.T. Hinatsu, M. Mizuhata, H. Takenaka, J. Electrochem. Soc. **141**, 1493 (1994)

[3] M. Santis, D. Schmid, M. Ruge, G. Paganelli, F.N. Büchi, PSI Scientific Report 2003, **V**, 118 (2004).

SCIENTIFIC CONTRIBUTIONS FROM THE ELECTROCHEMISTRY LABORATORY FOR THE PSI SCIENTIFIC REPORT 2003 VOLUME II, LIFE SCIENCES, ISSN 1423-7318

Please note that the following page numbers refer to the original page numbers in the PSI Scientific Report 2003, Volume II, Life Sciences.

Please cite the following contributions as indicated

L. Tiefenauer, B. Steiger, J.J. Hefti, C. Padeste
Protein-conjugates for bioelectrochemical interfaces
Paul Scherrer Institut Scientific Report 2003 / Volume II, ISSN 1423-7318.

PROTEIN-CONJUGATES FOR BIOELECTROCHEMICAL INTERFACES

L. Tiefenauer, B. Steiger, J.-J. Hefti, C. Padeste

Conjugates in which ferrocene centers are attached via linkers of various lengths to the anchor protein streptavidin have been immobilized in monolayers on gold electrodes. Charge transfer effects have been investigated with the aim of biomolecular interface construction.

INTRODUCTION

The usefulness of ferrocene-streptavidin conjugates for biosensor applications has recently been demonstrated (1). Charge transfer from the electrochemically active prosthetic groups of the two enzymes glucose and lactate oxidase to the electrode surface is mediated by protein-linked redox centers resulting in pronounced electrochemical signals. It was found that the measured current strongly depends on the molecular architecture. Therefore, structural differences of immobilized molecular assemblies on charge transport have been investigated.

METHODS

The length of the linker used for coupling ferrocene-moieties to streptavidin has been varied in the range of 0.5 nm to 2 nm and the peak currents of the immobilized conjugates were determined from cyclic voltammetry experiments. In a second experiment, a first layer of the long-linker conjugate was immobilized via biotin on electrodes, followed by electrochemically inactive streptavidin as a macromolecular bulky spacer to which again conjugate was bound via in situ generated bis-biotin.

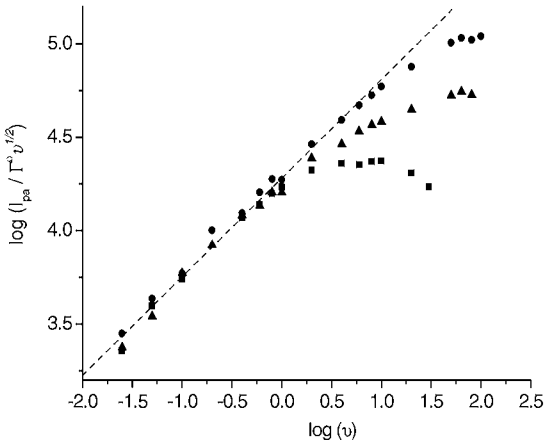

Fig. 1: Normalized anodic peak currents determined from cyclic voltammetry of conjugates with a short ■, a medium ▲ and a long linker ●.

RESULTS

It could be demonstrated (Fig. 1) that the normalized anodic peak current $I_{pa}/\Gamma^0\upsilon^{1/2}$ deviates from the response expected for a one-electron Nernstian redox couple (dashed line) at scan rates of about 1 V s^{-1} when using the short-linker conjugate. This deviation occurs at ten times higher scan rates with the long-linker conjugate (●).

A long linker enables fast charge transfer. The coverage of ferrocene in the third layer is more than expected for a monolayer indicating that the additional conjugates bind to the biotinylated Lys-residues of streptavidin. However, these inactive streptavidin molecules do not significantly disturb the charge transport process when using the long-linker conjugate (Fig. 2) whereas this has been observed in an analogous system of the short-linker conjugate.

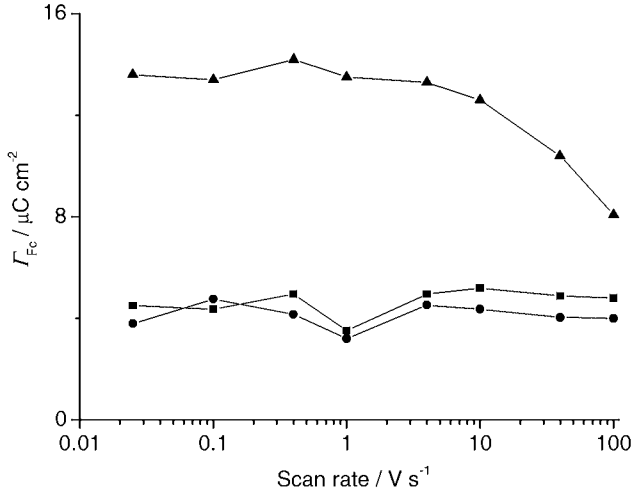

Fig. 2: Apparent ferrocene coverage (□Fc) determined from mixed multilayers built up of the long-linker conjugate in the first (■) and the third layer (▲) separated by streptavidin (●).

CONCLUSION

These results show that long-linker streptavidin conjugates are most suitable for charge transfer in biomolecular assemblies. A long linker enhances the flexibility and accessibility of the ferrocene-centers and thus facilitates charge transfer. Thus, the new conjugate is useful as an electrochemically active molecular anchor for biosensor applications and may be a key component to establish electrochemical contacts in future bioelectronic micro-devices.

REFERENCE

1. Padeste, C., Steiger, B., Grubelnik, A., Tiefenauer, L. Redox labelled avidin for enzyme sensor architectures. Biosensors & Bioelectronics *19*: 239-247, 2003.

Paul Scherrer Institut, 5232 Villigen PSI, Switzerland
Tel. +41 (0)56 310 21 11, Fax +41 (0)56 310 21 99
Internet: www.psi.ch